

POLITECNICO DI TORINO

Mathematical Engineering

Master's Thesis

A CFD study of *Morpho* butterflies



Supervisors:

Prof. Stefano Scialo

Ir. Jaap Windt

Prof. Florian Muijres

Candidate:

Dario Amadori

A.Y. 2018/2019

*A mio padre e mia madre, per avermi offerto tutto ciò di cui avevo bisogno per
percorrere il mio cammino*

Contents

Acknowledgments	i
Introduction	iii
1. State of the Art	1
1.1. Meet the <i>Morphos</i>	1
1.1.1. Conventions and nomenclature in insect flight	1
1.1.2. How should we model <i>Morpho</i> butterflies?	3
1.2. Mathematical Modelling and Numerical Methods	7
1.2.1. The Navier-Stokes equations	7
1.2.2. Reynolds Number: dynamical similarity	7
1.2.3. The problem of turbulence	8
1.2.4. The time-averaged Navier-Stokes equations	10
1.2.5. The Boussinesq assumption	13
1.2.6. The Spalart-Allmaras model	14
1.2.7. The $k - \omega$ and SST $k - \omega$ models	15
1.2.8. Transition modelling	17
1.2.9. Partially averaged Navier-Stokes equations	17
1.3. Numerical Errors and Uncertainty Estimation	18
2. Approach, Tools, Methodology	22
2.1. Approach to the problem and main assumptions	22
2.1.1. Modelling the wing	23
2.1.2. Modelling gliding flight	25
2.1.3. Modelling flapping flight	28
2.1.4. Inverse dynamic model of a gliding butterfly	29
2.2. Tools	30
2.2.1. ReFRESH CFD solver	32

2.2.2.	HEXPRESS™ mesher	33
2.2.3.	MARIN internal software for numerical uncertainty estimation	34
2.3.	Methodology	34
2.3.1.	Generation of the grids and procedure for refinements	34
2.3.2.	Rotation of the grids	38
2.3.3.	On the importance of grid refinements in the wake and of the values of y^+	40
2.3.4.	On the size of the domain	43
2.3.5.	On the time and space discretisation for flapping simulations	44
3.	Reproduction of a Morpho Butterfly's Gliding Flight Using Various Turbulence Models and Comparison with Experimental Data	48
3.1.	Setup and Considerations	48
3.1.1.	Common configurations	52
3.1.2.	Configurations for turbulence equations	54
3.1.3.	Configurations for the timestep	56
3.1.4.	Configuration of the f_k value	59
3.2.	Results	59
3.2.1.	Residuals	59
3.2.2.	Numerical uncertainty	61
3.2.3.	Velocity field in the stream direction	63
3.2.4.	Unsteadiness of PANS simulations	67
3.2.5.	Development of turbulence in the flow	67
3.2.6.	Turbulent intensity	73
3.2.7.	Pressure distribution	74
3.2.8.	Limiting streamlines	77
3.3.	Comparison of the numerical simulations with experimental results	79
3.4.	Discussion	82
4.	Comparing Different Morpho Species By Means Of Computational Fluid Dynamics	84
4.1.	Setup and Considerations	84
4.1.1.	Gliding setup	85
4.1.2.	Flapping setup	86

4.2. Results	88
4.2.1. Residuals	88
4.2.2. Numerical uncertainties	90
4.2.3. Drag and lift coefficients	90
4.2.4. Lift-to-drag ratio	92
4.3. Pressure distribution in gliding flight	93
4.3.1. Limiting streamlines in gliding flight	95
4.3.2. Vortex structures on the wing in gliding flight	95
4.4. Discussion	98
5. Conclusions and Final Remarks	100
5.1. Which CFD model should we use to reproduce the flight of <i>Morpho</i> butterflies?	100
5.2. Do different <i>Morpho</i> species have different aerodynamic performances?	101
5.3. Future work	101
A. Support Plots for Chapter 3	102
A.1. Numerical uncertainties	102
B. Support Material for Chapter 4	104
B.1. Numerical uncertainties	104
B.2. <i>Morpho cisseis</i> : pressure coefficient on the wing	116
B.3. <i>Morpho deidamia</i> : pressure coefficient on the wing	120
B.4. <i>Morpho cisseis</i> : velocity limiting streamlines on the wing	125
B.5. <i>Morpho deidamia</i> : velocity limiting streamlines on the wing	130
B.6. <i>Morpho cisseis</i> : vortex structures	135
B.7. <i>Morpho deidamia</i> : vortex structures	139

Acknowledgments

The caterpillar does all the work,
but the butterfly gets all the
publicity.

George Carlin

To me, writing this thesis made time accelerate. Everything happened so quickly that I am not sure I can distinguish the person who is writing now from the one that started this work eight months ago: somehow, they are overlapping, they are living in the same moment. When, in the middle of this timelapse, I found myself thinking about what this thesis meant to me, I realised something. This work represents for me a milestone in my life, it is at the same time the end of an era and the beginning of another one. Most of the time, in the last months, I was only focusing on the latter: future is becoming present so fast that I can't not think about it. But that moment of reflection made me realise that I was pointing my attention only at the butterfly, which gets all the publicity, and I was neglecting all the things accomplished by the caterpillar. For this reason, I find it necessary to mention all the people who helped me achieving these results and becoming who I am.

First of all, I want to thank my supervisors: Prof. Stefano Scialò for being always helpful and at my disposal any time I needed; Ir. Jaap Windt for sharing with me his broad knowledge in fluid dynamics and numerical simulations and for making me understand the importance of precision and critical sensibility in this work; last but not least, Prof. Florian Muijres, for often offering me the out-of-the-box perspective and for some really interesting stories about the animal world. Then I would like to thank the interns at MARIN, who have been to me more friends rather than colleagues, and whom I spent incredible moments with: I hope we will meet soon again. A particular thanks goes to Andrea, for helping me in what I fear most: CAD. I also want to thank Pietro, for making everything better in Wageningen and,

the other way around, Wageningen for accomplishing what Trento hadn't been able to: braid our paths together. A big hug goes to my colleagues Beppe, Luca, Giulio, Fabio, Paolo, Matteo, Michela and Francesca, who fulfilled my time at Politecnico with nice and warm moments. A hug is also owed to my friends who shared with me those little things of life that just make you happy: Mattia, Pietro, Alessandro, Ilaria, Federica, Hannah, Francesco and Piero and all my team mates from Invicta. Then I want to deliver all my gratitude to those guys who mean everything to me: Luca, Elia, Manuel, Alice, Marco, Sebastiano, Emil, Giovanni, Martin and Raffaele. All my affection goes to my family, in particular to Alessandro for his unconditional love, to Simone for his wise suggestions and to my parents, whom I could never payback enough what they gave to me.

Introduction

Una volta che abbiate conosciuto il
volo, camminerete sulla terra
guardando il cielo, perché là siete
stati e là desidererete tornare

Leonardo da Vinci

This famous sentence of Leonardo Da Vinci means literally "once that you have experienced flight, you will walk on earth looking at the sky, since there you have been and there you will desire to go again". Since long time ago nature has been source of great inspiration for human beings: Leonardo da Vinci had been a keen observer of anatomy and flight of birds with the aim of both studying them and creating a "flying machine" and he might deserve the title of "forefather of biomimetics". After him many scientists began to investigate the complexity and beauty of nature, trying to catch its perfection and exploit it for human progress and technology growth.

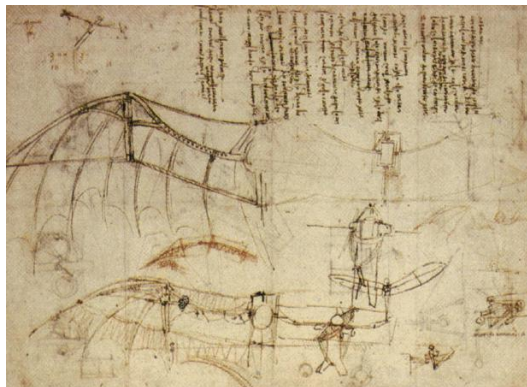


Figure 1.: Leonardo da Vinci's design for a flying machine with wings based closely upon the structure of bat wings.

The present work constitute another human attempt to explore the mightiness of Mother Nature and to gain some useful insights from her. Our attention is focused here on *Morpho* butterflies, which represent a numerous group of different

butterfly species living mostly in South America, Central America and Mexico. The large number of species translates in a broad variety of individuals with different morphological and behavioural characteristics and attitudes. The range of wingspan among the different species goes from 7.5 to 20 cm, the colours and patterns are various and the shapes of the wings can have substantial differences. Some species move around flapping -as almost all the insects- whereas others are able to perform flap-gliding phases, which are typical in birds. Among the many interesting aspects of this butterflies that can be studied, we will focus on the following goals:

1. define a robust set of tools, manners and methodologies which can represent an exhaustive and appropriate process to approach the CFD study of *Morpho* butterflies and, more in general, other insects operating in similar dynamical conditions; these aspects are discussed in Chapter 2;
2. supported by field data, we reproduce gliding flight conditions using different mathematical models to understand which ones are more capable to produce realistic results; this part of the work is gathered in Chapter 3;
3. given the insights gained at the previous points, we use CFD to compare the performances of two *Morpho* species, the *cisseis* and the *deidamia*, in both gliding and flapping flight; these results are available in Chapter 4.

The computational simulations are performed with the CFD solver ReFRESKO, taking great care of producing reliable results: rigorous procedures for the estimations of numerical errors are carried out, together with accurate tuning of the software and models used parameter.

Since the work consists of almost two hundredsof CFD simulations, for sake of conciseness, clearness and understandability only the aspects of the results important for the purposes of the work will be discussed; two appendixes report results which didn't find space inside the text.

1. State of the Art

Well, I must endure the presence of a few caterpillars if I wish to become acquainted with the butterflies.

Antoine de Saint-Exupéry, The Little Prince

1.1. Meet the Morphos

1.1.1. Conventions and nomenclature in insect flight

The present work will adopt a terminology commonly used in insect flight literature [9, 44, 24], borrowed from fixed wing aerodynamics: the wing will be considered as an aerofoil; "wing span" refers to the length between the tips of the wings, whilst "wing length" refers to the root-to-tip length of one wing. "Wing chord", instead, refers to the section between the leading and trailing edge of the wing at any given position along the span (Figure 1.1 (A)); the ratio between wingspan and mean chord is a non-dimensional morphological parameter termed "aspect ratio". "Angle of attack" refers to the angle between the wing chord and the relative velocity vector of the fluid in the "free-stream flow" or "mean flow", *i.e.* the flow not influenced by the presence of the wing. This limitation to the non-disturbed flow is necessary since, close to the wing, the flow is influenced by the presence of the aerofoil, which induces a downwash U' that, even if small in magnitude compared to the "free-stream velocity" U_∞ , can significantly alter the direction of the local flow velocity, with the effect of lowering the angle of attack. The angle of attack relative to the mean flow will be from now on simply termed "angle of attack" α , whilst the angle of attack relative to the deflected flow is termed "effective angle of attack" α' (Figure 1.1 (B)); this two quantities are tied together by the relation:

$$\alpha - \alpha' = \tan^{-1}\left(\frac{U'}{U_\infty}\right).$$

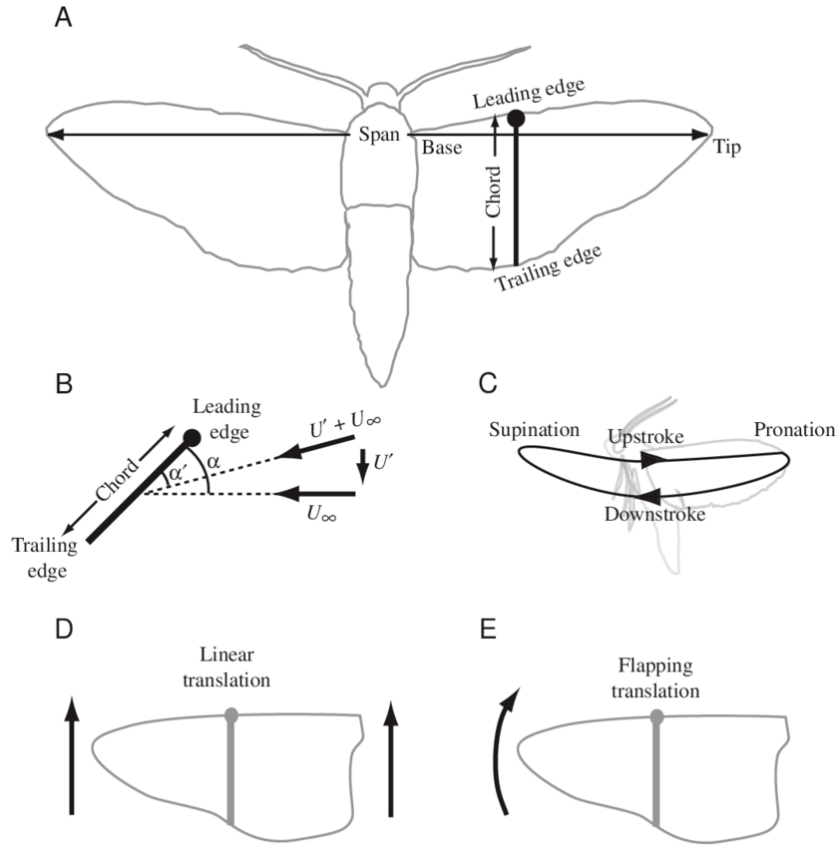


Figure 1.1.: Conventions and terminology. (A) Sketch of an insect. (B) Sectional view of the insect wing. (C) Phases of insect wing kinematics. Wing pronation occurs dorsally as the wing transitions from upstroke to downstroke, and wing supination occurs ventrally at the transition from downstroke to upstroke. (D,E) gliding (or Linear) and flapping translation. Source: [44].

During their flight, insects perform many different flapping patterns, which makes it difficult to define unequivocally the kinematics of flapping flight; to overcome this issue, researchers restricted their studies to hovering [44, 13]. Terms "upstroke" and "downstroke" are used here to describe ventral-to-dorsal and dorsal-to-ventral motion of the wing respectively (Figure 1.1 (C)). If the insect moves forward, their stroke plane bends forward. The term "wing rotation" refers to any change in angle

Morpho deidamia
Hinge-to-tip length = 7.56 cm



Figure 1.2.: Wing shape of a *Morpho deidamia* specimen.

of attack around a chordwise axis. During the downstroke-to-upstroke transition the wing "supinates", performing a rotation that brings the ventral surface of the wing to face upward, whereas during upstroke-to-downstroke transition the wing "pronates" bringing the ventral face of the wing to face downward (Figure 1.1). From now on, "gliding translation" will refer to aerofoils translating linearly (Figure 1.1 (D)), whereas "flapping translation" will refer to an aerofoil revolving around a central axis (Figure 1.1 (E)).

The insects considered here are *Morpho* butterflies, which comprise a large number of different species that can be found mostly in Central and South America. They boast important sizes, with wingspans reaching 20 cm ([22]), different wing shapes between the various species and fly at velocities in the range 1-2 m/s, performing different flying techniques.

1.1.2. How should we model Morpho butterflies?

Morpho butterflies are among the biggest insects on the entire planet and, thanks to their dimensions, they are able to perform flap-gliding flight ([22]). This characteristic, common in birds but not in insects, makes them of particular interest and carries the question of how to simulate and reproduce their different flying techniques. In the last years, attention to the flying behaviour of insects has drastically grown, largely as a consequence of industrial and engineering interest for small size flying vehicles; this led to an increment of studies about the performances of low aspect-ratio airfoils at low Reynolds numbers (see [49, 33, 10]). Nonetheless, most of

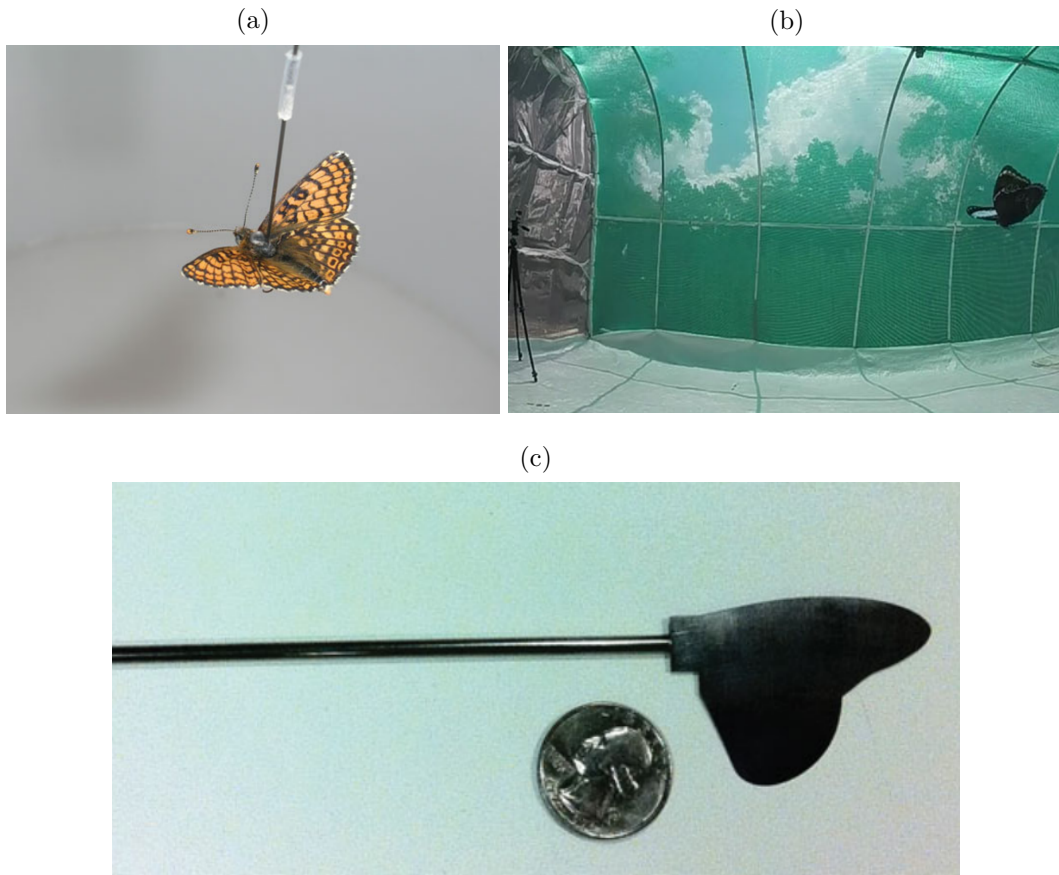


Figure 1.3.: Examples of techniques used to observe and study the aerodynamics of butterflies. In (a) a *Melitatea cinxia* attached to a tether in a laboratory; source: [37]. In (b) the insectary used in [22] to film various species of *Morpho* butterflies. In (c) an artificial wing model used in [46].

them only take under consideration Reynolds number of the order of $10^4 - 10^5$ and cambered airfoil profiles. Here, instead we consider butterflies that mostly operate at Reynolds numbers in the range of 5000-9000 with sharper and flatter profiles.

Some recent studies contributed in gaining some insights about the flight of butterflies ([23]). In [37] tethered-flight experiments in laboratory conditions have been carried out, whereas in [22] various specimens of different *Morpho* species have been recorded while flying in a large insectary (8 m x 4 m x 2.5 m). An interesting work on gliding flight in butterflies was proposed in [46], where artificial wing models with various shapes were tested in a wind tunnel, varying angle of attack and configuration of the fore and hind wings. Numerical simulations are also proposed to reproduce experimental results using computational fluid dynamics. Another at-

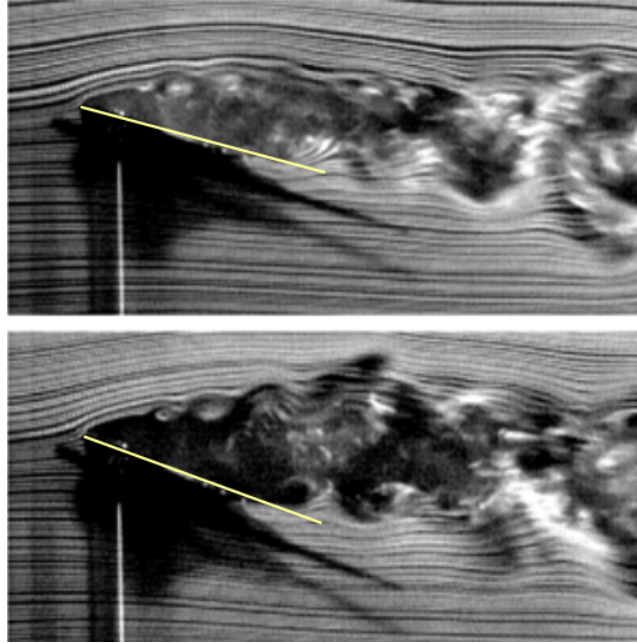


Figure 1.4.: Reproduction of a Swallowtail butterfly aerodynamics in a wind tunnel. Angles of attack of 10 (top) and 15 (bottom) degrees. The Reynolds number, with respect to the mean chord length, is in the range 5760-8640. Source: [39].

tempt to study the flow characteristics surrounding a gliding butterfly is presented in [39], where a wing model of a swallowtail butterfly -which has dimensions similar to *Morphos*- is observed in a wind tunnel. The reported visualisations of the latter (see Figure 1.4) provide interesting insights about the flow surrounding the wing, with separation taking place at the leading edge, reattachment for low attack angles and development of turbulent structures on and downstream the wing.

The analysis of flapping flight phase is much more complicated than the one of gliding flight. To gain an insights about how to deal with it, we have to leave the specific niche of butterflies in favour of the broader world of insect flight, where flapping and hovering flight has been widely dissected ([44, 14, 25, 51]). While flapping, an insect moves the wings following rapid oscillatory patterns that produce unsteady air flows over the wing. To understand the connections that bond the aerodynamic forces to the complex movements of the wings during flapping, different physic mechanisms have been observed, studied and modelled ([14, 44]). A possible approach to the problem is represented by the combination of models of separate aerodynamic mechanisms to build a comprehensive simulation of the various sources ([25, 51]).

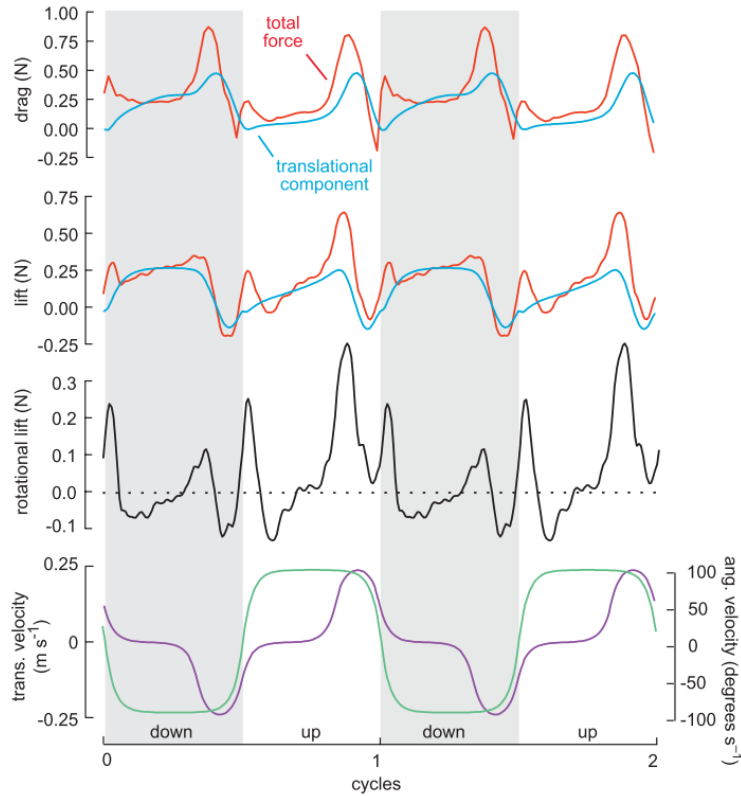


Figure 1.5.: Time history of lift and drag forces during a flapping wingbeat of an artificial reproduction of *Drosophila*. Measured forces in red, forces predicted by translation force coefficients in blue and rotational lift in black. Translational (green) and rotational (purple) velocities of the wing at the bottom. Source: [9].

Among the mechanisms accountable for the often unexpected high performances of insects flight, of particular importance is the leading edge vortex (LEV) ([14, 44]). In [25] it is shown that the LEV remains stably attached on a wing model that revolves around its base, despite it is shed, and thus not anymore capable of enhancing the aerodynamic performances of the animal, after a few chord lengths of travel on a translating model of the wing. Similarly, the experiments performed in [9] show the importance of wing rotation in the production of forces that keep insects aloft. In this latter work, a wing model of *Drosophila* is used to reproduce the flapping movement of the insect; the history of drag and lift forces during a wingbeat is then decomposed into transitional and rotational component, highlighting the importance of the latter (see Figure 1.5).

For this study two different setups has been taken into account: one for gliding

flight, where the wing lies fixed in a box-shaped domain and is invested by the air flow (a setup comparable to the one used in [46, 39]), and one for flapping flight, which reproduces the rotational setup used in [25], with the wing lying in a cylindrical domain and revolving around its hinge in still air.

1.2. Mathematical Modelling and Numerical Methods

The following section reports the physical equations describing the dynamics of fluids and their interaction with immersed bodies immersed along with some of the models developed to solve the resulting differential problem. A broad literature is available on this topic, with a variety of different approaches having different efficiencies, fields of application computational costs and other intrinsic characteristics. Here we discuss only the methods that have been used for the simulations of the present work.

1.2.1. The Navier-Stokes equations

The flow surrounding and aerofoil immersed in a Newtonian fluid (like air) is governed by the Navier-Stokes equations ([2, 50]). At low speeds, as it is the case for this study, we can assume that compressibility of the flow is negligible ([2]), and thus refer to the continuity equation and the incompressible Navier-Stokes equations; for $i,j=1,\dots,3$ and summing over repeated indexes:

$$\frac{\partial u_i}{\partial x_i} = 0, \tag{1.1}$$

$$\frac{\partial u_i}{\partial t} + u_j \frac{\partial u_i}{\partial x_j} = -\frac{1}{\rho} \frac{\partial p}{\partial x_i} + \nu \frac{\partial^2 u_i}{\partial x_j \partial x_j}, \tag{1.2}$$

where $[u_1(\mathbf{x}, t), u_2(\mathbf{x}, t), u_3(\mathbf{x}, t)]$ is the velocity field of the flow, p is the pressure field, ρ is the density and ν the kinematic viscosity of the fluid; the latter two are considered to be constant in the present work.

1.2.2. Reynolds Number: dynamical similarity

We will now introduce two quantities characteristic of the phenomenon we are studying: the length (L) and velocity (U) scales. This two quantities are meant to describe the size of the apparatus we are considering and the rate at which the fluid is moving through it ([50, Chapter 7]. For our case, L represents the mean chord length of the

wing and U the free-stream velocity of the flow. We can now use these values to turn the quantities at stake in dimensionless equations, by defining:

$$\tilde{u}_i = \frac{u_i}{U}, \quad \tilde{x}_i = \frac{x_i}{L}, \quad \tilde{t} = t \frac{U}{L}, \quad \tilde{p} = \frac{p}{\rho U^2}. \quad (1.3)$$

And replacing them in (1.2) and (1.1), we obtain:

$$\frac{U}{L} \frac{\partial \tilde{u}}{\partial \tilde{x}_i} = 0, \quad (1.4)$$

$$\frac{U^2}{L} \frac{\partial \tilde{u}_i}{\partial \tilde{t}} + \frac{U^2}{L} \left(\tilde{u}_j \frac{\partial \tilde{u}_i}{\partial \tilde{x}_j} \right) = - \frac{U^2}{L} \frac{\partial \tilde{p}}{\partial \tilde{x}_i} + \frac{U}{L^2} \nu \frac{\partial^2 \tilde{u}_i}{\partial \tilde{x}_j \partial \tilde{x}_j}, \quad (1.5)$$

which finally yields:

$$\frac{\partial \tilde{u}}{\partial \tilde{x}_i} = 0, \quad (1.6)$$

$$\frac{\partial \tilde{u}_i}{\partial \tilde{t}} + \left(\tilde{u}_j \frac{\partial \tilde{u}_i}{\partial \tilde{x}_j} \right) = - \frac{\partial \tilde{p}}{\partial \tilde{x}_i} + \frac{1}{Re} \frac{\partial^2 \tilde{u}_i}{\partial \tilde{x}_j \partial \tilde{x}_j}, \quad (1.7)$$

where $Re = UL/\nu$ is the *Reynolds Number*. If we now consider two geometrically similar setups -meaning that one is just a scaled-up version of the other-, if they have the same Reynolds Number, then the equations for the non-dimensional variables are the same, and the problems have the same solutions and flow patterns ([50, Chapter 7]). The Reynolds Number is thus a global parameter of great importance, since it gives full information about the case studied, without any need to study the inference of the other parameters (L , U , ρ , ν).

The Reynolds Number also has an important physical interpretation, since it can be seen as the ratio between the *inertia forces* and the *viscous forces* thus playing a fundamental role in defining the pattern of the flow topology.

1.2.3. The problem of turbulence

At low Reynolds regimes the flow pattern is simple and tidy. The streamlines of fluid particles are smooth and arranged in layers that don't mix with each other. With the increase of the Reynolds number this heavenly situation eventually comes to an end, due to small instabilities that start to mix such layers, entangling and ravelling them, bringing the flow to a chaotic state where velocities and pressure at every point are characterised by sudden and random variations. This process of slowly and incrementally mixing and stirring the flow is called *transition to turbulence* and the final state of chaos and randomness that follows it is called *turbulence*. The bond

between the Reynolds Number and the state of the flow (laminar or turbulent) is clear and straightforward, even though the value of Re at which transition is kicked depends on a wide range of factors ([2, 50, 32]).

There is no definition on turbulent flow, but we can still frame it listing its most characteristic features ([6, Chapter 1], [48, Chapter 1]):

1. **Irregularity.** Any turbulent flow is highly irregular; the streamlines of fluid particles are chaotic and highly entangled. The flow is made up of a spectrum of different time and length scales (eddy sizes), some of them assuming a particularly specific role. Such spectrum is bounded from above by the size of the flow geometry and from below by the viscous forces exerted by molecular viscosity.
2. **Diffusivity.** Turbulent motion has the outstanding ability to transport or mix momentum, kinetic energy, heat, with rates of transfer and mixing several orders of magnitude higher than the ones characteristic of laminar flow. This high diffusivity has several effects on the flow pattern and on the generation of forces.
3. **Large Reynolds Numbers.** As previously said, turbulence is highly related to the Reynolds number. Transition to turbulence is also case-dependent though, occurring at different Reynolds numbers for different geometries and conditions.
4. **Three-Dimensional.** Turbulence is always a three-dimensional phenomenon. That said, modelling turbulence with time-averaging can bring to two-dimensional flows.
5. **Dissipation.** Turbulence is a process that dissipates kinetic energy. In particular, the largest eddies gain energy from the mean flow, which is then transferred to smaller scale eddies, which in turn transfer it to smaller eddies; this cascade process eventually brings kinetic energy to the smaller scales, where the action of viscous forces turn it into internal energy. The whole process that brings energy from the largest scales to the smallest is called *cascade process*.

As the flows becomes more turbulent, the spectrum of scales widens and the smallest scale decreases. In particular, it can be demonstrated (see [7]) that the

relation between the length of the smallest scale of turbulence (also referred to as *Kolmogorov microscales* and written as η) and the Reynolds number is the following:

$$\eta = Re^{-3/4}l, \quad (1.8)$$

where l is the size of the large energy-containing eddies. When it comes to discretise the spatial and temporal domain of a problem to perform numerical simulations, in order to accurately reproduce the flow and all the phenomena concerning it, a resolution that catches all the scales of the phenomenon is needed. Therefore, the higher the Reynolds numbers -and, consequently, the smaller the smallest scales of turbulence- the finer the discretisation needed. In practical terms, this means that in most cases computational costs are prohibitive (see [7, p. 423-424]) and alternative solutions must be adopted in order to be able to properly simulate the problem under consideration at a reasonable cost. This problem leads to the question of how to accurately model turbulence without directly resolving it.

1.2.4. The time-averaged Navier-Stokes equations

Although turbulent flows are chaotic, they are deterministic and described by the Navier-Stokes equation which, as said, in most cases cannot be directly numerically solved. To overcome this problem, when analyzing a turbulent flow it can be useful to decompose the instantaneous variables (velocity components and pressure) into a mean and a fluctuating value ([48, 6, 53, 7]):

$$\begin{aligned} u_i &= \bar{u}_i + u'_i \\ p &= \bar{p} + p', \end{aligned} \quad (1.9)$$

where \bar{u}_i , \bar{p} denote the time averaged value defined by:

$$\bar{u}_i = \frac{1}{2T} \int_{-T}^T u_i dt, \quad (1.10)$$

where T is a sufficiently large time interval. Averaging (1.9) in time yields:

$$\bar{u}_i = \overline{\bar{u}_i + u'_i} = \bar{u}_i + \overline{u'_i}, \quad (1.11)$$

since $\overline{\bar{u}_i} = \bar{u}_i$. Operating similarly on p we obtain:

$$\overline{u'_i} = 0, \quad \overline{p'} = 0. \quad (1.12)$$

Insert Equation (1.9) into (1.1) and time-averaging, we find ([6]):

$$\frac{\partial(\overline{u_i + u'_i})}{\partial x_i} = \frac{\partial \bar{u}_i}{\partial x_i}. \quad (1.13)$$

With the same process for the Navier-Stokes equations we find:

$$\underbrace{\frac{\partial(\overline{u_i + u'_i})}{\partial t}}_{T1} + \underbrace{(\bar{u}_j + u'_j) \frac{\partial(\overline{u_i + u'_i})}{\partial x_j}}_{T2} = -\frac{1}{\rho} \underbrace{\frac{\partial(\overline{p + p'})}{\partial x_i}}_{T3} + \nu \underbrace{\frac{\partial^2(\overline{u_i + u'_i})}{\partial x_j \partial x_j}}_{T4}. \quad (1.14)$$

We will now discuss each term of the last equation separately, as in [6]. The first term (**T1**) results in:

$$\frac{\partial(\overline{u_i + u'_i})}{\partial t} = \frac{\partial \bar{u}_i}{\partial t} + \frac{\partial \overline{u'_i}}{\partial t} = \frac{\partial \bar{u}_i}{\partial t}.$$

Note that, in case of a steady mean flow, this term is zero. The second term (**T2**) gives:

$$(\bar{u}_j + u'_j) \frac{\partial(\overline{u_i + u'_i})}{\partial x_j} = \bar{u}_j \frac{\partial \bar{u}_i}{\partial x_j} + u'_j \frac{\partial \bar{u}_i}{\partial x_j} + \bar{u}_j \frac{\partial u'_i}{\partial x_j} + u'_j \frac{\partial u'_i}{\partial x_j},$$

and using $\overline{u_i u_j} = \bar{u}_i \bar{u}_j$, $\overline{u_i u'_j} = \bar{u}_i \overline{u'_j} = 0$ and $\overline{u_j u'_i} = \bar{u}_j \overline{u'_i} = 0$ (see [6, Chapter 8]) we finally find:

$$(\bar{u}_j + u'_j) \frac{\partial(\overline{u_i + u'_i})}{\partial x_j} = \bar{u}_j \frac{\partial \bar{u}_i}{\partial x_j} + u'_j \frac{\partial \bar{u}_i}{\partial x_j} = \bar{u}_j \frac{\partial \bar{u}_i}{\partial x_j} + \frac{\partial u'_j u'_i}{\partial x_j} - \bar{u}_i \frac{\partial \bar{u}_j}{\partial x_j},$$

with the last term being equal to zero thanks to the continuity equation. The third term (**T3**) results in:

$$\frac{\partial(\overline{p + p'})}{\partial x_i} = \frac{\partial \bar{p}}{\partial x_i}.$$

The fourth term (**T4**) results in:

$$\frac{\partial^2(\overline{u_i + u'_i})}{\partial x_j \partial x_j} = \frac{\partial^2 \bar{u}_i}{\partial x_j \partial x_j}.$$

This brings to the time averaged continuity equation and Navier-Stokes equations (typically called Reynolds-Averaged Navier-Stokes equations, in short RANS):

$$\frac{\partial \bar{u}_i}{\partial x_i} = 0, \quad (1.15)$$

$$\frac{\partial \bar{u}_i}{\partial t} + \bar{u}_j \frac{\partial \bar{u}_i}{\partial x_j} = -\frac{1}{\rho} \frac{\partial \bar{p}}{\partial x_i} + \frac{\partial}{\partial x_j} \left(\nu \frac{\partial \bar{u}_i}{\partial x_j} - \overline{u'_i u'_j} \right). \quad (1.16)$$

These equations look very similar to the original Equations (1.1) and (1.2) if we don't consider the average operator, exception made for the second part of the last term, which is new and, when multiplied by the density, goes with the name *Reynolds stress tensor*:

$$\tau_{ij} = -\rho \overline{u'_i u'_j}. \quad (1.17)$$

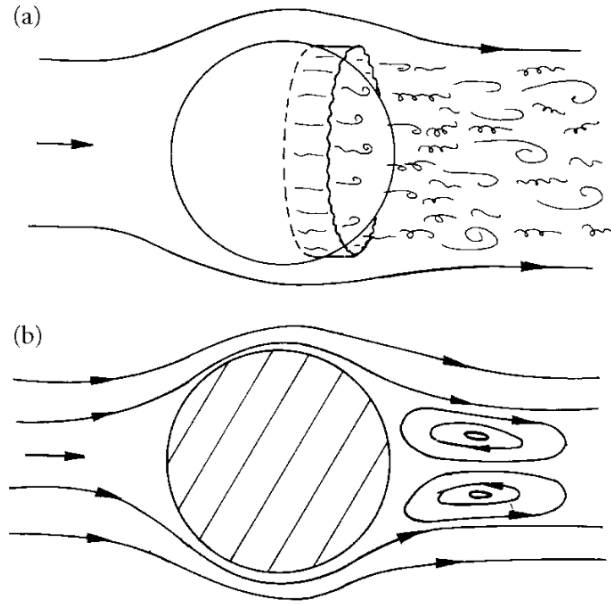


Figure 1.6.: Representation of flow over a sphere at $Re = 2 \times 10^4$: (a) real topology of the flow and (b) time-averaged flow pattern (as it could be seen in a time-lapse photograph). Source: [6].

Such tensor is symmetric and represents the correlation between fluctuating velocities: if $\overline{u'_i u'_j} \neq 0$ u'_i and u'_j are said to be *correlated*, otherwise they are said to be *uncorrelated* ([48]). The Reynolds stress tensor is an additional term related to turbulence, and brings six new unknowns, meaning that we need a model for $\overline{u'_i u'_j}$ to close the equation system, which now has ten variables (three velocity components, pressure, six Reynolds stress tensor components) but still only four equations. This is known as the *closure problem*. Note that the continuity equation applies both for the instantaneous velocity u_i and the time-averaged term \bar{u}_i , therefore it holds also for the fluctuating velocity term u'_i ([6]):

$$\frac{\partial u'_i}{\partial x_i} = 0. \quad (1.18)$$

The last term of Equation (1.16) represents the divergence of the total stress tensor ([18]). The first part is related to the net momentum flux by molecular motions, while the second part is the net flux of the momentum $\rho u'_i$ by the macroscopic velocity fluctuations u'_j . The molecular contribute to the stress tensor can be written as:

$$-p\delta_{ij} + \mu \left(\frac{\partial u_i}{\partial x_j} + \frac{\partial u_j}{\partial x_i} \right), \quad (1.19)$$

where $\mu = \nu\rho$ is the *dynamic viscosity*.

With the Reynolds-averaged formulation of the Navier-Stokes equations it is possible to define a useful quantity, the *turbulent kinetic energy* (per unit mass) as:

$$k = \frac{1}{2} \overline{u'_k u'_k}. \quad (1.20)$$

1.2.5. The Boussinesq assumption

As said, a model is necessary for the Reynolds stress tensor in order to solve the system of equations describing the flow. One of the most popular models was introduced by Boussinesq and is based on the introduction of an eddy viscosity to reproduce the role of the $\overline{u'_i u'_j}$ terms. We start considering the diffusion terms in Equation (1.16), with an explicit formulation of the viscous stress (we assume ν is non-constant for the moment):

$$\frac{\partial}{\partial x_j} \left(\nu \left(\frac{\partial \bar{u}_i}{\partial x_j} + \frac{\partial \bar{u}_j}{\partial x_i} \right) - \overline{u'_i u'_j} \right). \quad (1.21)$$

We define the Reynolds stress tensor terms as:

$$-\overline{u'_i u'_j} = \nu_t \left(\frac{\partial \bar{u}_i}{\partial x_j} + \frac{\partial \bar{u}_j}{\partial x_i} \right), \quad (1.22)$$

where ν_t is called *kinematic turbulent viscosity* ($[\text{m}^2/\text{s}]$) and we use it in Equation (1.21), thus yielding:

$$\frac{\partial}{\partial x_j} \left((\nu + \nu_t) \left(\frac{\partial \bar{u}_i}{\partial x_j} + \frac{\partial \bar{u}_j}{\partial x_i} \right) \right). \quad (1.23)$$

The definition given in Equation (1.22) is not valid upon contraction ([6]), as the right term is zero when $i = j$; for this reason we add the trace of the left side to the right side obtaining:

$$\overline{u'_i u'_j} = -\nu_t \left(\frac{\partial \bar{u}_i}{\partial x_j} + \frac{\partial \bar{u}_j}{\partial x_i} \right) + \frac{1}{3} \delta_{ij} \overline{u'_k u'_k} = -2\nu_t \bar{s}_{ij} + \frac{2}{3} \delta_{ij} k. \quad (1.24)$$

The former equation is known as *Boussinesq assumption*. It will be useful in the future to underline that the definition given in Equation (1.17) can be written as:

$$\tau_{ij} = 2\mu_t \bar{s}_{ij} - \frac{2}{3} \delta_{ij} k. \quad (1.25)$$

Thus, this model is thus replacing the six turbulent stresses with one new unknown, the turbulent viscosity ν_t . With such assumption Equation (1.16) reads:

$$\frac{\partial \bar{u}_i}{\partial t} + \bar{u}_j \frac{\partial \bar{u}_i}{\partial x_j} = -\frac{1}{\rho} \frac{\partial \bar{p}_B}{\partial x_i} + \frac{\partial}{\partial x_j} \left((\nu + \nu_t) \frac{\partial \bar{u}_i}{\partial x_j} \right), \quad (1.26)$$

where $\bar{\rho}_B = \bar{\rho} + 2k/3$. It is important to remember that ν is a property of the fluid, whilst ν_t is a variable dependent on the flow, which means that it is function of time and space: $\nu_t = \nu_t(t, x_i)$.

With this assumption we have a set of four equations and five variables; many different models have been developed starting from the ReBoussinesq hypothesis. They differ from each other in the way of defining the function ν_t and in the number of equations added to close the problem. In the present work, the turbulence models used are the *Spalart – Allmaras* model ([47]) and the SST $\kappa - \omega$ model ([30]).

1.2.6. The Spalart-Allmaras model

The *Spalart – Allmaras* model ([47]) is a 1-equation model (meaning that one equation is added to the starting system of Equations (1.15) and (1.26) to solve it) which defines the turbulent viscosity by means of an auxiliary viscosity $\tilde{\nu}$ and an auxiliary function f_{v1} ([26, Chapter 8]):

$$\nu_t = \tilde{\nu} f_{v1}. \quad (1.27)$$

The equation added to the system is the transport equation for $\tilde{\nu}$:

$$\begin{aligned} \frac{\partial \tilde{\nu}}{\partial t} + u_j \frac{\partial}{\partial x_j} &= c_{b1}(1 - f_{v1})\tilde{S}\tilde{\nu} \\ &+ \frac{1}{\sigma} \left(\frac{\partial}{\partial x_j} (\nu + \tilde{\nu}) \frac{\partial \tilde{\nu}}{\partial x_j} \right) + c_{b2} \frac{\partial \tilde{\nu}}{\partial x_j} \frac{\partial \tilde{\nu}}{\partial x_j} \\ &- \left(c_{w1} f_w - \frac{c_{b1}}{k^2} f_{t2} \right) \left(\frac{\tilde{\nu}}{d} \right)^2 + f_{t1} \Delta U^2. \end{aligned} \quad (1.28)$$

In the right hand side, the first term represents the *production term*, the second the *diffusion term*, the third the *dissipation term* and a *transition related term*. The coefficients are:

$$\begin{aligned} c_{b1} &= 0.1335, \quad c_{b2} = 0.622, \quad \sigma = \frac{2}{3}\kappa = 0.41, \\ c_{w1} &= \frac{c_{b1}}{\kappa^2} + \frac{1 + c_{b2}}{\sigma}, \quad f_w = g \left(\frac{1 + c_{w3}^6}{g^3 + c_{w3}^6} \right)^{\frac{1}{6}}, \quad c_{w2} = 0.3, \\ c_{w3} &= 2, \quad r \equiv \frac{\tilde{\nu}}{\tilde{S}\kappa^2 d^2}, \quad g = r + c_{w2}(r^6 - r). \end{aligned} \quad (1.29)$$

The auxiliary functions related to the flow close to wall are:

$$\begin{aligned} \tilde{S} &= S + \frac{\tilde{\nu}}{\kappa^2 d^2} f_{v2}, \quad S = \sqrt{2\bar{s}_{ij}\bar{s}_{ji}}, \quad \chi \equiv \frac{\tilde{\nu}}{\nu}, \\ f_{v1} &= \frac{\chi^3}{\chi^3 + c_{v1}^3}, \quad f_{v2} = 1 - \frac{\chi}{1 + \chi f_{v1}}, \quad c_{v1} = 7.1. \end{aligned} \quad (1.30)$$

The function connected to the transition related term are given by:

$$\begin{aligned} f_{t1} &= c_{t1} g_t \exp\left(-c_{t2} \frac{w_t^2}{\Delta U^2} \left(d^2 + (g_t d_t)^2\right)\right), & f_{t2} &= c_{t3} \exp(-c_{t3} \chi^2), \\ g_t &= \min\left(0.1, \frac{\Delta U}{\omega_t \Delta x_t}\right), & c_{t1} &= 1, \quad c_{t2} = 2, \quad c_{t3} = 1.2, \quad c_{t4} = 0.5. \end{aligned} \quad (1.31)$$

Here ω_t is the vorticity, ΔU the norm of the difference between the velocity at the transition and the velocity at any field point, Δx_t the grid size along the wall at the transition point and d the distance to the wall.

1.2.7. The $k - \omega$ and SST $k - \omega$ models

The original $k - \omega$ model was introduced by David Wilcox in 1988 ([52]; it introduces two transport equation to close the system represented by Equations (1.15) and (1.26), one for the turbulent kinetic energy k and one for the characteristic frequency of turbulence, ω). This model defines eddy viscosity as:

$$\nu_t = \frac{k}{\omega}. \quad (1.32)$$

The equations that define the model are:

- *Turbulent kinetic energy k equation:*

$$\frac{\partial k}{\partial t} + \bar{u}_j \frac{\partial k}{\partial x_j} = \tau_{ij} \frac{\partial \bar{u}_i}{\partial x_j} - \beta^* k \omega + \frac{\partial}{\partial x_j} \left((\nu + \sigma^* \nu_t) \frac{\partial k}{\partial x_j} \right), \quad (1.33)$$

- *Specific dissipation rate ω equation:*

$$\frac{\partial \omega}{\partial t} + \bar{u}_j \frac{\partial \omega}{\partial x_j} = \alpha \frac{\omega}{k} \tau_{ij} \frac{\partial \bar{u}_i}{\partial x_j} - \beta \omega^2 + \frac{\partial}{\partial x_j} \left((\nu + \sigma^* \nu_t) \frac{\partial \omega}{\partial x_j} \right), \quad (1.34)$$

where P_k is called *rate of production of turbulent kinetic energy* ([26]) and is defined as:

$$P_k = \tau_{ij} \frac{\partial \bar{u}_i}{\partial x_j}. \quad (1.35)$$

Writing as Δ_y the distance between the cell center of the first cell adjacent to the wall and the wall itself, the boundary conditions for the model at the wall are:

$$k = 0, \quad \omega = 10 \frac{6\nu}{\beta(\Delta y)^2}, \quad (1.36)$$

and the conditions outside the boundary layer are:

$$\omega_\infty = \lambda \frac{\bar{u}_{ref}}{L_{ref}}, \quad \nu_{t_\infty} = 10^{-3} \nu, \quad k_\infty = \nu_{t_\infty} \omega_\infty, \quad (1.37)$$

U_{ref} and L_{ref} being reference quantities and λ a parameter varying from 1 to 10. This model has been revisited in terms of coefficients by David Wilcox in 1998 ([53]); moreover, in 1993 Menter introduced a variation of it, called *Shear Stress Transport* (SST) $k - \omega$ model ([31]). This new version is characterised by the new following equations for k and ω :

$$\frac{\partial k}{\partial t} + \bar{u}_j \frac{\partial k}{\partial x_j} = P_k - \beta^* k \omega + \frac{\partial}{\partial x_j} \left((\nu + \sigma_\omega \nu_t) \frac{\partial k}{\partial x_j} \right), \quad (1.38)$$

$$\begin{aligned} \frac{\partial \omega}{\partial t} + \bar{u}_j \frac{\partial \omega}{\partial x_j} = P_\omega - \beta \omega^2 + \frac{\partial}{\partial x_j} \left((\nu + \sigma_\omega \nu_t) \frac{\partial \omega}{\partial x_j} \right) \\ + 2(1 - F_1) \frac{\sigma_{\omega 2}}{\omega} \frac{\partial k}{\partial x_j} \frac{\partial \omega}{\partial x_j}. \end{aligned} \quad (1.39)$$

Where the production term P_ω is defined as:

$$P_\omega = \frac{\alpha}{\mu_t} P_k. \quad (1.40)$$

In the various versions of the model given, various different closure coefficients were proposed ([30, 53]); the ones used in the present work were presented in the most recent SST $k - \omega$ version, and are the following:

$$\begin{aligned} F_1 = \tanh(\arg^4), \quad \arg = \min \left(\max \left(\frac{\sqrt{k}}{\beta^* \omega d}, \frac{500\nu}{d^2 \omega} \right), \frac{4\rho\sigma_{\omega 2} k}{CD_{k\omega} d^2} \right), \\ CD_{k\omega} = \max \left(2\rho\sigma_{\omega 2} \frac{1}{\omega} \frac{\partial k}{\partial x_i} \frac{\partial \omega}{\partial x_i}, 1 \times 10^{-10} \right), \end{aligned} \quad (1.41)$$

where d is the distance from the wall and:

$$\begin{aligned} \alpha = F_1 \alpha_1 + (1 - F_1) \alpha_2, \quad \beta = F_1 \beta_1 + (1 - F_1) \beta_2, \\ \sigma_k = F_1 \sigma_{k1} + (1 - F_1) \sigma_{k2}, \quad \sigma_\omega = F_1 \sigma_{\omega 1} + (1 - F_1) \sigma_{\omega 2}, \end{aligned} \quad (1.42)$$

with:

$$\begin{aligned} \beta^* = 0.09, \quad \alpha_1 = 5/9, \quad \beta_1 = 0.075, \quad \sigma_{k1} = 0.85, \quad \sigma_{\omega 1} = 0.5, \\ \alpha_2 = 0.44, \quad \beta_2 = 0.0828, \quad \sigma_{k2} = 1.0, \quad \sigma_{\omega 2} = 0.856, \end{aligned} \quad (1.43)$$

and the eddy viscosity ν_t defined by:

$$\begin{aligned} \nu_t = \frac{a_1 k}{\max(a_1 \omega, F_2 S)}, \quad a_1 = 0.31, \\ F_2 = \tanh(\arg_2^2), \quad \arg_2 = \max \left(\frac{2\sqrt{k}}{0.09\omega d}, \frac{500\nu}{\omega d^2} \right) \end{aligned} \quad (1.44)$$

with $S = \sqrt{2\bar{s}_{ij}\bar{s}_{ij}}$ and Ω is the absolute value of the vorticity.

The SST $k - \omega$ is a blending of the $k - \epsilon$ ([26, 41]) and $k - \omega$ models, since close to the wall $F_1 = 1$, meaning the model is working as a $k - \epsilon$, and $F_1 = 0$ far from the

walls, meaning the model is working as a $k-\omega$. To prevent the rising of turbulence in stagnation points, the production term P_k is bounded from above using the modified production term:

$$\tilde{P}_k = \min(P_k, 10\beta^* \rho k \omega). \quad (1.45)$$

1.2.8. Transition modelling

All the previously mentioned models are developed to reproduce the effects of turbulence but they have been developed based on the assumption that turbulence in the flow is fully developed. For certain situations, in particular for low Reynolds numbers, it can be argued that the phenomenon of transition from laminar to turbulent flow plays a major role. The transition consists of the generation of small perturbations that drive a laminar flow towards a turbulent state; it is a very delicate process ([20, 50, 40]) and it has been a great challenge to formulate proper models to catch it and its consequences. In the present work we consider and use the $\gamma - Re_\theta$ model developed by Florian Menter and Robin Langtry ([32, 21]) in 2004. The model consists in adding two transport equations to the SST $k-\omega$ model, one for the *intermittency* γ and one for the *Reynolds momentum thickness*, which is defined as:

$$Re_\theta = \frac{\max(Re_v)}{2.193}, \quad (1.46)$$

where Re_v is the *strain rate Reynolds number*:

$$Re_v = \frac{\rho y_n^2}{\mu} S, \quad (1.47)$$

with S defined as in Equation (1.30) and $y_n^2 = d$ being the distance from the wall. Outcomes of these two equations are then used inside the k equation being thus embedded in the SST $k-\omega$ model. Due to its complexity the formulation of the model is not reported here, but can be found in [32, 21] and [20, 26].

1.2.9. Partially averaged Navier-Stokes equations

The RANS models proved to predict the mean flow statistics with adequate accuracy for many engineering applications, although the range of flow physics that can be adequately represented by these models is limited. Many different turbulence models have been developed to resolve all or most of the dynamically important scales of motion ([26, 7, 53]), like *Large Eddy Simulation* (LES), *Detached Eddy Simulation*

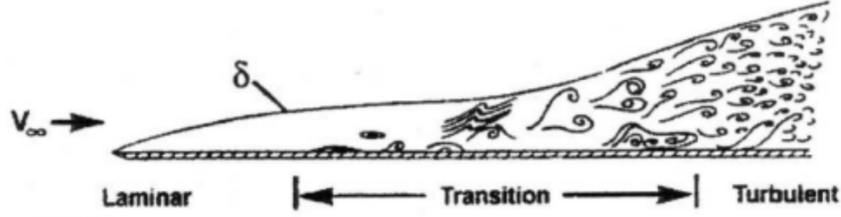


Figure 1.7.: A representation of transition to turbulence on a flat plate. δ is the boundary layer thickness and V_∞ the free stream velocity. Source: [45].

(DES) or *Direct Navier-Stokes Simulation* (DNS). As in most of engineering tools, accuracy comes at a cost, that is, in many cases unbearable and/or unjustified. In this work we will make use of another high accuracy model, the *Partially Averaged Navier-Stokes equations* (PANS), introduced by Sharath Girimaji in 2006 ([15]). PANS is a suite of turbulence closure models of various modeled-to-resolved scale ratios ranging from RANS to DNS. The modelled-to-resolved scale ratio or the level of physical resolution in PANS is quantified by two parameters: the unresolved-to-total ratios of kinetic energy f_k and dissipation f_ϵ . The unresolved stress is modelled with the Boussinesq approximation and modelled transport equations are solved for the unresolved kinetic energy and dissipation ([16]). The unresolved kinetic energy and dissipation equations are derived from a parent RANS model, in this case the SST $k-\omega$. PANS models of different f_k values require different numerical resolutions: the lower the f_k value, the smaller the finer time and space need to be discretized, with $f_k = 1$ representing RANS and $f_k = 0$ representing DNS. If we write the unresolved kinetic energy as k_u , the unresolved energy dissipation as ϵ_u and the unresolved specific dissipation as ω_u , we can define the PANS coefficients as:

$$f_k = \frac{k_u}{k}, \quad f_\omega = \frac{f_\epsilon}{f_k} = \frac{\omega_u}{\omega}. \quad (1.48)$$

These values are then embedded in the RANS equations (in this case the SST $k-\omega$). A full explanation of the model is given in [15, 16] and its implementation in the CFD solver used in this work is given in [26].

1.3. Numerical Errors and Uncertainty Estimation

The assessment of the quality and reliability of a numerical analysis is a fundamental step if we aim to issue a reliable work. Such procedure is commonly denoted

as *Verification & Validation*. Following [12], "Verification is a purely mathematical exercise that intends to show that we are 'solving the equations right', whereas Validation is science/engineering activity that intends to show that we are 'solving the right equations'. This means that Verification deals with numerical errors/uncertainties whereas Validation is concerned with modelling errors/uncertainties". Here we mention errors and uncertainties, but it is important to state clear that these are conceptually different: to define an error we need the knowledge of the 'true/exact solution', and such error has a sign; an uncertainty defines an interval in which the 'true/exact solution' should lie with a certain degree of confidence. It is usually accepted ([12]) that the numerical error of a CFD prediction has three components:

1. round-off error
2. iterative error
3. discretisation error.

The first comes as a direct consequence of the finite precision of computers and its relative importance tends to increase with grid refinement ([11, 12]). Iterative error is unavoidable due to the non-linearity of the Navier-Stokes equations. The discretisation error is a consequence of the approximations made to transform the partial differential equations of the continuum formulation into a system of algebraic equations, which are for us brought by the adoption of a finite-volume method approach. The latter source of error, unlike the others, tends to decrease refining the grid.

When we follow procedures to estimate the numerical error due to discretisation, we assume that the other two error sources are negligible. The round-off errors are unavoidable and their impact on the solution is difficult to estimate; for the present work we will assume that they are small compared to the others. The sensitivity to the iterative error will be discussed case by case. The discretisation error will be computed using the software suite developed following the procedure reported in [12]. The latter chooses as estimator for the discretisation error ϵ_ϕ with power series expansions:

$$\epsilon_\phi \simeq \delta_{RE} = \phi_i - \phi_0 = \alpha h_i^p. \quad (1.49)$$

ϕ_i stands for any integral or other functional of a local flow quantity, ϕ_0 is the estimate of the exact solution, α is a constant to be determined, h_i is a typical cell

size and p is the observed order of grid convergence. The index i refers to the i -th grid and for $i = 0$ we are referring to the finest grid. The estimation of ϵ_ϕ requires the determination of ϕ_0 , α and p . Therefore the minimum number of grids (n_g) required for the estimation of ϵ_ϕ is $p+1$.

The assumptions needed for the application of Equation (1.49) are ([12]):

1. ϕ does not include any singularities;
2. the grids must be in the 'asymptotic range'¹ to guarantee that the leading term of the power series expansion is sufficient to estimate the error;
3. the density of the grids is representable by a single parameter, the typical cell size of the grids, h_i ; this requires the grids to be geometrically similar, that is the grid refinement ratio must be constant in the complete field and grid properties must remain unaffected.

In practical problems -and the present in one of these- it is not possible to respect such constraints; to deal with these shortcomings in [12] three error estimators are proposed (considering from now on that $p = 2$, as it is for the discretisation method used in the present work):

$$\epsilon_\phi \simeq \delta_1 = \phi_i - \phi_0 = \alpha h_i, \quad (1.50)$$

$$\epsilon_\phi \simeq \delta_1 = \phi_i - \phi_0 = \alpha h_i^2, \quad (1.51)$$

$$\epsilon_\phi \simeq \delta_1 = \phi_i - \phi_0 = \alpha_1 h_i + \alpha_2 h_i^2. \quad (1.52)$$

These three alternatives are used when Equation (1.49) is not reliable, giving orders of convergence either too large or small. Equation (1.52) can be used also for non-monotonic convergence, whereas Equations (1.50) and (1.51) are suitable only for monotonically convergent solutions.

As reported in [12], it is suggested to use at least four grids to have a reliable estimation of the uncertainty. In such conditions ($n_g \geq 4$), it is possible to do the

¹This means that the grids used are fine enough to give a single dominant term in a power series expansion of the error.

error estimation in the least-square sense, that is determining ϕ_0 from the functions:

$$S_{RE}(\phi_0, \alpha, p) = \sqrt{\sum_{i=1}^{n_g} (\phi_i - (\phi_0 + \alpha h_i^p))^2} \quad (1.53)$$

$$S_1(\phi_0, \alpha) = \sqrt{\sum_{i=1}^{n_g} (\phi_i - (\phi_0 + \alpha h_i^p))} \quad (1.54)$$

$$S_2(\phi_0, \alpha) = \sqrt{\sum_{i=1}^{n_g} (\phi_i - (\phi_0 + \alpha h_i^2))^2} \quad (1.55)$$

$$S_{12}(\phi_0, \alpha_1, \alpha_2) = \sqrt{\sum_{i=1}^{n_g} (\phi_i - (\phi_0 + \alpha_1 h_i + \alpha_2 h_i^2))^2}. \quad (1.56)$$

The approach can be slightly modified if one may wish to give more value to the finer grid solutions, using weighting coefficients, and thus using the following functions instead:

$$S_{RE}^w(\phi_0, \alpha, p) = \sqrt{\sum_{i=1}^{n_g} w_i (\phi_i - (\phi_0 + \alpha h_i^p))^2} \quad (1.57)$$

$$S_1^w(\phi_0, \alpha) = \sqrt{\sum_{i=1}^{n_g} w_i (\phi_i - (\phi_0 + \alpha h_i^p))} \quad (1.58)$$

$$S_2^w(\phi_0, \alpha) = \sqrt{\sum_{i=1}^{n_g} w_i (\phi_i - (\phi_0 + \alpha h_i^2))^2} \quad (1.59)$$

$$S_{12}^w(\phi_0, \alpha_1, \alpha_2) = \sqrt{\sum_{i=1}^{n_g} w_i (\phi_i - (\phi_0 + \alpha_1 h_i + \alpha_2 h_i^2))^2}. \quad (1.60)$$

The weights W_i are based on the typical cell size:

$$w_i = \frac{\frac{1}{h_i}}{\sum_{i=1}^{n_g} \frac{1}{h_i}}, \quad (1.61)$$

for which the following holds:

$$\sum_{i=1}^{n_g} w_i = 1. \quad (1.62)$$

The least-square minimisation of the previous functions, together with data regressions are presented in [12].

2. Approach, Tools, Methodology

Nature, my friends, is the most surprising spectacle man can behold. Did you know ants have herds of livestock that give them milk and sugar? That spiders invented the submarine millions of years ago? Did you know that butterflies have tongues? The tongue of a butterfly is like an elephant's trunk, but very thin and wound up like a watch spring.

Don Gregorio, Butterfly's Tongue

2.1. Approach to the problem and main assumptions

The experimental data we refer to in this work ([22]) has been collected by the PhD candidate at the *Institute of Systematic, Evolution and Biodiversity* (ISYEB) Camille Le Roy, whom we raised a collaboration with. Mr. Le Roy spent several month in South America to gather and study various species of *Morpho* butterflies. Among the many specimen collected, some of them have been recorded while flying in a large insectary (8 m x 4 m x 2.5 m). The three-dimensional trajectories of this flights have been then reconstructed, thanks to the simultaneous use of several cameras. Tracking the positions of head and tail of the butterfly and of left and right wingtips allowed us to derive position, velocity and acceleration of the butterfly and the angles of attack of the wings.

Since the flight phases were recorded inside a closed insectary, we assume that during the filming the air was still and any currents had negligible effect on the trajectory drawn by the insects.

2.1.1. Modelling the wing

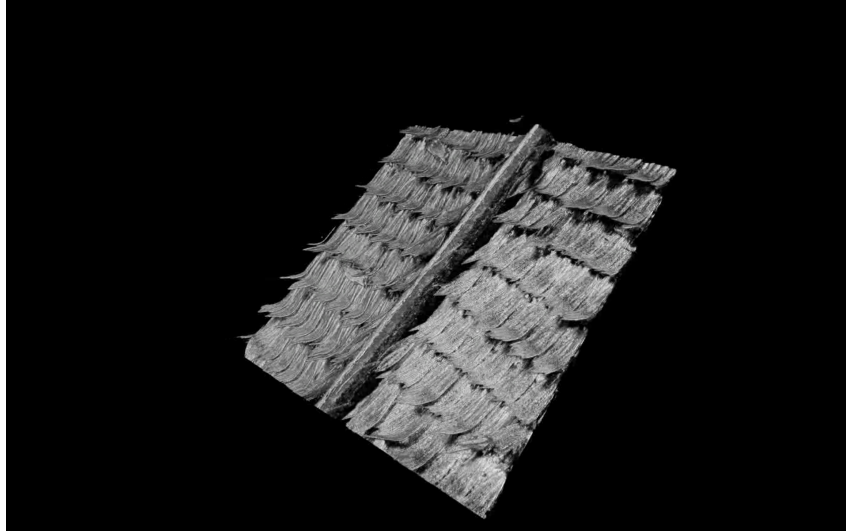
Morpho's wing shape has been studied in [22], together with the topology of its thickness. Each wing consists of a front and hind wing that can vary their mutual position. Using optical coherent tomography an important insight to the wing¹ thickness was given. The membrane separating the dorsal side from the ventral side is very thin and is covered with small scales which mostly curl upwards; when the scales are nearly flat, wing thickness is about 30-50 μm , whilst considering the distance between the tip of a scale and the tip of the corresponding scale on the opposite side, the thickness reaches values of around 100-150 μm . The wings are swept by veins, which represent the thickest parts of the wing itself, reaching values of 1 mm. Such veins are mostly allocated close to the leading edge of the wing.

The technology used to pull out this information is though too expensive to be applied to the entire wing, thus we don't have a comprehensive precise data of the behaviour of the thickness along the whole wing.

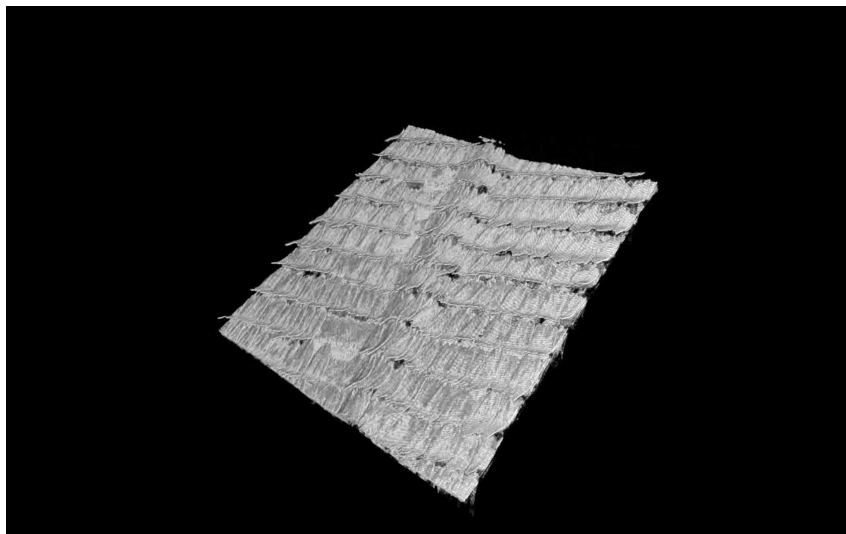
Here we model the wing starting from the configuration of the front and hind wings used by the butterfly during gliding flight; the two-dimensional shape is traced directly from the specimens gathered in [22], whereas the thickness is considered to be uniform and equal to 1 mm. The three-dimensional model of the wing (visible in Figure 2.2) is thus represented by a flat plate 1 mm thick shaped as mentioned, with the edges rounded with a half-circumference having 0.5 mm radius. Motivations for these assumptions are the following:

- the length-scale of wing scales represents an impossible target in terms of computational costs, geometry and meshing precision; moreover, the role of this scales in the aerodynamics of the butterfly are arguable, since their size, compared to the thickness of the expected boundary layer, is not sufficient to produce any appreciable changes in the flow ([3]);
- as previously mentioned, it is not within our means to extrapolate the topology of the whole wing's thickness;
- in terms of flow development, we believe that the most important parameter for thickness is its value at the leading edge, which, luckily, can be estimated

¹The specimen used for this measurements was a *Morpho cisseis*.



(a)



(b)

Figure 2.1.: Insight of a part of a *Morpho cisseis* wing: in (a) the ventral side and in (b) the dorsal side. Note the scales curling upwards (with a thickness of around $50\text{-}75\ \mu\text{m}$) and the vein sweeping the wing, having a thickness considerably larger than the rest of the wing (up to $1\ \text{mm}$).

with sufficient precision ([22]); thereby the decision of extending such thickness to the whole wing;

- according to [22], the front and hind wings are most of the time one pressed on the other, acting *de facto* as a single body.

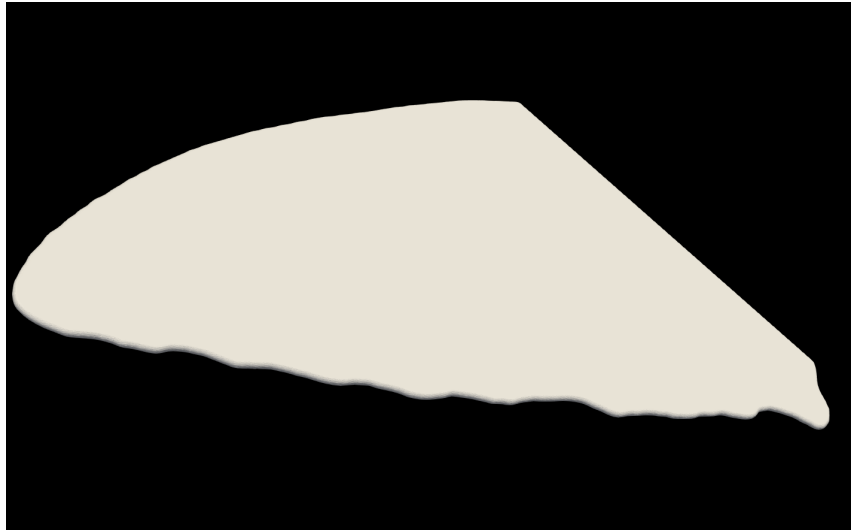
As a final remark, looking at Figure 1.2, where wing shape and half of the trunk of a *Morpho deidamia* is shown, it can be noticed that the latter is a tapered body with a surface area at least one order of magnitude smaller than that of the wing; thereby, we assume that the role of the butterfly's body has negligible effects in the production of aerodynamic forces and flow topology and thus we won't model it but we will consider only the wings.

2.1.2. Modelling gliding flight

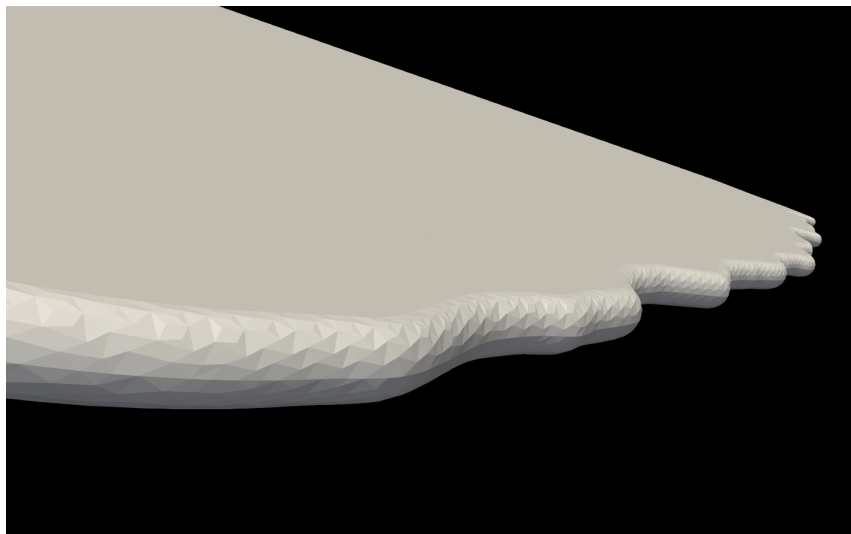
Gliding flight might be thought as a steady phenomenon, but this is not the case for *Morpho* butterflies. As expected, in order to maintain its gliding trajectory, the animal is continuously correcting its maneuvers: in Figure 2.3 the kinematic details of gliding trajectories of a *Morpho cisseis* and a *Morpho deidamia* are reported, showing smooth trends of position, velocity and acceleration, in contrast with quick changes of the angles of attack.

In the analysis of the gliding performances of the butterflies we will neglect this observation and we will perform the simulations with a fixed angle of attack, as also done in [46]. The motivations for this choice are the following:

- the changes in angle of attack are a consequence of the unsteadiness of the flow encountered by the butterfly and they clearly have a random and difficult-to-control nature; therefore, they are highly case-dependent and not reproducible: trying to simulate them would lead to a very specific result with scarce meaning and range of applicability;
- the purpose of this work is to investigate the mathematical models which are more promising to efficiently reproduce the flow patterns around butterfly wings and to look at the performances of different wings; from this perspective, we need a highly controllable setting that would allow us to keep track of all the parameters we want to investigate.



(a)



(b)

Figure 2.2.: 3D model of a *Morpho cisseis* wing: in (a) an overview of the full wing; in (b) a focus of the edge region.

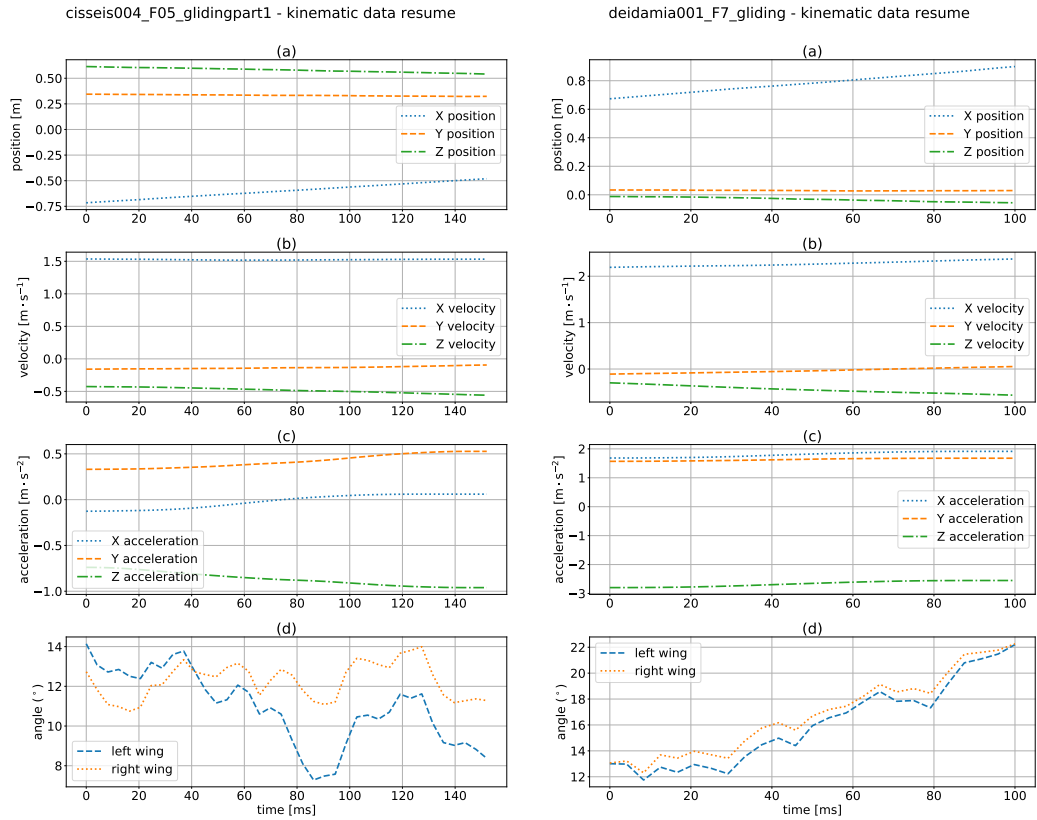


Figure 2.3.: Gliding trajectory of the specimens *cisseis004_F05_glidingpart1* and *deidamia001_F7*. In (a) the position field during the flight, in (b) the velocity field, in (c) the acceleration field and in (d) the angles of attack of the wings. Data source: [22].

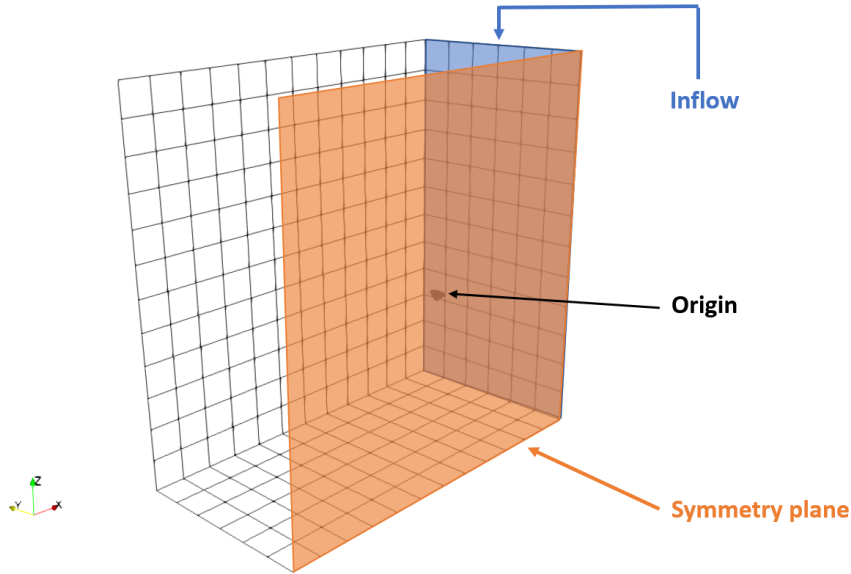


Figure 2.4.: Setup of a gliding simulation. The root of the wing is positioned on the symmetry plane.

In light of this considerations, all the simulations of gliding flight presented here have the following setup:

- domain: represented by a rectangular box, measuring 1 m in the y direction and 2 m in the x and z directions; the wing's root is laying on the $y = 0$ plane, with the leading tip of the hinge centered in the origin;
- boundary conditions: a symmetry plane is imposed on the $y = 0$ plane; an inflow velocity is set on the $x = 1$ plane, with direction reverse to the x axis; on the wing a no-slip condition is imposed, whereas the remaining surfaces are characterised by a zero-pressure condition;

such setup is the same used in [46] and is shown in Figure 2.4.

2.1.3. Modelling flapping flight

Reproducing the flapping flight of an insect represents a very complicated task. Moreover, the direct simulation of a flapping trajectory can represent a very interesting topic but also a honey trap when it comes to understanding where and how the forces at stake are generated. In fact, with this type of approach it is possible to observe the evolution of the flow surrounding the animal, but it is difficult to state which are the physical mechanisms responsible for the production of forces. For this

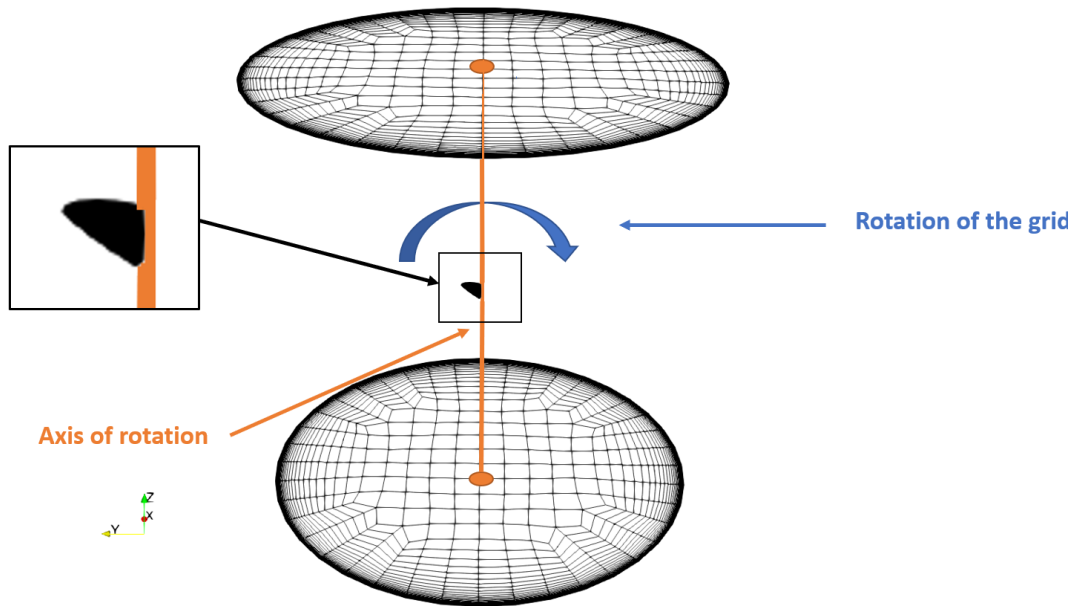


Figure 2.5.: Setup for the flapping simulations. The wing is positioned in the origin of the cylinder and rotates (together with the whole grid) around its hinge in still air.

reason, to evaluate the performance of flapping flight of *Morpho* butterflies, in this work we use CFD to reproduce the experimental pattern proposed in [9] and [25], using the following setup:

- domain: represented by a vertical cylinder, with a 1 m radius base and a height of 2 m; the leading tip of the hinge is centered in the origin of the circumference at half height;
- boundary conditions: on the wing a no-slip condition is imposed, whereas the remaining surfaces are characterised by a zero-pressure condition;

such setup is shown in Figure 2.5. The simulations are then run revolving the grid around the z axis for a total angle of 360° , to reproduce the experiments mentioned above.

2.1.4. Inverse dynamic model of a gliding butterfly

So far, we mentioned the experimental data collected in [22], but we didn't specify how we made use of it. When it comes to setting up the numerical simulations, in addition to the geometry of the wing, we use the data at our disposal for the inflow

velocity and the angle of attack of the wing. Furthermore, to validate the simulations performed, we developed a procedure to extrapolate from the flight kinematics some quantities that can be compared with the numerical results .

Since the flight phases were recorded inside a closed insectary, we assume that during the filming the air was still and any air current had negligible effects on the trajectory drawn by the insects. Under these circumstances, using an *inverse dynamics* approach, we can estimate the aerodynamic lift \mathbf{L} and drag \mathbf{D} acting on the animal at each time frame. To accomplish that, we start with a balance of the forces acting on the insect during its recorded flight using Newton's second law (see Figure 2.6):

$$m\mathbf{a} = m\mathbf{g} + \mathbf{F}_{\text{aero}}. \quad (2.1)$$

where m is the mass of the butterfly and \mathbf{g} is the gravitational acceleration. Here \mathbf{F}_{aero} represents the total aerodynamic force acting on the animal; since we know \mathbf{a} , we have all we need to define our unknown:

$$\mathbf{F}_{\text{aero}} = -m\mathbf{g} + m\mathbf{a}, \quad (2.2)$$

The next step consists in pulling the drag and lift vectors out of the \mathbf{F}_{aero} vector. The drag is defined as the aerodynamic force component in the free-stream airflow direction, and is thus calculated as:

$$\mathbf{D} = \langle \hat{\mathbf{v}}, \mathbf{F}_{\text{aero}} \rangle \hat{\mathbf{v}}, \quad (2.3)$$

where $\hat{\mathbf{v}}$ is the normalised velocity field vector and $\langle \hat{\mathbf{v}}, \mathbf{F}_{\text{aero}} \rangle$ is the scalar product of $\hat{\mathbf{v}}$ and \mathbf{F}_{aero} . The lift was estimated as the difference between the total aerodynamic force and drag as:

$$\mathbf{L} = \mathbf{F}_{\text{aero}} - \mathbf{D}. \quad (2.4)$$

An example time-history of the computed aerodynamic forces during a gliding flight phase are reported in Figure 2.7.

2.2. Tools

In the following section the software used for the numerical simulations, the production of the meshes and the estimation of numerical uncertainties are briefly presented.

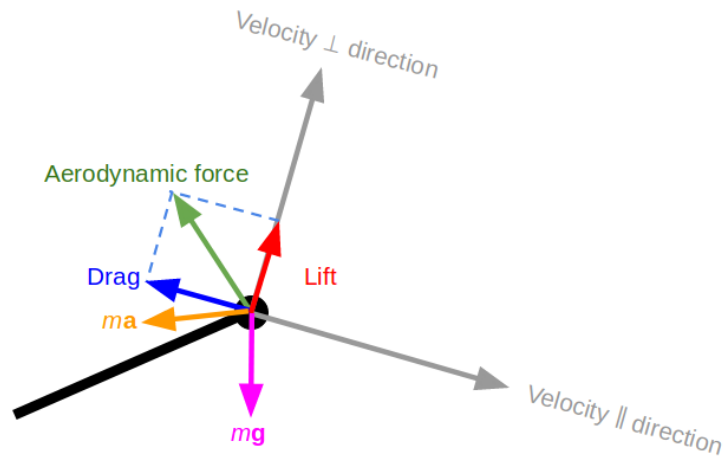


Figure 2.6.: Free body diagram of a gliding butterfly, including vectors normal and parallel to the flight direction, body acceleration vector and vectors of all external force acting on the animal. The animal is depicted as a lolly-pop whereby the circle is the head. Lift and drag can be estimated from the acceleration and weight vectors (Eq. 2.2).

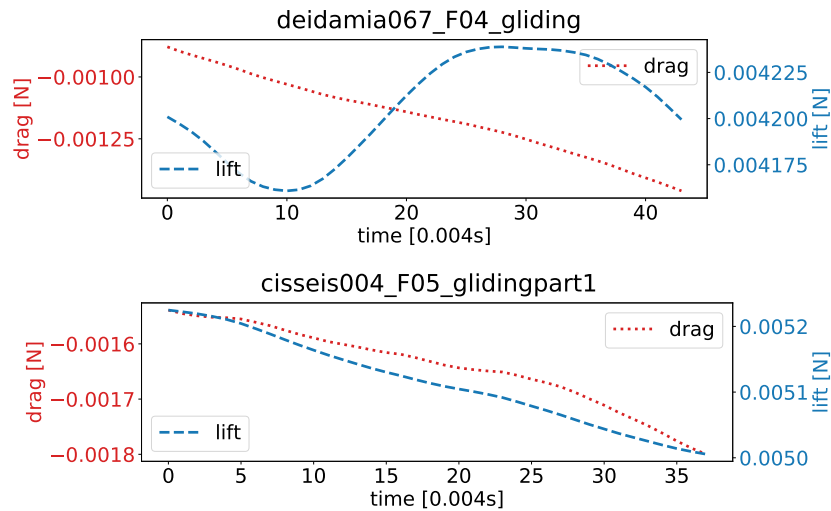


Figure 2.7.: Examples of aerodynamic forces acting on butterflies during a gliding flight phase, computed with the procedure of inverse dynamics presented.

2.2.1. ReFRESKO CFD solver

In the present work all the numerical simulations are performed with the CFD solver ReFRESKO ([28]). This is a viscous-flow CFD code solving multiphase unsteady incompressible flows using the Navier-Stokes equations and turbulence models. The equations are discretized using a finite-volume approach with cell-centered collocated variables. Time integration is performed implicitly with first or second order backward schemes. At each implicit time-step, the non-linear system for velocity and pressure is linearised with Picard's method and either a segregated or coupled approach is used.

ReFRESKO works without GUI; it is launched directly from the terminal or via batch file when ran on a Linux cluster. All the settings of the simulation are gathered in the file `controls.xml`, as shown in Listing 2.1.

Listing 2.1: Example of a `controls.xml` file for Refresco

```
<controls>
<general>
  <codeVersion>2.5</codeVersion>
  <name>morpho</name>
  <description>default description</description>
  <caseid>cisseis</caseid>
  <material>AIR</material>
  <referenceLength>0.07</referenceLength>
  <referenceVelocity>1.5</referenceVelocity>
  <referenceMaterial>AIR</referenceMaterial>
  <referencePressure>0.000000E+00</referencePressure>
  <outFileName>outLam</outFileName>
  <outFilePath>./data</outFilePath>
  <nsave>-1</nsave>
  <suppressOutput>>false</suppressOutput>
</general>
.
.
```

```

<timeLoop>
  <unsteady>>false</unsteady>
  <solutionScheme>IMPLICIT_THREE_TIME_LEVEL</solutionScheme>
  <maxTimesteps>4</maxTimesteps>
  <timeDelta>0.25</timeDelta><!--default 0.0001-->
</timeLoop>

```

2.2.2. HEXPRESSTM mesher

Computational meshes are generated with the software HEXPRESSTM ([38]), an automated mesher developed by NUMECA International which generates non-conformal body-fitted full hexahedral unstructured meshes. The generation of a mesh using HEXPRESSTM goes through the following steps:

1. import of the geometry: a `geometry.stl` file is imported;
2. creation of the domain: a domain is defined around the `geometry.stl` file; in this step names to the surfaces are given and multiple surface can be gathered in one;
3. generation of initial mesh: a first coarse Cartesian grid is created, based on a given number of cells in each direction (see Table 2.1 values "n° cells");
4. adaptation to geometry: specific options of refinements and refinement diffusion are given for any desired surface; box refinements can be created;
5. snapping to geometry: the rough cells are adapted to the shape of the geometry;
6. optimisation: grid optimisation step; usually ran with default settings;
7. inserting of viscous layers: the settings for the insertion of the viscous layers are defined; on each surface, the number of layers or the height of the first cell needs to be defined.

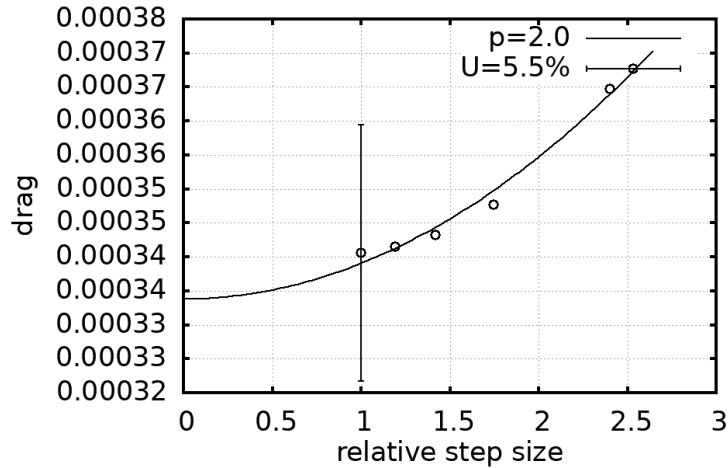


Figure 2.8.: An example of the estimation of the uncertainty due to spatial discretisation for a gliding model of a *Morpho deidamia* at angle of attack 4° . On the x axis the refinement level of the grid (smaller = finer) and on the y axis the relative values for drag.

2.2.3. MARIN internal software for numerical uncertainty estimation

As previously discussed in Section 1.3, any numerical simulation, to be reliable, has to come with an estimation of the uncertainties brought by the numerical discretisation. In this work, to evaluate the uncertainties due to spatial discretisation we use a MARIN internal software, based on the theory presented in [12, 11]. We will use it to check the trend of drag and lift forces with grid refinements. The software, given for each mesh the values of a flow quantity and the typical cell sizes h_i , will minimise Equations 1.53 to 1.60 and will output an uncertainty estimation and the observed order of convergence (respectively the "U" and "p" values visible in Figure 2.8).

2.3. Methodology

2.3.1. Generation of the grids and procedure for refinements

In this work the grids have been generated following this approach:

1. generation of a coarse grid which is already capable of catching the geometry of the wing with sufficient precision to run simulations with low residuals and acceptable results;

2. starting from the previous coarse grid, finer grids are generated to accomplish a grid sensitivity study, for which at least four grids are used; when the computational costs allowed it, five grids have been used.

To follow the first step of this process we found the following settings (referred to the tweakable options in HEXPRESSTM, as reported in Subsection 2.2.2) to be satisfactory:

- the domain is grossly divided in cubic cells with edges 16.7 cm long (referring to the values in Table 2.1, this means that a 1 m x 1 m x 1 m cube is divided with n° Cells X = n° Cells Y = n° Cells Z = 6);
- on the dorsal and ventral sides of the wing 8 refinements are requested, whereas on the edge of the wing 10 refinements are requested, to deal with the sharper curvatures (see Figure 2.9);
- a number of viscous layers is inserted to ensure y^+ values always lower than 1; in this range ($y^+ < 1$), different number of layers have been used, depending on the study case.

In HEXPRESSTM, every refinement consists in halving each cell's edge, thus passing from one to four cells with one refinements, to sixteen with two refinements, and so on. This means that the number of cells increases as 2^{3n} and the size of their edges decreases as 2^{-n} , where n is the number of refinements. Thereby, if our domain is made up of boxes with 16.7 cm long edges, after the refinements we obtain the following typical sizes for the cells close to the wing:

- wing surface, 8 refinements: typical cell edge size of 0,65 mm;
- wing edge, 10 refinements: typical cell edge size of 0,16 mm.

The thickness of the wings is 1 mm, and the edges are modelled as a 0.5 mm radius semi-circumference (see Figure 2.1); the latter is then about 1.57 mm long, which means that with the previous settings for the refinements of the cells we are wrapping around the edges of the wing with at least ten cells; an example of this is shown in Figure 2.9.

Once the first grid is created, we pass to the step of creating finer grids to perform the mentioned uncertainty estimation. As stated in Section 1.3 and in [12, 11], one of

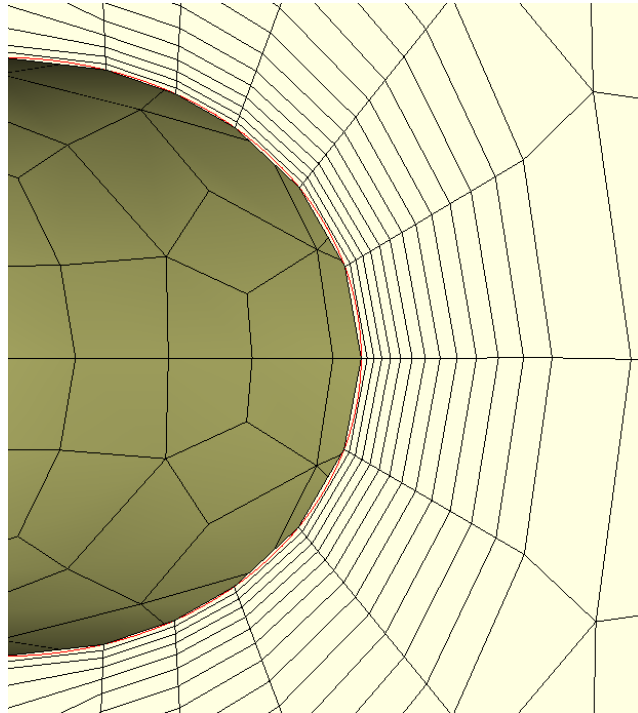


Figure 2.9.: Particular of the coarsest mesh used wrapping around the leading edge of the wing. Note that twelve cells are used to cover the perimeter of the edge. The section is taken at the symmetry plane.

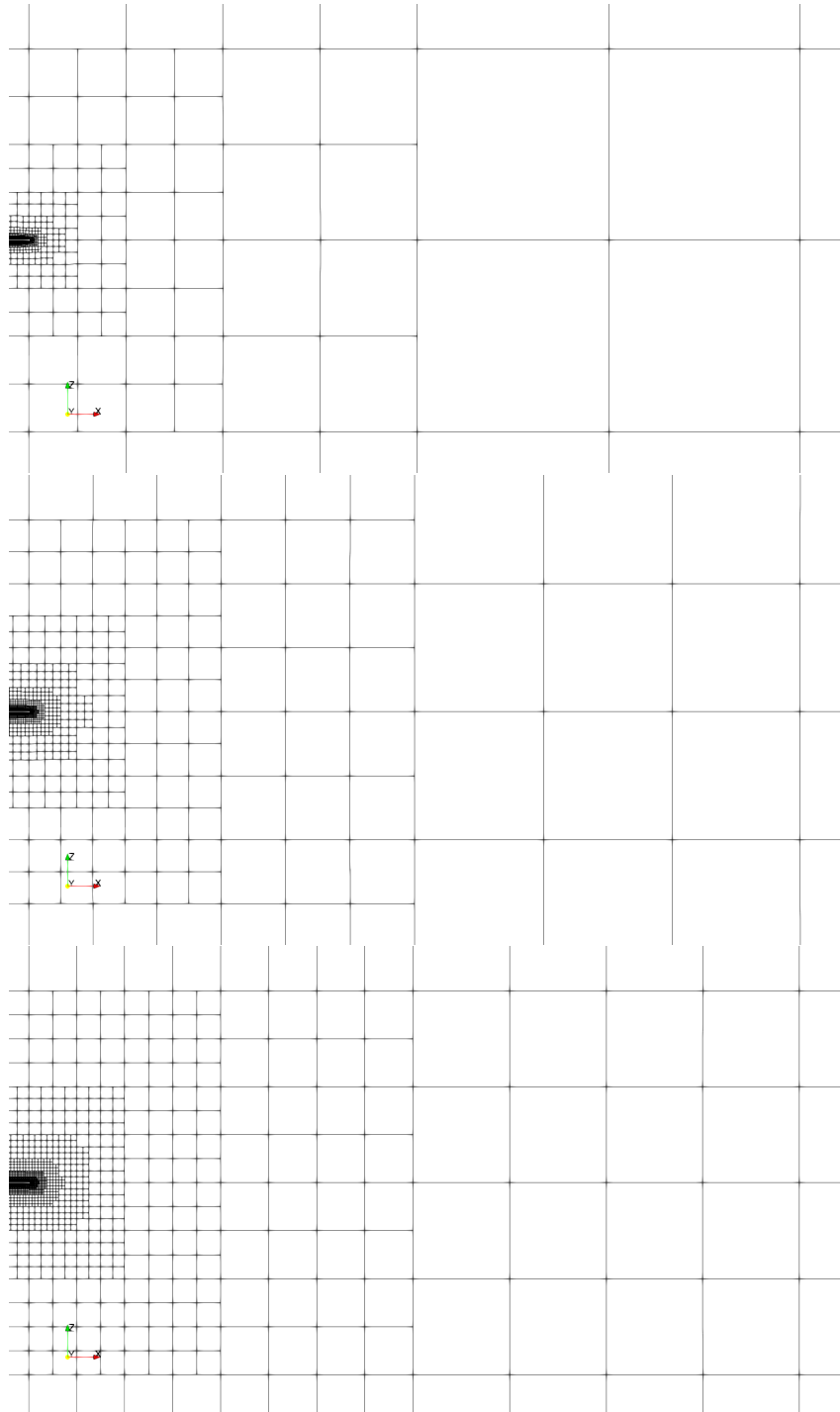


Figure 2.10.: Three meshes of the same geometry (a 0 angle of attack *Morpho cisseis* wing), produced to preserve as much as possible geometrical similarity. The section is taken at the symmetry plane.

meshing parameters	grid series					
	1	2	3	4	5	6
refinement level	1	2	3	4	5	6
n° cells X	12.0	18.0	24.0	30.0	36.0	42.0
n° cells Y	6.0	9.0	12.0	15.0	18.0	21.0
n° cells Z	12.0	18.0	24.0	30.0	36.0	42.0
diffusion	1	2	3	4	5	6
1 st layer thickness	5.00E-05	3.23E-05	2.38E-05	1.89E-05	1.56E-05	1.33E-05

Table 2.1.: Example of HEXPRESSTM parameters used to produce a series of grids (as much as possible) geometrically similar. n° cells represents the number of initial gross cells in the domain along each spatial dimension.

the constraints necessary for a proper study of the inference of spatial discretization in the solution is represented by the use of structured grid -for which a scaling preserving similarity is possible. Although the grids used here are unstructured, they have been generated following the procedure developed in [5], which leads to the production of close to geometrically similar meshes using HEXPRESSTM. An example of the parameters used to produce such series of grids is given in Table 2.1 and the results are visible in Figure 2.10.

2.3.2. Rotation of the grids

With the aim of running simulations with different angles of attack, the following aspects have to be considered:

- the production of a mesh from scratch goes through the use of RhinoTM ([42]), McMesh and HEXPRESSTM;
- meshing two geometries of the same wing at different angle of attack would result in important discrepancies between the grids, which would translate into an added uncertainty when it comes to compare the results.

To overcome this limitations we found a solution to optimise the work and the time needed for the large amount of meshes used. It consists in the following steps:

1. for each butterfly specie (*i.e.* wing shape) only two geometries are generated, one as described in Subsection 2.1.2, with a 0° angle of attack and one as

described in 2.1.3, with a 45° angle of attack;

2. for each of the two geometries the necessary grids are generated (various refinement levels, different y^+);
3. the grid deformation option of ReFRESKO is used to generate grids with different angles of attack starting from the ones built in the previous step.

The advantages brought by this approach are considerable: the use of RhinoTM, McMesh and HEXPRESSTM is minimised and the grids with the wing at various angles of attack share the same pattern, drastically reducing the uncertainties discussed before. Moreover, the rotation of the grid is easily embedded in the simulation with a `bash` script. For example, with the aim of simulating the gliding flight of a butterfly at ten different angles of attack, using five differently refined meshes per angle of attack, twenty-five grids are needed. With this solution only five grids have to be generated, whereas the others will be obtained by deformation.

The deformation of the grid in ReFRESKO is based on radial basis interpolation functions ([8, 55, 54]); the method has been used with default settings and a `<supportRadius>` value of one, which guarantees a deformation of the mesh far enough from the wing, in order to reduce the added skewness in the region of main importance (see Figure 2.11). The deformations are performed in 200 timesteps; this solution proved to preserve the mesh quality almost, if not totally, unmodified.

Listing 2.2: Options for the grid deformation in ReFRESKO. Of particular interest for us the parameter `supportRadius` which expresses the action area where the cells are deformed; as shown in Figure 2.11 with this configuration the mesh pattern surrounding the wing is not warped.

```
<deformGridSetup name="general">
  <general>
    <deformGridApply>true</deformGridApply>
    <deformGridGlobal>true</deformGridGlobal>
    <deformGridUserDefined>false</deformGridUserDefined>
    <exactWallDistanceInOuterLoop>false</exactWallDistanceInOuterLoop>
    <exactWallDistanceFrequencyInTimeLoop>1</exactWallDistanceFrequencyInTimeLoop>
    <updateFrequency>1</updateFrequency>
  </general>
</deformGridSetup>
```

```

    </general>
  </deformGridSetup>
  <deformGridSetup name="deformMethod_RBF">
    <deformMethod_RBF>
      <supportRadius>1</supportRadius>
      <maxiter>500</maxiter>
      <convergenceTolerance>0.100000E-03</convergenceTolerance>
      <greedyApply>true</greedyApply>
      <reuseGreedyDataInOuterLoop>true</reuseGreedyDataInOuterLoop>
      <resetGreedyFrequencyInTimeLoop>100</resetGreedyFrequencyInTimeLoop>
      <exactNearWallCorrFrequencyInTimeLoop>100</exactNearWallCorrFrequencyInTimeLoop>
      <greedyTolerance>0.100000E-01</greedyTolerance>
      <absoluteGreedyTolerance>0.100000E-11</absoluteGreedyTolerance>
      <maxCPUhourToAbort>0.500000E+00</maxCPUhourToAbort>
      <updateStep>20</updateStep>
      <exactNearWallCorrInOuterLoop>false</exactNearWallCorrInOuterLoop>
      <solver>GMRES</solver>
      <preconditioner>SUPERLU</preconditioner>
      <coordinatesystem>
        <CARTESIAN>
        </CARTESIAN>
      </coordinatesystem>
    </deformMethod_RBF>
  </deformGridSetup>

```

2.3.3. On the importance of grid refinements in the wake and of the values of y^+

A topic widely discussed in literature is represented by the importance of grid refinements in the wake. This particular attention to the mesh in the area following the body comes largely from the following reasons:

- the flow details developing downwind the object can have an important role in determining the pressure field close to the body, and, consequently, the forces

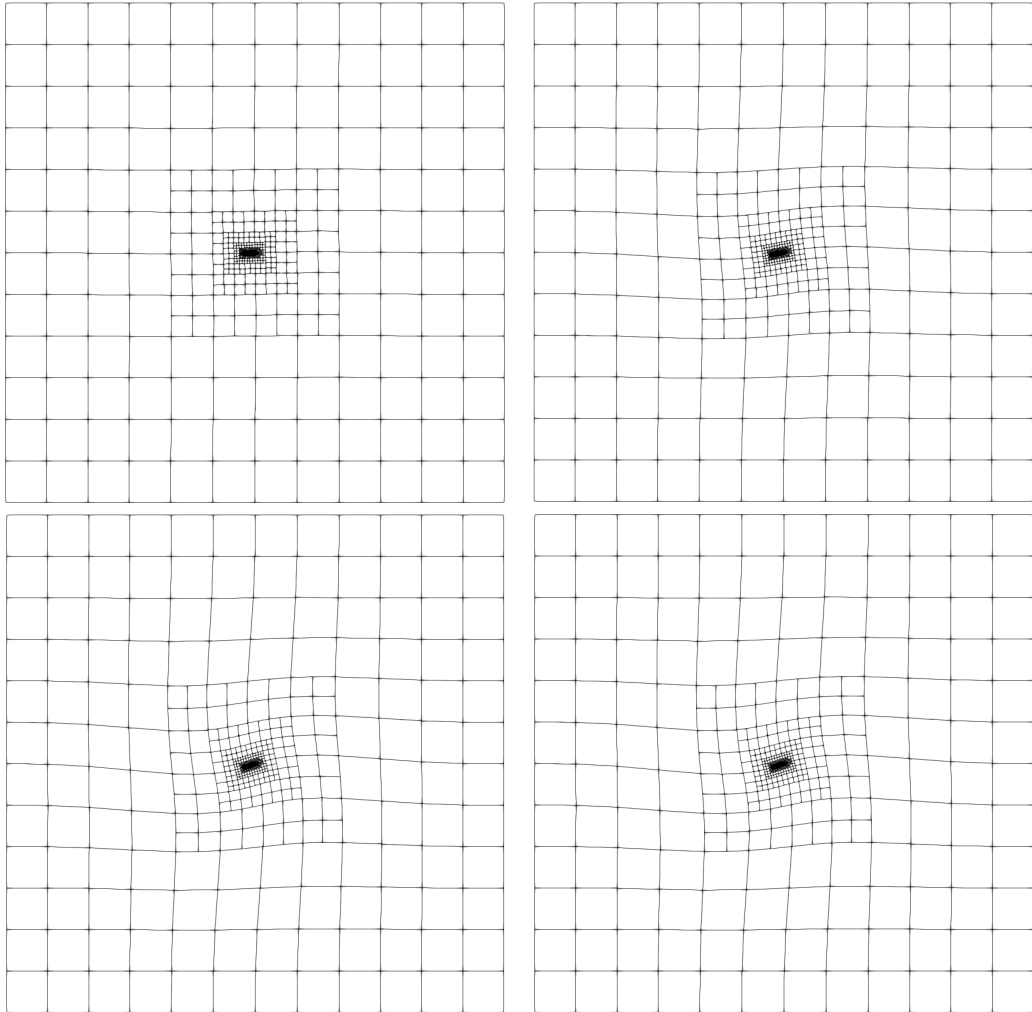


Figure 2.11.: An initial grid is deformed with rotations of 2, 6, 12 and 18 degrees, with the procedure proposed in Subsection 2.3.2. Note that the mesh pattern close to the wing is almost not modified. The section is taken at the symmetry plane.

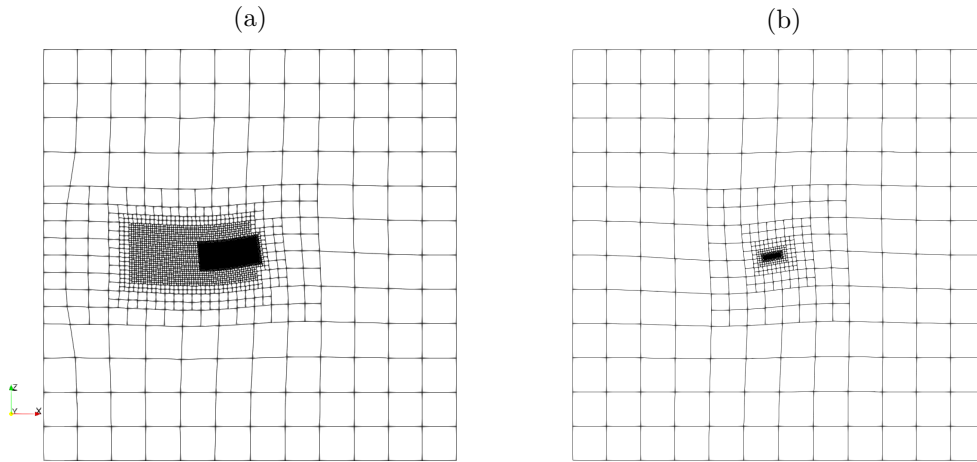


Figure 2.12.: Plane section of the setups **GridF** (a) and **GridC** (b), defined in Subsection 2.3.3 and used for the sensitivity study about y^+ values and box refinements.

acting on it;

- the topology of the wake generated can represent an important parameter when it comes to designing particular structures, for example in civil engineering ([4, 1]), for which a full comprehension of the phenomena taking place downwind is important not only for the facility itself but also for the surrounding buildings and people.

Fortunately, since the wake generated by a butterfly represents a harmless flow pattern for the environment and our purpose lies mostly in gaining insights in the forces acting on the insect, only the first of the two previous points represents a concern to us.

Another parameter of great importance when it comes to CFD simulations stems from the values of y^+ characterising the grid. If the flow is directly solved to the wall -which is our case- and not by means of wall functions, a rule of thumb commonly used establishes that the value of y^+ should always be lower than 1. Nevertheless, in [11] it is showed that for the SST $k - \omega$ turbulence model -largely used in the present work- the inference of y^+ on the results can be considerable also for values below 1 and that a more reliable range of value for y^+ would then be close to 0.1.

For these reasons we studied the effects of these two aspects for our study case. Using the SST $k - \omega$ turbulence model, we performed simulations of a gliding *Morpho*

grid	GridF			GridC			% difference	
	y^+	drag [N]	lift [N]	y^+	drag [N]	lift [N]	drag [N]	lift [N]
1	0.170303E+00	9.19E-04	3.66E-03	0.522060E+00	9.72E-04	3.98E-03	-5.76E+00	-8.84E+00
2	0.128609E+00	8.89E-04	3.61E-03	0.417619E+00	9.20E-04	3.77E-03	-3.42E+00	-4.42E+00
3	0.991440E-01	8.85E-04	3.59E-03	0.352364E+00	8.97E-04	3.65E-03	-1.38E+00	-1.82E+00
4	0.744550E-01	8.85E-04	3.57E-03	0.307924E+00	8.91E-04	3.60E-03	-6.97E-01	-8.12E-01

Table 2.2.: Comparison of aerodynamic forces for two simulations of the same *Morpho cisseis* wing in gliding flight condition with 10.91° angle of attack and inflow velocity of 1.61 m/s. Grid numeration: 1=coarsest, 4=finest.

cisseis with an angle of attack of 10.91 degrees and inflow velocity of 1.61 m/s with two different series of grids:

- the first with box refinements in the wake (see Figure 2.12) and y^+ values close to or lower than 0.1, which will be labelled **GridF**;
- the second without box refinements and a y^+ value lower than 1, which will be labelled **GridC**.

The values of drag and lift for the mentioned simulations are gathered in Table 2.2, showing the percentage difference of the results from **GridC** setups with respect to the ones from the **GridF** setups. Two things about them are worth mentioning:

1. for the finest grids, the difference in the results between the two setups is lower than 1%, allowing us to consider setup **GridC** a good compromise for our simulations;
2. the discrepancy between the two setups gets smaller as the grids are refined, further strengthening the reliability of setup **GridC**.

In the light of this results, some of the simulations have been run with grid settings similar to **GridC** without loss of validity.

2.3.4. On the size of the domain

A fundamental aspect in CFD numerical simulations lies in the sizing of the domain, since we want to be sure that its boundaries are far enough not to pollute the results. For this reason, we compared the solutions for a gliding *deidamia* at 6° and 14°

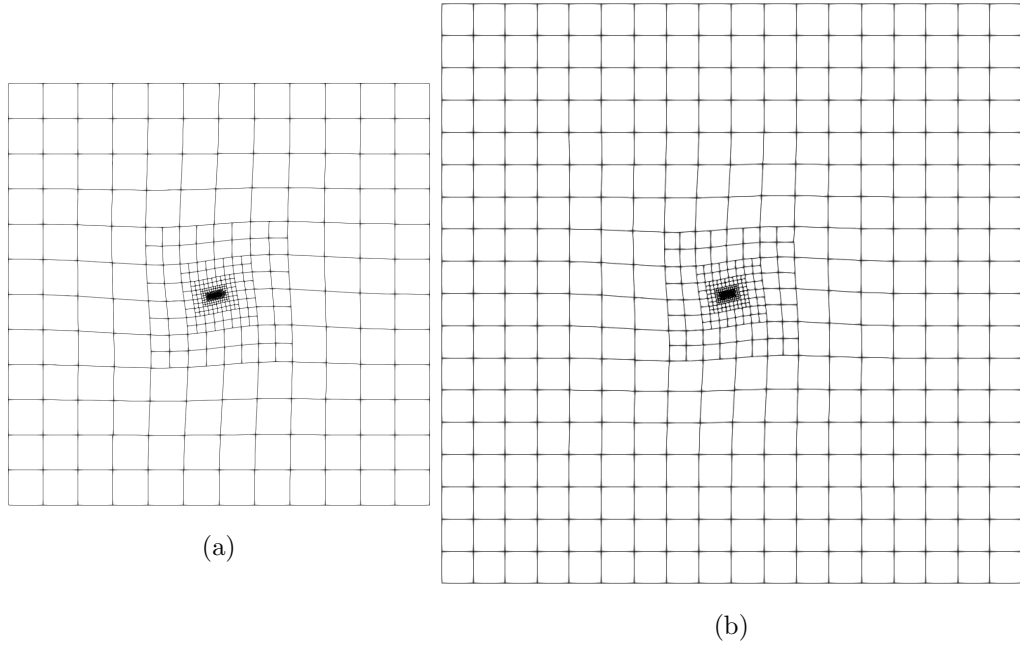


Figure 2.13.: Different domain sizes for a *Morpho deidamia* gliding with a 14° angle of attack; in (a) the original mesh (DomainS) and in (b) the augmented one (DomainB). Slice taken at the symmetry plane.

angles of attack using two domains with different size: one with the size used for the other simulations (2 m x 1 m x 2 m, labelled `DomainS` in this subsection) and one augmented of a 1.5 factor (3 m x 1.5 m x 3 m, labelled `DomainB` in this subsection), as visible in Figure 2.13. The meshing settings used are the same, to maintain the grids exactly the same in the area of the wing.

The values of drag and lift force for the two different domains are compared in Table 2.3, showing that the difference between the quantities in the two domains are negligible.

2.3.5. On the time and space discretisation for flapping simulations

The simulations proposed in Subsection 2.1.3 are unsteady by definition. For this reason, a numerical uncertainty estimation should be accomplished with respect to both space and time discretisations. In practical terms, this means that any study case would need at least 12 simulations with various timesteps and grids with different refinements. Since our goal was to run such simulations at different angles of attack and for different species we estimated that at least 30 different cases would have been required, making such analysis unaffordable in terms of computational

Table 2.3.: Study on the effects of domain size on simulation results. Grid numeration: 1=coarsest, 4=finest.

(a)

grid	DomainB		DomainS		% difference	
	drag	lift	drag	lift	drag	lift
1	4.3860E-04	2.1451E-03	4.3755E-04	2.1441E-03	2.3892E-01	4.5825E-02
2	4.2028E-04	2.1448E-03	4.1971E-04	2.1411E-03	1.3574E-01	1.6832E-01
3	4.1545E-04	2.1425E-03	4.1514E-04	2.1407E-03	7.5989E-02	8.6253E-02
4	4.1557E-04	2.1489E-03	4.1541E-04	2.1478E-03	3.8982E-02	4.9933E-02
5	4.1408E-04	2.1454E-03	4.1396E-04	2.1443E-03	3.0598E-02	5.1738E-02

(b)

grid	DomainB		DomainS		% difference	
	drag	lift	drag	lift	drag	lift
1	1.2093E-03	4.0330E-03	1.1962E-03	3.9802E-03	1.0813E+00	1.3089E+00
2	1.1177E-03	3.6769E-03	1.1026E-03	3.6154E-03	1.3457E+00	1.6738E+00
3	1.0757E-03	3.4981E-03	1.0765E-03	3.4982E-03	-7.5859E-02	-3.0874E-03
4	1.0724E-03	3.4588E-03	1.0734E-03	3.4622E-03	-9.8567E-02	-1.0027E-01
5	1.0651E-03	3.4146E-03	1.0638E-03	3.4081E-03	1.2055E-01	1.8957E-01

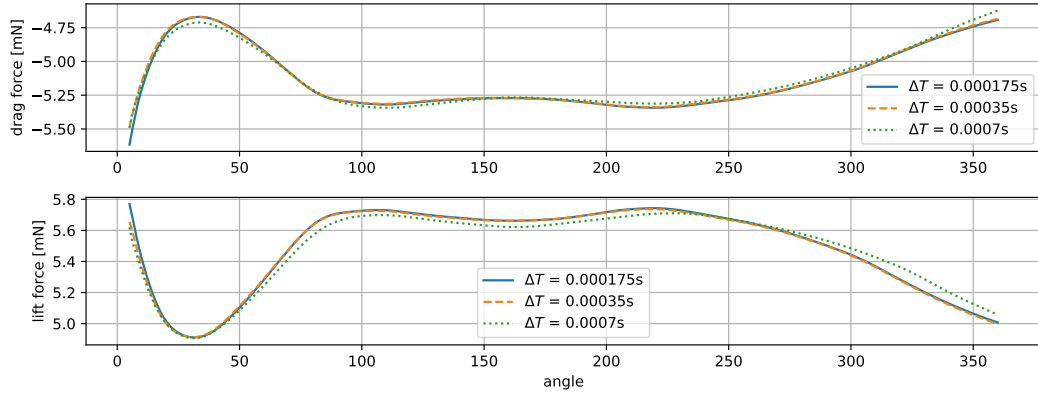


Figure 2.14.: The time history of drag and lift forces during the rotation of the wing in a flapping setup (2.1.3) at 45° angle of attack with three different timesteps.

costs. For this reason we decided to perform a sensitivity study on the spatial and time discretisation only for the 45° angle of attack case, which lies in the middle of our range values of angles of attack for the flapping simulations. To accomplish this, we started from the setting we found to be computationally-speaking affordable and we ran simulations with refinements in time or in space to understand how reliable such setup is. Being our target timestep $\Delta T_0 = 6.66667\text{E-}04$ s and calling our target grid Grid_0 , for the sensitivity to time discretisation we performed simulations with $\Delta T = 7.0\text{E-}4, 3.5\text{E-}4, 1.75\text{E-}4$ using Grid_0 and for the sensitivity to space discretisation we ran computations using $\text{Grid}_0, \text{Grid}_1$ and Grid_2 (where the subscript refers to the refinement level: 0=coarsest, 2=finest) with $\Delta T = 7.0\text{E-}4$.

The time history of drag and lift forces during the rotation of the wing for the three different timesteps is reported in Figure 2.14 and for the three refinement levels in Figure 2.15. To offer a more exhaustive idea of the discrepancies in the results brought by the discretisation refinements, the L_2 and L_∞ norms of the drag and lift differences between the various simulations (the integration is computed over all the timesteps) are reported in Table 2.5: there, with $L_2 \text{ Diff}_{01}$ we mean the L_2 norm of the difference of a quantity between the refinement (either in time or space) "0" (coarsest option) and the refinement "1". The results of Figure 2.14 and 2.15 and of Table 2.5 show that the target timestep and grid represent a good compromise, providing result with mild sensitivity to discretisation refinements at an affordable computational cost.

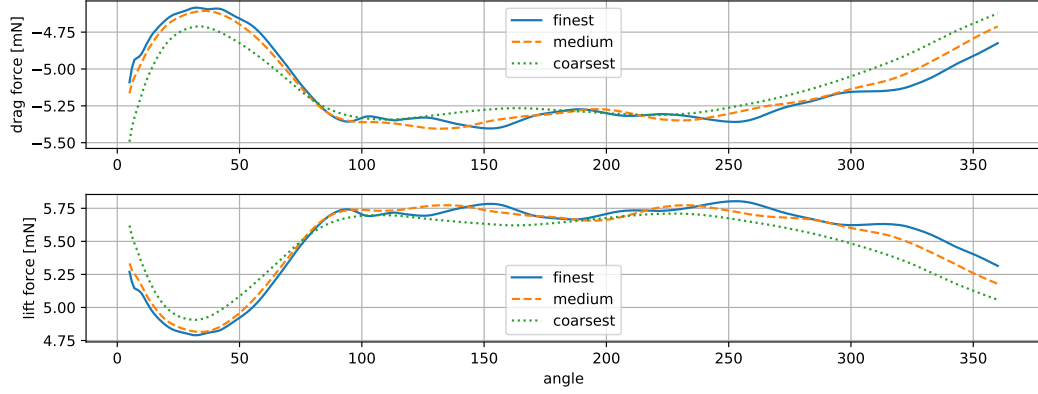


Figure 2.15.: The time history of drag and lift forces during the rotation of the wing in a flapping setup (2.1.3) at 45° angle of attack with three different refinement grids produced following Subsection 2.3.1.

variable	timestep sensitivity		grid sensitivity	
	drag force [N]	lift force [N]	drag force [N]	lift force [N]
$\ \text{Diff}_{01}\ _{L^2}$	4.69520E-04	7.85363E-04	1.633138E-03	1.823789E-03
$\ \text{Diff}_{12}\ _{L^2}$	2.67041E-04	2.40808E-04	9.78006E-04	1.128108E-03
$\ \text{Diff}_{01}\ _{L^\infty}$	4.69520E-04	8.7358E-05	1.633138E-03	2.86365E-04
$\ \text{Diff}_{12}\ _{L^\infty}$	1.32615E-04	1.14282E-04	1.20409E-04	1.45169E-04

Table 2.5.: Norms of the drag and lift differences between different levels of refinement in either time or space. Diff_{01} stands for the the difference between the "level 0" refinement (coarsest option) and the "level 1".

3. Reproduction of a Morpho Butterfly's Gliding Flight Using Various Turbulence Models and Comparison with Experimental Data

Does the flap of a butterfly's wings
in Brazil set off a tornado in Texas?

E. N. Lorentz

3.1. Setup and Considerations

In this chapter we approach the study of *Morphos*' gliding flight using different CFD models and we compare them with the experimental results provided by [22] and postprocessed as described in Subsection 2.1.4. Here we aim at understanding how close the predictions of the models used are to the experimental counterpart. Moreover, we want to compare the different models to understand if consistent differences arise between them. The numerical simulations try to reproduce the gliding flight performed by specimen `cisseis004_F05_glidingpart1` ([22]); the relative kinematic data and aerodynamic forces deduced with inverse dynamics approach are plotted in Figure 3.1 and Figure 3.2 and the average values of them are used for the simulations (see Table 3.1). With respect to mean wing chord, the flight is characterised by a Reynolds number of 5200. The setup is the one described in Subsection 2.1.2. In this chapter we use four grids with different refinements, generated and rotated as described in Section 2.3; a side view of the coarsest is shown in Figure 2.12 (a) and the total number of cells of each grid is given in Table 3.2.

The choice of this specimen is a consequence of the smooth development in time

Numerical setup and physical details	
specie	<i>Morpho cisseis</i>
inflow velocity	1.61 m/s
angle of attack	10.91°
weight	0.58 g
mean wing chord	0.0482 m
hinge-to-tip length	0.085 m

Table 3.1.: Setup values for the numerical simulations discussed in this chapter. The inflow velocity and the angle of attack are the results of averaging the respective time histories during the gliding phase for which the kinematic data are given in Figure 3.1 and the aerodynamic forces computed with inverse dynamics approach in 3.2.

grid characteristics		
grid	n cells	y
1	1,157,340	0.522060E+00
2	3,785,147	0.417619E+00
3	8,406,881	0.352364E+00
4	15,738,960	0.307924E+00

Table 3.2.: Characteristics of the grids used for the simulations discussed in this chapter.

cisseis004_F05_glidingpart1 - kinematic data resume

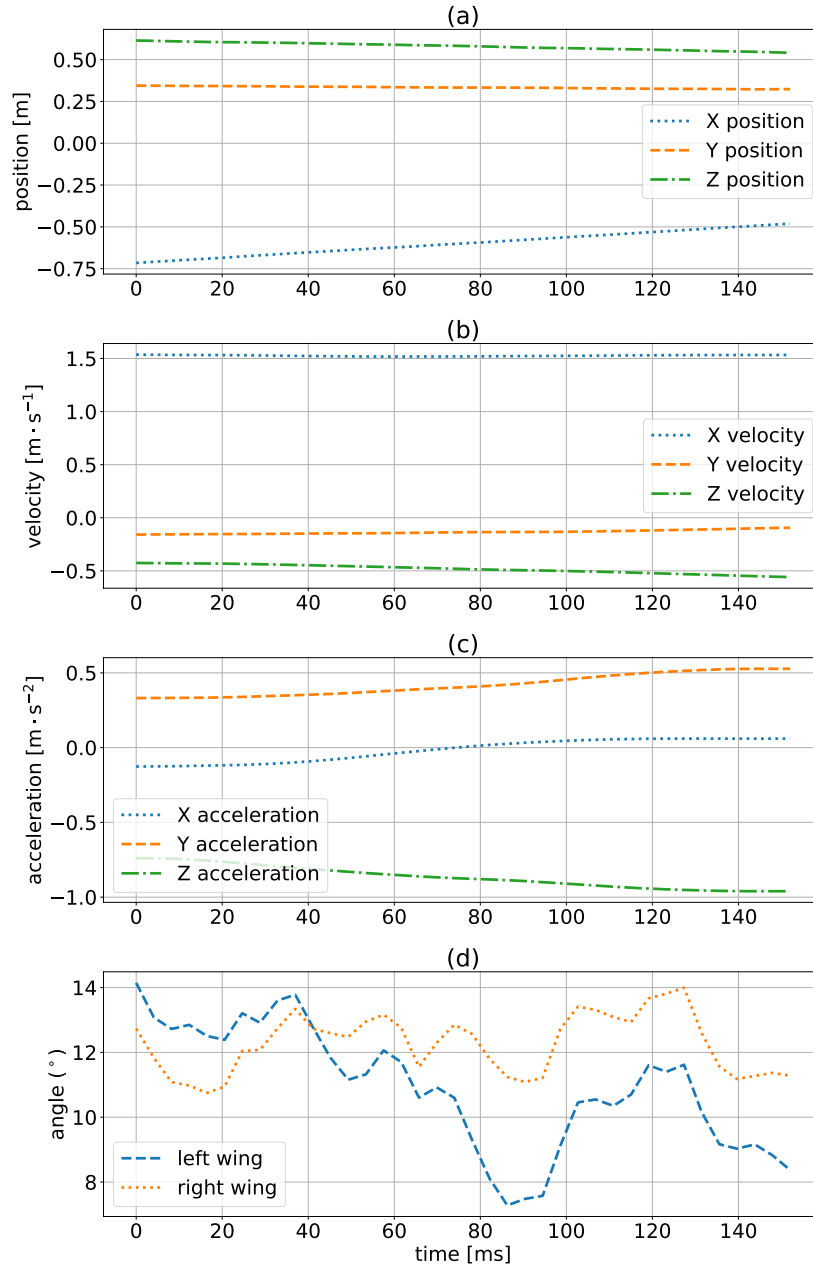


Figure 3.1.: Gliding trajectory of the specimen `cisseis004_F05_glidingpart1`, taken as reference for the validation of the numerical results. In (a) the position field during the flight, in (b) the velocity field, in (c) the acceleration field and in (d) the angles of attack of the wings. These values have been averaged to setup the CFD simulations. Data source: [22].

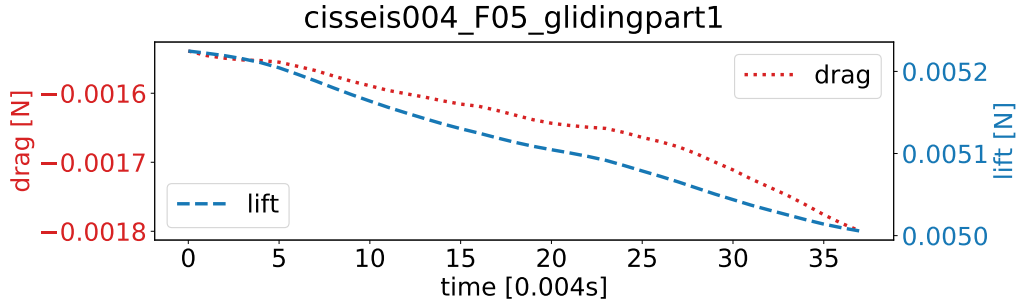


Figure 3.2.: Aerodynamic forces acting on the specimen `cisseis004_F05_glidingpart1` during its gliding phase flight that is reproduced numerically in this chapter, computed with the procedure of inverse dynamics. The time-average values of drag and lift are used for the comparison with the CFD results.

not only of the velocities but also of the aerodynamic forces, suggesting that the glide phase was not affected by significant external events. Five different models have been chosen for the numerical simulations.

- The first model used is the SST $k-\omega$. This model has been developed for aerodynamics applications ([30]) and has provided very reliable results in internal MARIN applications using ReFRESCO.
- The second model chosen is the Spalart-Allmaras ([47]), which was also created for aerodynamic purposes and has been extensively validated.
- Given the low Reynolds number at which these butterflies operate, we considered the possibility that transition could play an important role; for this reason we also performed simulations equipping the SST $k-\omega$ model with the $\gamma-Re_\theta$ equations. Since this model is sensitive to the inflow conditions of eddy viscosity, we used two different setups with inlet conditions of ν_t/ν equal to 10 and 2.5, following some experiments performed in [21].
- As an alternative to the listed fully modelled approaches, we investigated the study case using PANS, with the aim of solving directly part of the turbulence and check if this could bring more detailed or more precise results.

The details of the options used in the CFD solver are presented in the following subsections.

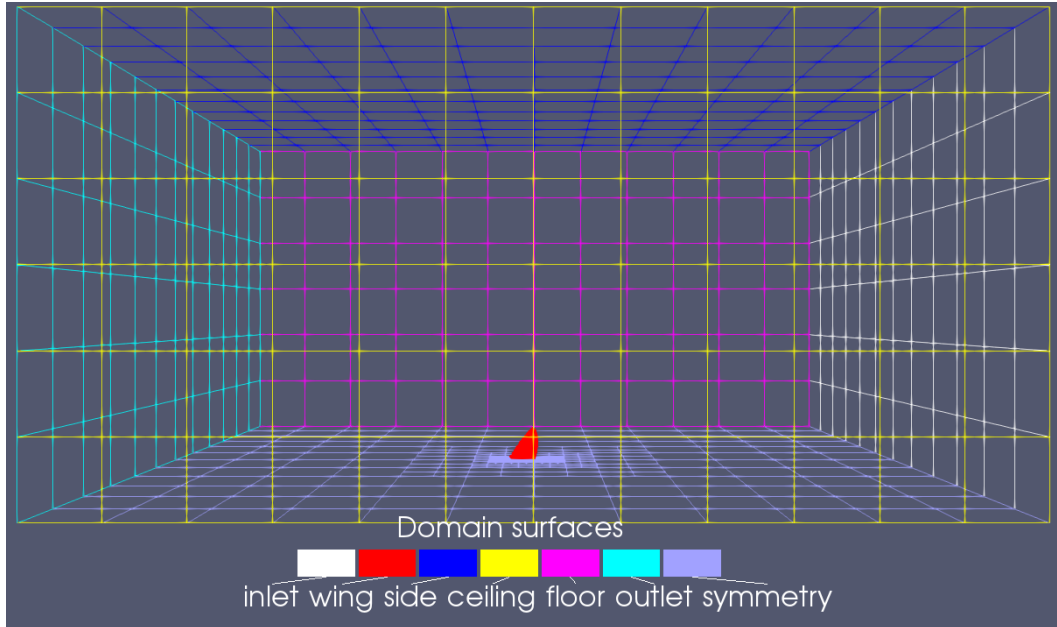


Figure 3.3.: Boundary surfaces of the numerical domain.

3.1.1. Common configurations

Part of the numerical setup used for the different cases is shared by all the simulations. Such configurations are listed below.

- Fluid properties:
 - air density (ρ): 1.225E-00 kg/m³;
 - air dynamic viscosity (μ): 1.81E-05 Pa·s;
- boundary conditions (see Figure 3.3):
 - wing surface: velocity no-slip condition;
 - inlet surface: velocity (-1.61E00, 0, 0)m/s, turbulence intensity 0.01;
 - side: pressure 0 Pa (free stream);
 - ceiling: pressure 0 Pa (free stream);
 - floor: pressure 0 Pa (free stream);
 - outlet: pressure 0 Pa (free stream);
 - symmetry: all unknowns symmetry;
- outerloop:
 - max n^o iterations: 400;

- check residual norm: L^∞ ;
- convergence tolerance: 1E-06;
- convergence check skipped for: $k - \omega$ equations, $\gamma - Re\Theta$ (when present);
- solver type: segregated;
- momentum equations:
 - solver: GMRES;
 - preconditioner: BJACOBI;
 - convergence tolerance: 1E-03;
 - max n° iterations: 1200;
 - min implicit relaxation: 0.50E+00;
 - max implicit relaxation: 0.90E+00;
 - implicit relaxation factor: 1;
 - explicit relaxation: 2.5E-01;
 - convective flux discretisation: total variation diminishing (TVD) harmonic scheme;
 - gradient calculations method: Gauss;
 - apply eccentricity correction: true;
- pressure equation:
 - solver: conjugate gradient method;
 - preconditioner: BJACOBI;
 - convergence tolerance: 1E-03;
 - max n° iterations: 1200;
 - explicit relaxation: 1E-01;
 - gradient calculations method: Gauss;
- transition equations (when present):
 - solver: GMRES;

- preconditioner: BJACOBI;
- convergence tolerance: 1E-03;
- max n° iterations: 200;
- min implicit relaxation: 0.50E+00;
- max implicit relaxation: 0.95E+00;
- implicit relaxation factor: 1;
- explicit relaxation: 2.0E-01;
- convective flux discretisation: first order upwind scheme;
- gradient calculations method: Gauss;
- tolerance apply gamma: 10;
- relaxation gamma: 1.

3.1.2. Configurations for turbulence equations

The Spalart-Allmaras, SST $k-\omega$ and SST $k-\omega$ with $\gamma-Re_\theta$ share the same configuration for the solution of the turbulent equations, whereas for PANS different settings have been used. This choice derives from the difficulties in reaching convergence for the PANS simulations, which, with the same settings used for the other models, were affected by L^∞ norms of residuals never decreasing under values of 1E+00 and L^2 norms of residuals never decreasing under values of 1E-02. As it will be shown later, the changes made for this purpose showed considerable improvements in the residuals trend. For the first three models, the following options have been used:

- turbulence equations (SST $k-\omega$, Spalart-Allmaras):
 - model type: $k-\omega$ SST (Spalart-Allmaras for Spalart-Allmaras simulations);
 - solver: GMRES;
 - preconditioner: BJACOBI;
 - convergence tolerance: 1E-03;
 - max n° iterations: 200;
 - min implicit relaxation: 0.95E+00;

- max implicit relaxation: 0.95E+00;
- implicit relaxation factor: 1;
- explicit relaxation: 2.5E-01;
- convective flux discretisation: first order upwind scheme;
- gradient calculations method: Gauss;
- apply eccentricity correction: true;
- turbulent intensity initialisation: 0.01;
- turbulent viscosity initialisation: 0.01 (2.5 and 10 for SST $k - \omega$ + $\gamma - Re_\theta$ simulations).

For the PANS simulations, the following options have been used:

- turbulence equations (SST $k - \omega$, Spalart-Allmaras):
 - model type: $k - \omega$ SST (Spalart-Allmaras for Spalart-Allmaras simulations);
 - solver: GMRES;
 - preconditioner: BJACOBI;
 - f_k value: 0.2;
 - f_ϵ value: 1;
 - convergence tolerance: 1E-03;
 - max n° iterations: 200;
 - min implicit relaxation: 0.99E+00;
 - max implicit relaxation: 0.99E+00;
 - implicit relaxation factor: 1;
 - explicit relaxation: 1.0E-01;
 - convective flux discretisation: total variation diminishing (TVD) harmonic scheme;
 - gradient calculations method: Gauss;
 - apply eccentricity correction: false;
 - turbulent intensity initialisation: 0.01;
 - turbulent viscosity initialisation: 0.01.

3.1.3. Configurations for the timestep

All the simulations in this chapter are run as unsteady. For the various model a first attempt has been done with the following settings:

- `timeloop`:
 - `unsteady`: true;
 - `solution scheme`: implicit three time level scheme;
 - `time delta`: 0.0008 s.

This value of the timestep was chosen such that the mean flow needs more than fifty timesteps to sweep the whole wing. The Spallart-Allmaras and SST $k - \omega$ model based simulations converged to a steady state, whereas the ones using PANS resulted in an unsteady state. For this reason PANS simulations were run with various refinements in timesteps, in order to estimate their uncertainty not only with respect to the spatial but also to the temporal discretisation. The combinations of grids and timesteps used are reported in Table 3.3, together with the respective Courant Number, which is defined as:

$$C_N = \|\mathbf{u}\|_{L^2} \frac{\Delta t}{\Delta x}, \quad (3.1)$$

Δt being the timestep and Δx the maximum cell size. Since the PANS model is resolving directly part of turbulence, we aim at always having a Courant number lower than 1, since otherwise the spatial resolution of the grid is finer than the temporal resolution, meaning that we are not catching part of the turbulence spectrum that our mesh would allow us to catch. Looking at Table 3.3, one could argue that this condition is never respected in the simulations lead here. This is true in absolute terms, but since the maximum Courant number is not really descriptive of what is happening on the whole domain, in Figure 3.4 we show, for the finest configuration both in space and time, the cells in the whole domain which have a Courant number higher than 1. As it can be seen, these cells are limited to small regions around the edges, where turbulence is either absent or not fully developed; moreover, most of this cells are still characterised by a Courant number below 2, thus we believe the timestep used is adequate, since it is below one in the fluctuating regions of the flow. This aspect is confirmed by the the timestep sensitivity study showed in Figure 3.8.

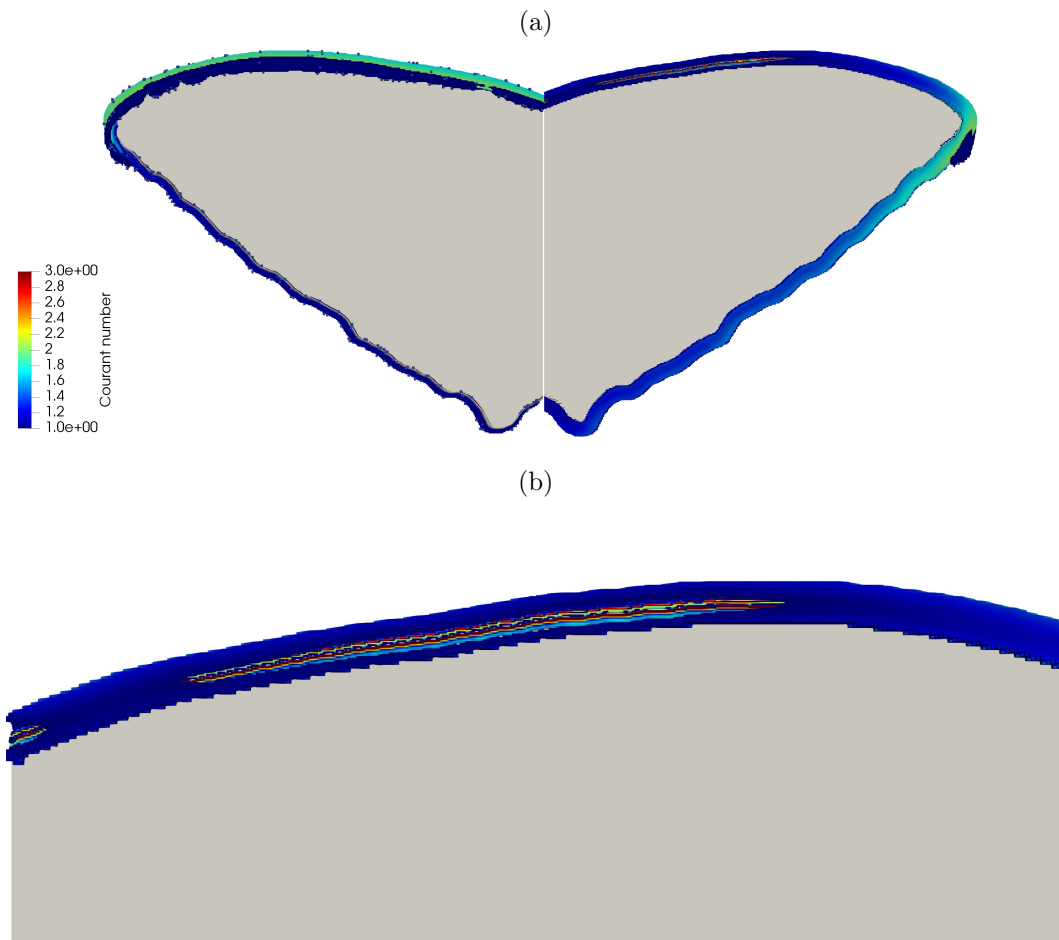


Figure 3.4.: Distribution of cells with Courant number greater than 1 throughout the domain for the PANS simulator with the finest grid and timestep refinement. In (a) the dorsal side (left) and ventral side (right) of the wing and in (b) a zoom on the pressure side leading leading edge, where the cells with the highest values of C_N lie.

PANS simulations: resume of discretisation steps		
n° cells	Δt	max Courant n.
1157340	2.000E-03	0.721E+03
1157340	1.000E-03	0.360E+03
1157340	5.000E-04	0.180E+03
3785147	1.340E-03	0.700E+03
3785147	6.700E-04	0.350E+03
3785147	3.350E-04	0.175E+03
8406881	1.040E-03	0.726E+03
8406881	5.200E-04	0.363E+03
8406881	2.600E-04	0.181E+03
15738960	8.200E-04	0.738E+03
15738960	4.100E-04	0.369E+03
15738960	2.050E-04	0.184E+03
15738960	1.025E-04	0.923E+02

Table 3.3.: Resume of grid sizes and timesteps used for the PANS simulations, together with the respective maximum Courant number.

3.1.4. Configuration of the f_k value

As discussed in Subsection 1.2.9, what defines the amount of turbulence directly resolved in a PANS simulation is the f_k value. At the state of the art, different techniques exist to determine the correct value to use ([15, 16, 19]). Here, we refer to the oldest but also most robust ([19]) of these methods, which consists in choosing a fixed value for f_k and then to run simulations refining both in space and time to reach an asymptotical trend of the results.

3.2. Results

Here we report the plots of various flow quantities of the simulations with the different models and then we compare the relative values of drag and lift with the ones extrapolated from the butterfly's kinematics. If not differently specified, the results refer to the simulations performed with the finest grid (and smallest timestep for PANS). Since the SST $k - \omega$ and Spalart-Allmaras models lead to a steady state, the results at the last timestep represent a fully descriptive dataset. Regarding the PANS model, the plots shown that are not depending on time are the result of a time-averaging of the solutions of various timesteps (here, the finest simulation in both space and time is used).

3.2.1. Residuals

For the simulations run with SST $k - \omega$ and Spalart-Allmaras the trends of the residuals at each timestep are mostly monotonically decreasing, reaching orders of magnitude lower than 10^{-10} . Here, an important remark is needed regarding the iteration error: in Figure 3.5 the L^2 and L^∞ norm residuals of the simulation run with SST $k - \omega$ are plotted together with the time history of drag and lift forces; it can be noticed that the latter two reach a constant value while the residuals keep decreasing. This means that the inference of the iterative error on the results is null or negligible. The other simulations with Spalart-Allmaras and $\gamma - Re_\theta$ have similar trends for the residuals norms, which will not be reported.

For the PANS simulations the trend of the residuals is checked at the iteration level and not at the timestep level, due to their unsteady nature. In 3.6 it can be seen that at each timestep the L^2 and L^∞ norms of residuals decrease of almost four

orders of magnitude.

Residuals at each timestep - SST $k - \omega$ - 3° grid refinement level

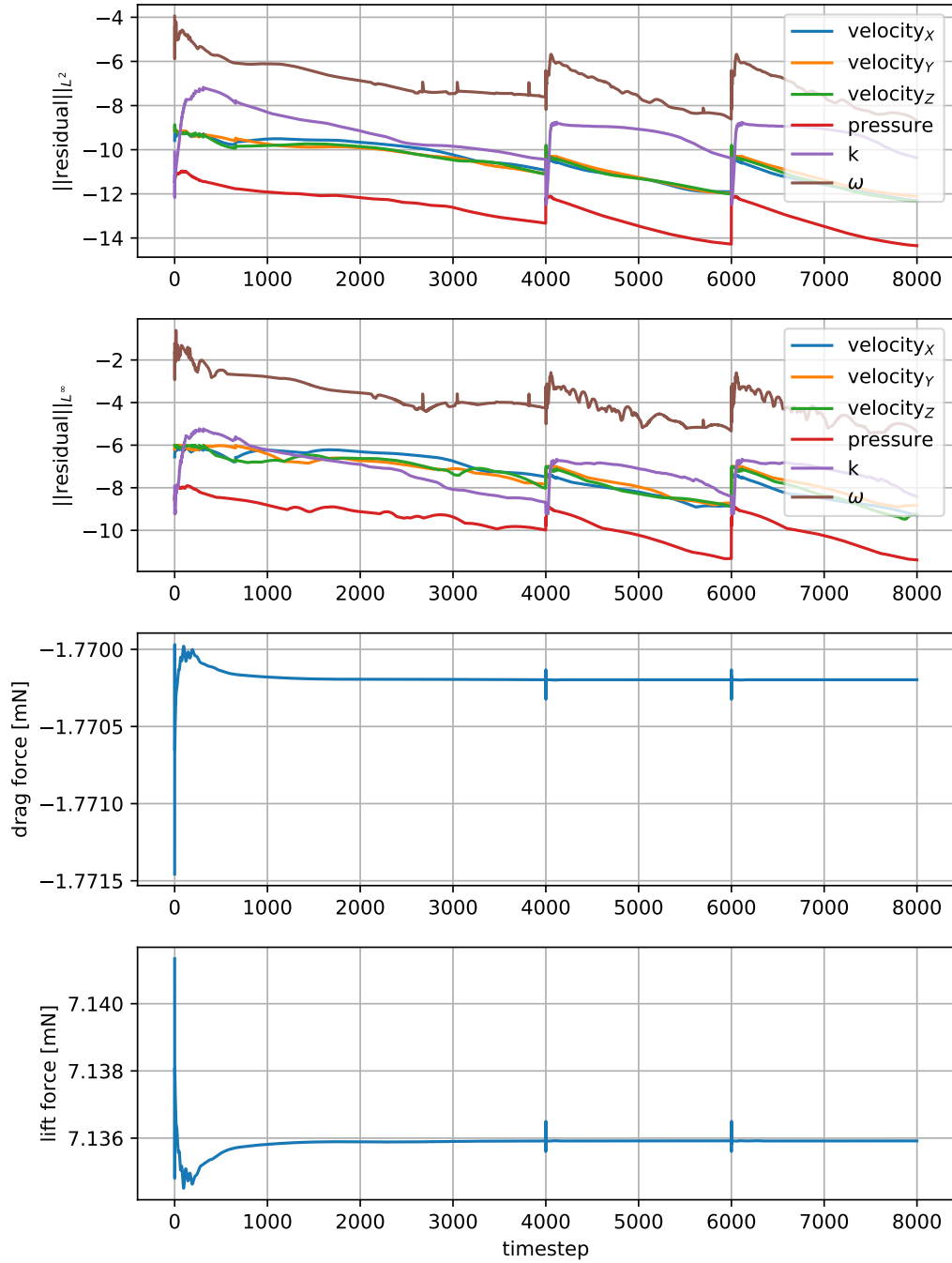


Figure 3.5.: L^2 and L^∞ norm residuals of the simulation run with SST $k - \omega$ on the finest grid, together with the history of lift and drag forces.

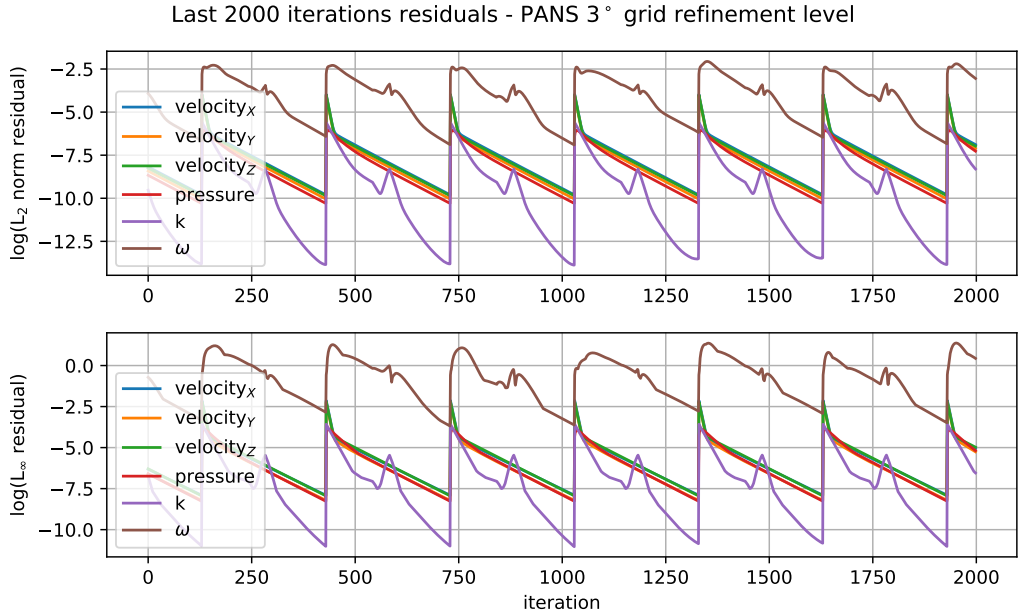


Figure 3.6.: L^2 and L^∞ norm residuals for the last 2000 iterations of a PANS simulation using the finest grid available and the smallest timestep (0.0001025 s).

3.2.2. Numerical uncertainty

In the following pages the numerical results will be often presented with an uncertainty. This has been computed using the internal MARIN software based on [12, 11]. For the Spalart-Allmaras, SST $k - \omega$ and $\gamma - Re_\theta$ simulations, the estimation of the uncertainty is performed with respect to space discretisation only, due to their steady nature. The theory behind this estimation is briefly recalled in Section 1.3, and computes the trend of the integral parameters we are considering (in our case, drag and lift force) against grid refinement; in Figure 3.7 such trend for the drag force using SST $k - \omega$ model is shown. For PANS simulations the uncertainty is estimated for both space and time discretisation, resulting in the prediction of a trend surface instead of a trend line. The theory used for this estimation is not discussed in the present work but can be found in [43, 11, 27]. In Figure 3.8 the drag trend for PANS simulations is shown, underlining that the sensitivity to the timestep is much larger than the sensitivity to the grid. All the uncertainties are here gathered as error bars in Figure 3.33. For sake of shortness, the full plots are however reported in Appendix A.

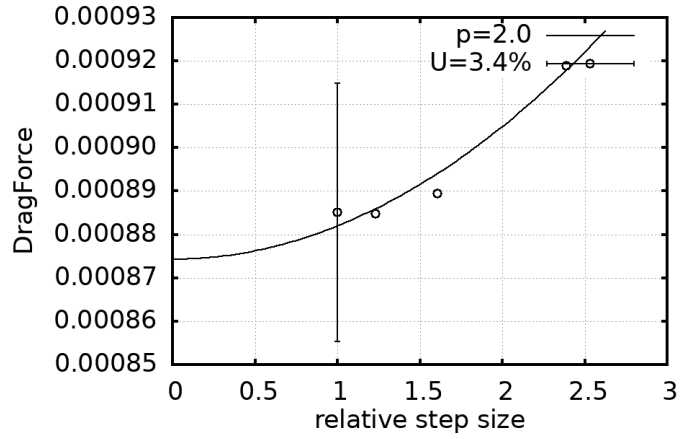


Figure 3.7.: Trend of drag force values with grid refinements and respective numerical uncertainty estimation for the SST $k-\omega$ simulations.

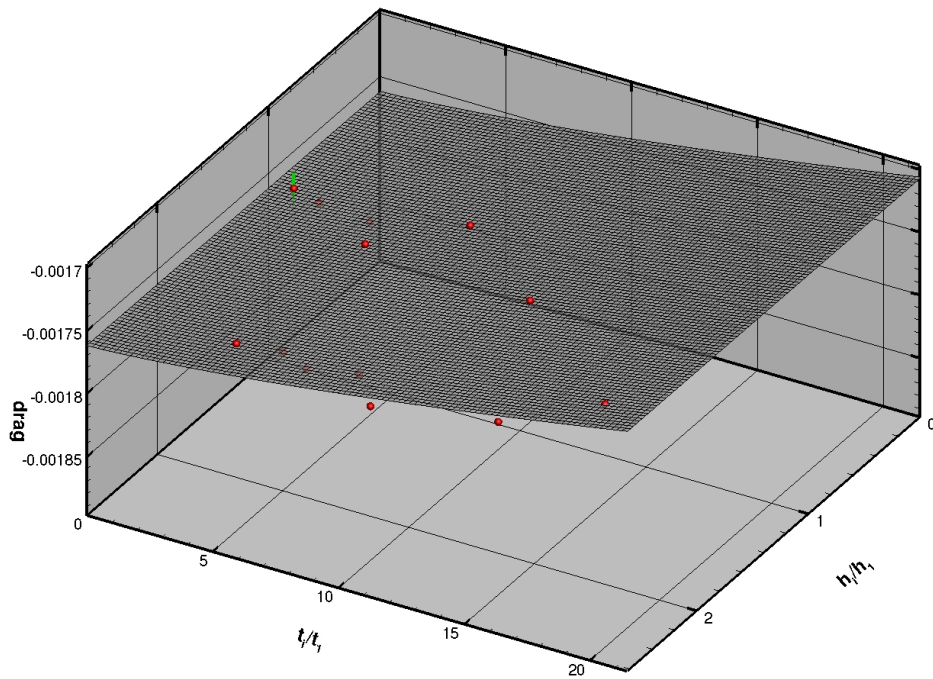


Figure 3.8.: Trend of drag force values with grid refinements and respective numerical uncertainty estimation for the PANS simulations. Here the uncertainty is represented by the green bar, whereas the red dots represent the position of the simulations in the timestep-gridsize-value space.

3.2.3. Velocity field in the stream direction

Figures 3.9, 3.10, 3.11, 3.12 and 3.13 show, for the different models, the field of the dimensionless x -component of the velocity on a slice at 1 cm from the symmetry plane. All the cases highlight the same flow pattern, with separation occurring at the leading edge and a separation bubble sweeping the whole wing chord. The SST $k - \omega$ model shows a wider and more developed bubble than the Spalart-Allmaras and $\gamma - Re_\theta$ with $\nu_t/\nu=10$ inflow, which are instead characterised by a narrow and short bubble; the other $\gamma - Re_\theta$ simulation lies in between the other results. The PANS model predicts the widest and most elongated separation, resulting in a very neat area of reverse flow.

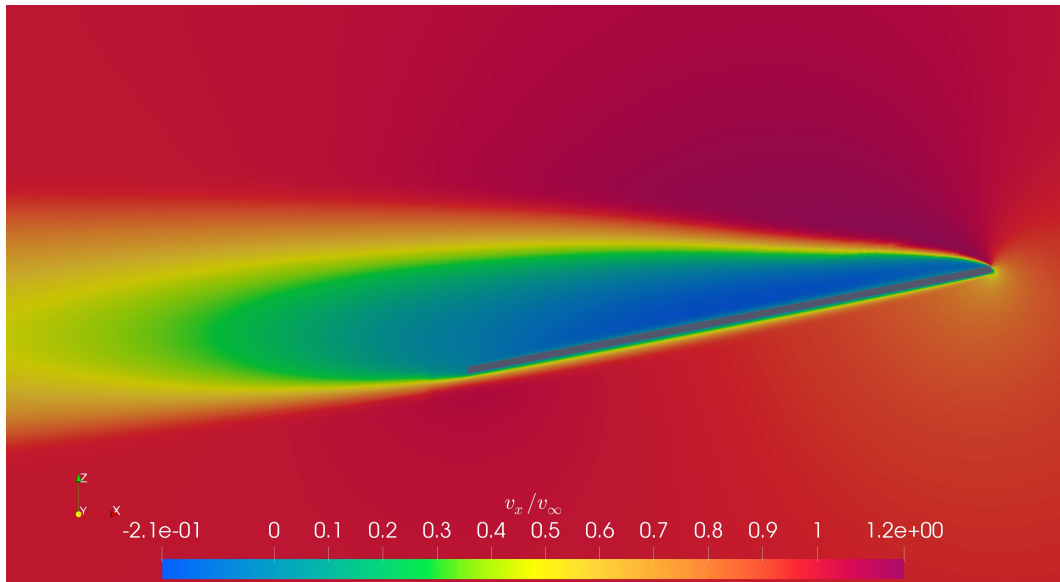


Figure 3.9.: dimensionless velocity (u_x/u_∞) field at $y = 0.01$ m using the SST $k - \omega$ model.

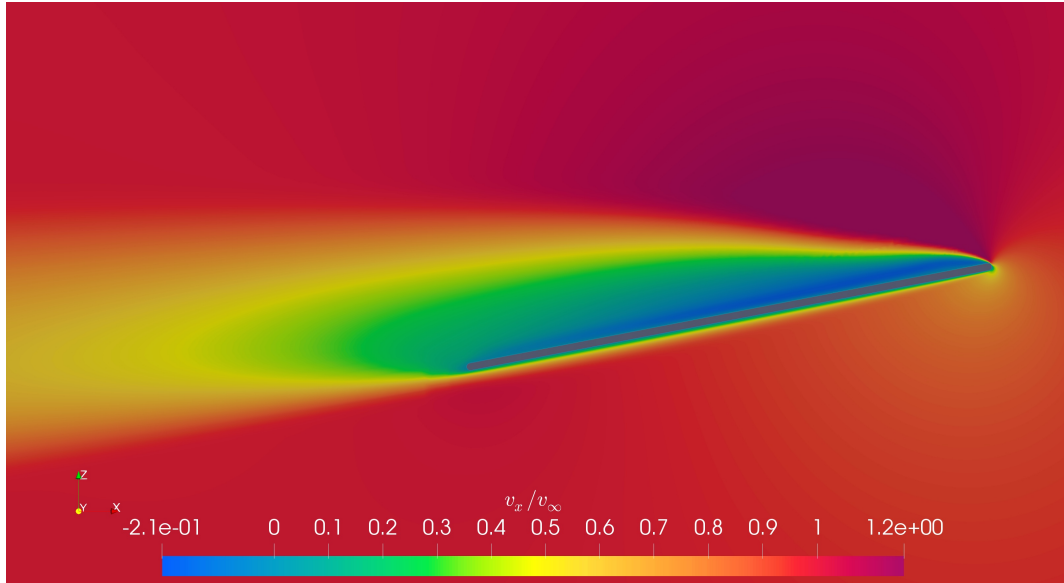


Figure 3.10.: dimensionless velocity (u_x/u_∞) field at $y = 0.01$ m using the Spalart-Allmaras model.

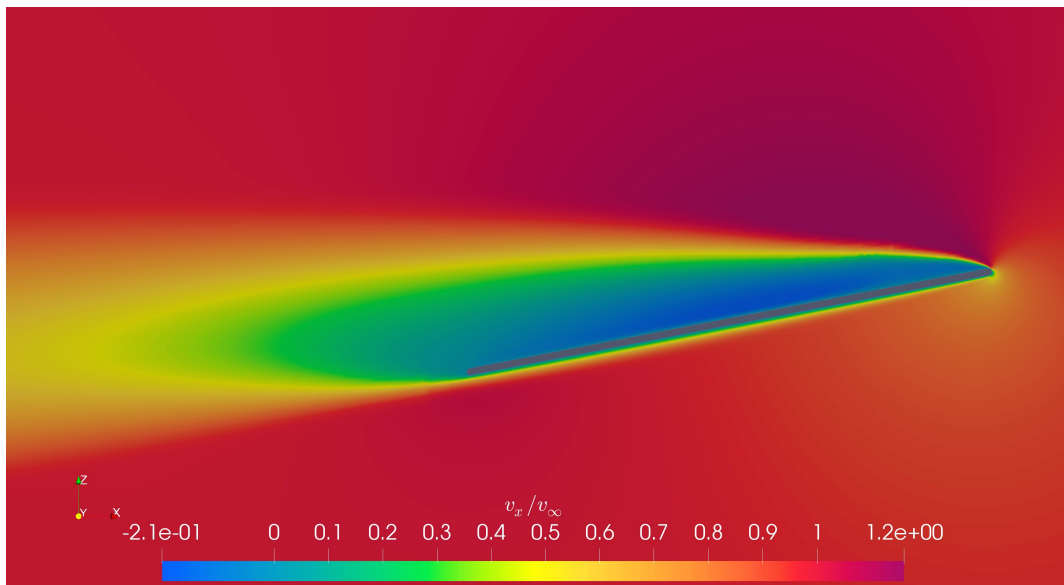


Figure 3.11.: dimensionless velocity (u_x/u_∞) field at $y = 0.01$ m using the SST $k-\omega$ turbulence model with $\gamma-Re_\theta$ transition model; $\nu_t/\nu=2.5$ inflow condition.

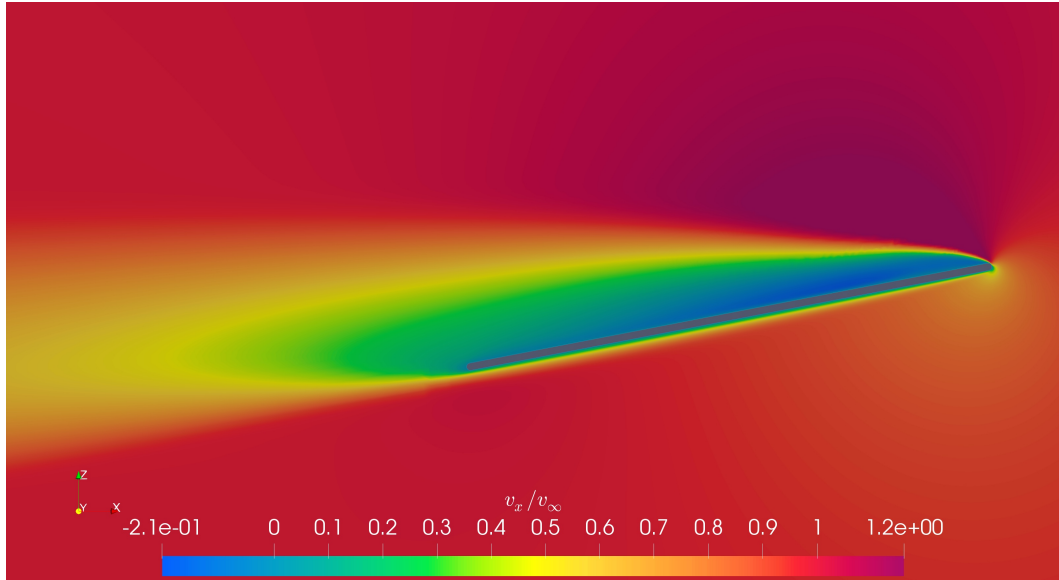


Figure 3.12.: dimensionless velocity (u_x/u_∞) field at $y = 0.01$ m using the SST $k - \omega$ turbulence model with $\gamma - Re_\theta$ transition model; $\nu_t/\nu=10$ inflow condition.

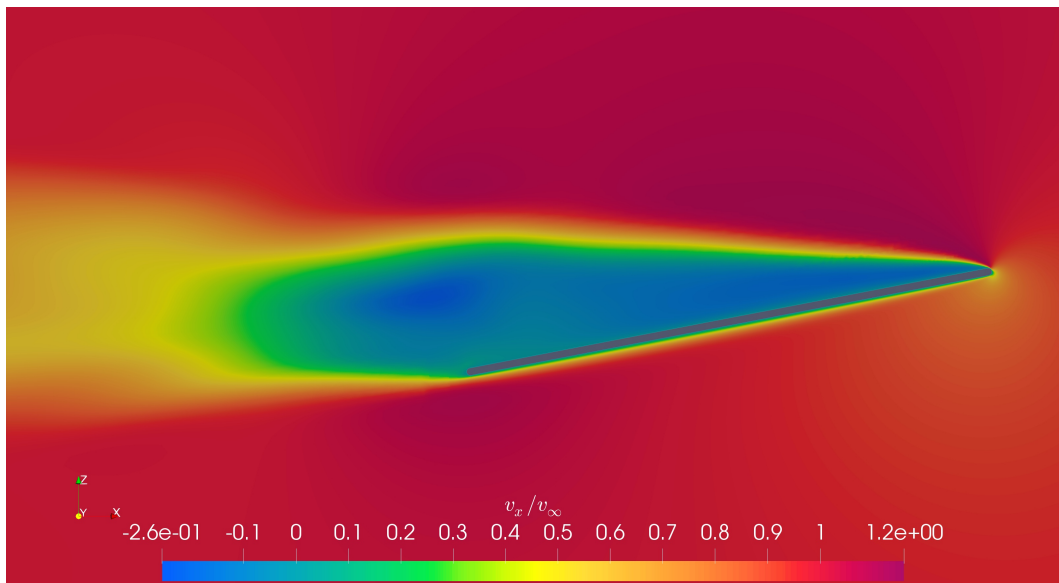


Figure 3.13.: dimensionless velocity (u_x/u_∞) field at $y = 0.01$ m using the PANS turbulence model (time-averaged solution).

Figure 3.14 shows some slices of instantaneous dimensionless velocity for different timeframes of the PANS simulation: the first part of the pattern is very similar to the one of the other models, but after about one third of chord length the unsteadiness of the flow becomes clear, with noticeable fluctuations being shed from the wing.

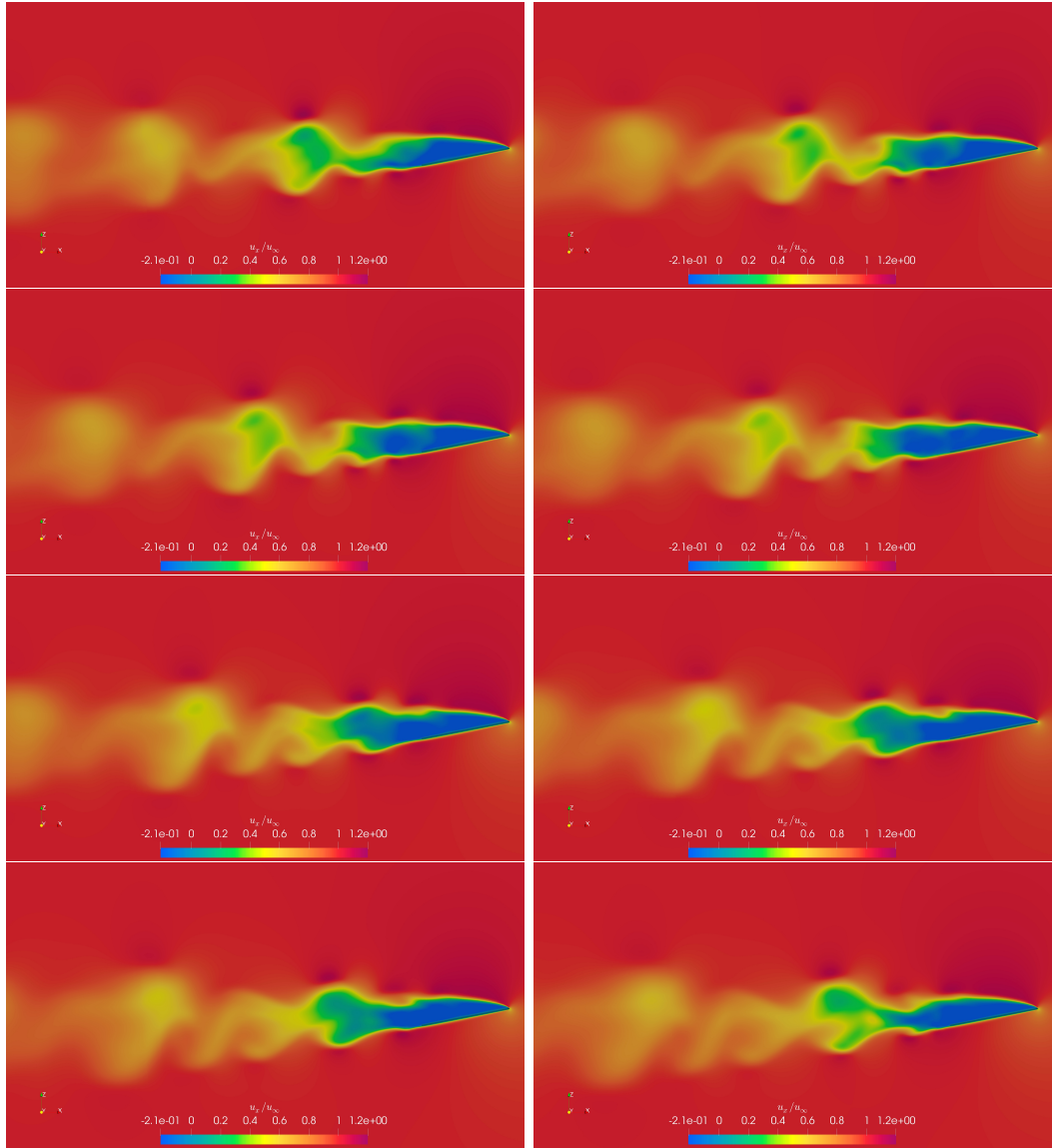


Figure 3.14.: PANS simulations: slice of dimensionless velocity field in x direction at $y = 0.01$ m at various timesteps.

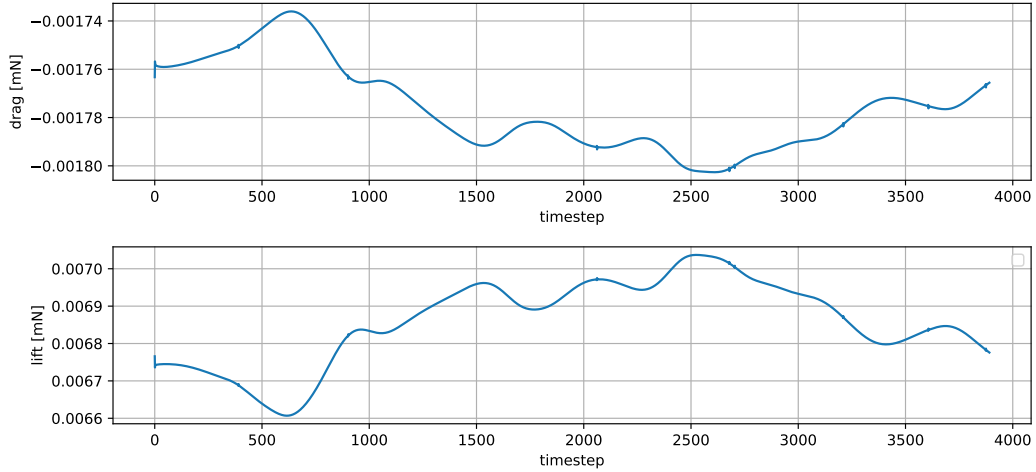


Figure 3.15.: Evolution in time of drag and lift forces for PANS simulation: finest grid, $\Delta t = 0.0001025$.

3.2.4. Unsteadiness of PANS simulations

As we already mentioned, PANS simulations produce unsteady results. Figure 3.15 shows the evolution in time of drag and lift force of the finest PANS simulation. It can be seen that the forces have random fluctuations of up to 3% of the mean value.

3.2.5. Development of turbulence in the flow

Since all the models used here are solving the same equation ((1.26)) and they differ from each other in the way of defining and computing ν_t , this parameter plays a key role in understanding the different behaviour of the various models. Figures 3.16, 3.17, 3.18 and 3.19 show the field of ν_t/ν on a domain slice at 1 cm from the symmetry plane. This variable represents the ratio of the magnitude of modelled turbulence to the viscosity of the fluid, telling us when the effects of the former are negligible and when they are not. In the plots, a white contour line highlights the region where $\nu_t/\nu = 2$, which can be considered as a gross threshold between the laminar and the turbulent part of the flow. As it can be seen, the various models all draw a similar pattern: turbulence kicks in at around one sixth of the wing length, with the SST $k - \omega$ having the least ν_t generation and the Spalart-Allmaras being the most productive. As visible in Figures 3.11 and 3.12, for the transition model a lower value of eddy viscosity in the free flow results in a more intense production of

it in the wake. The awkward shape of the white contour line in Figure 3.19 is due to the high inflow ν_t/ν value of 10, which is brought from the inflow to the wing. This is not happening for the same model with an inflow ν_t/ν ratio of 2.5 (Figure 3.18) because, as shown in [11], the lower the inflow amount of ν_t , the faster its decay will be, meaning that for this inflow value, through its path to the wing the eddy viscosity will decrease significantly.

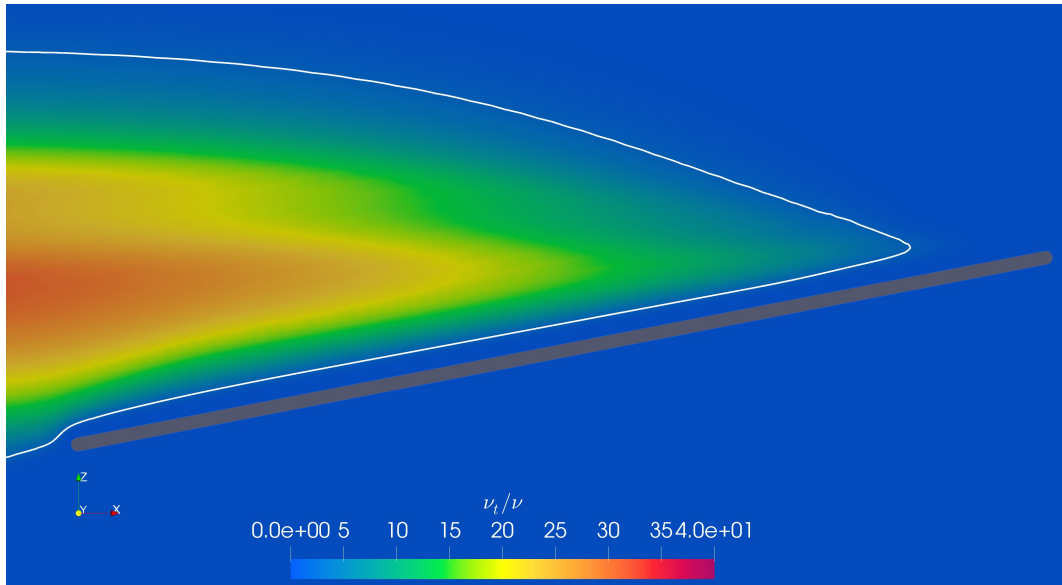


Figure 3.16.: Eddy viscosity intensity (ν_t/ν) field at $y = 0.01$ m sing the SST $k - \omega$ model. A white contour line marks where $\nu_t/\nu = 2$, value for which the effect of turbulence kicks in.

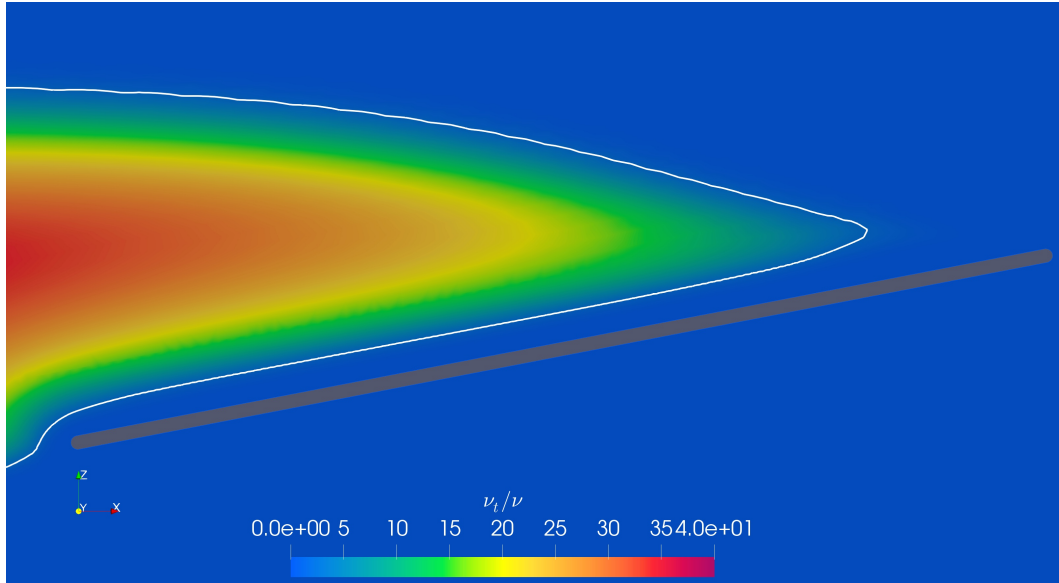


Figure 3.17.: Eddy viscosity intensity (ν_t/ν) field at $y = 0.01$ m using the Spalart-Allmaras model. A white contour line marks where $\nu_t/\nu = 2$, value for which the effect of turbulence kicks in.

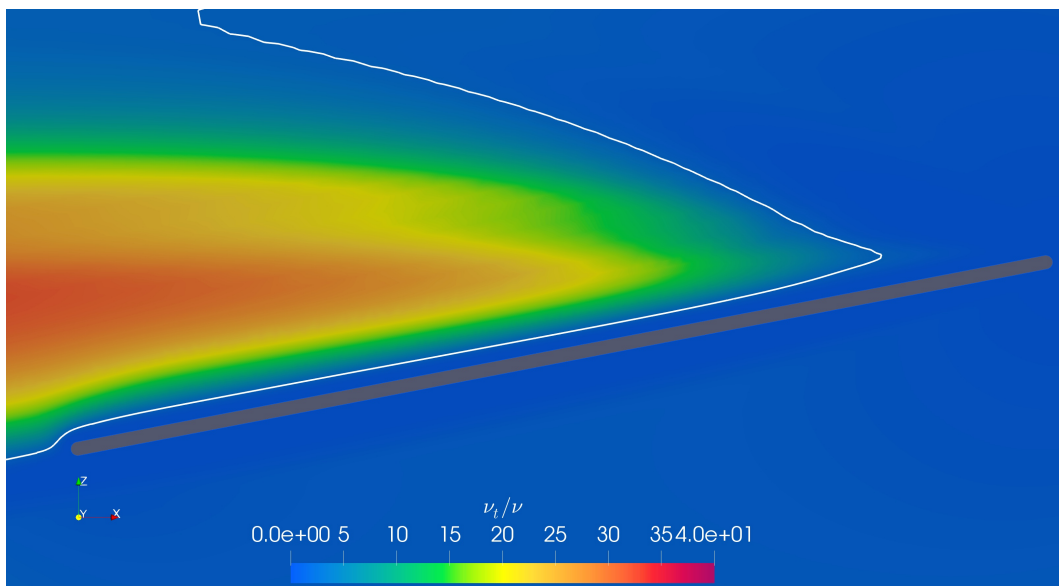


Figure 3.18.: Eddy viscosity intensity (ν_t/ν) field at $y = 0.01$ m using the SST $k-\omega$ turbulence model with $\gamma-Re_\theta$ transition model; $\nu_t/\nu=2.5$ inflow condition. A white contour line marks where $\nu_t/\nu = 2$, value for which the effect of turbulence kicks in.

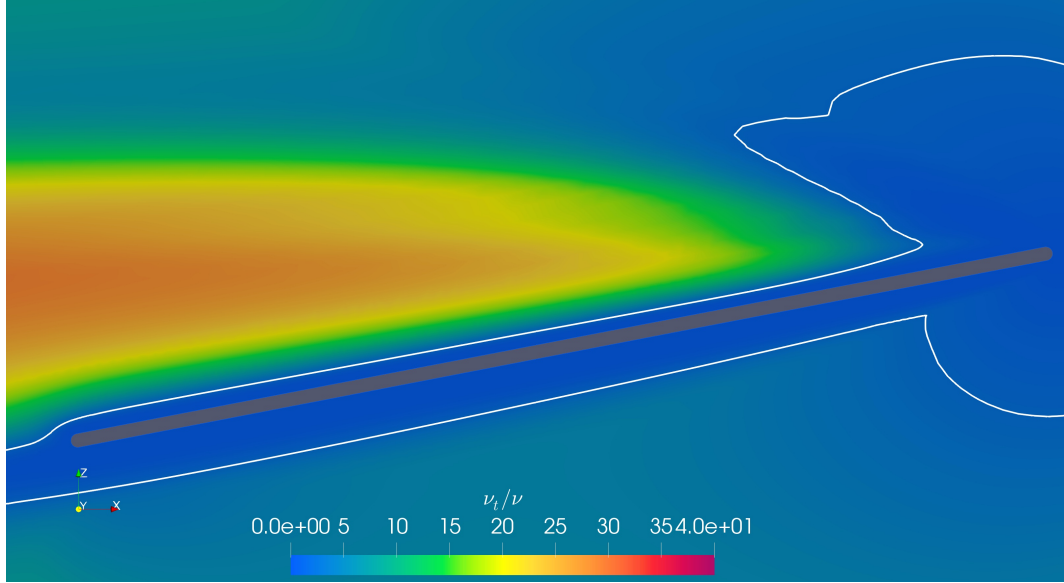


Figure 3.19.: Eddy viscosity intensity (ν_t/ν) field at $y = 0.01$ m using the SST $k - \omega$ turbulence model with $\gamma - Re_\theta$ transition model; $\nu_t/\nu=10$ inflow condition. A white contour line marks where $\nu_t/\nu = 2$, value for which the effect of turbulence kicks in.

An evaluation of the turbulent state of the flow is not that straightforward for PANS simulations, since ν_t becomes only the source of turbulence for the unresolved scales and is thus not describing the total level of turbulence. To overcome this problem, we tracked the values of instant velocity and pressure for seven points through the wing and we performed a fast Fourier transform on them to see which frequencies were characterising the flow in that positions. Figure 3.20 shows the location of the points on the wing in the xz plane ($y = 0.01$ m) and Figures 3.21 and 3.22 shows the evolution in time of the respective velocity components and their frequency response. This sequence of images shows how, sweeping the wing, the velocity field becomes unsteady and fluctuates with an increasing spectrum of (smaller) frequencies.

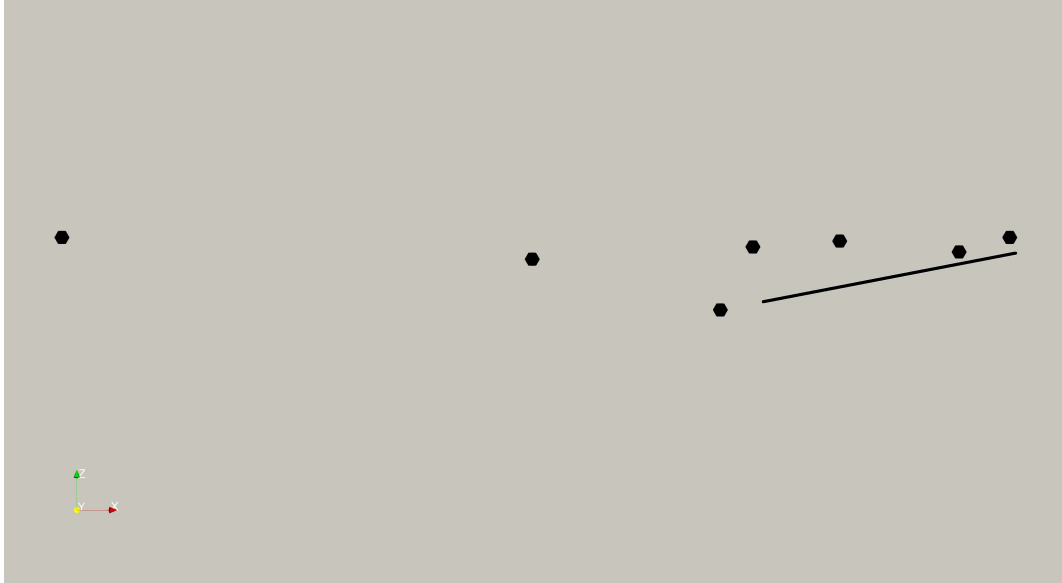


Figure 3.20.: Distributions of the points tracking velocity and pressure along the wing (black line); the y coordinate is 0.01 (as the previous plots of velocity and ν_t/ν). From right to left (inflow direction): `leadingEdge`, `wing1`, `wing2`, `wing3`, `trailingEdge`, `wing4`, `wake`.

Figure 3.21.: Time history of velocity and respective FFT transform for the tracking points `leadingEdge`, `wing1` and `wing2` (See Figure 3.20) used in the PANS simulations. $\Delta t = 0.0001025s$.

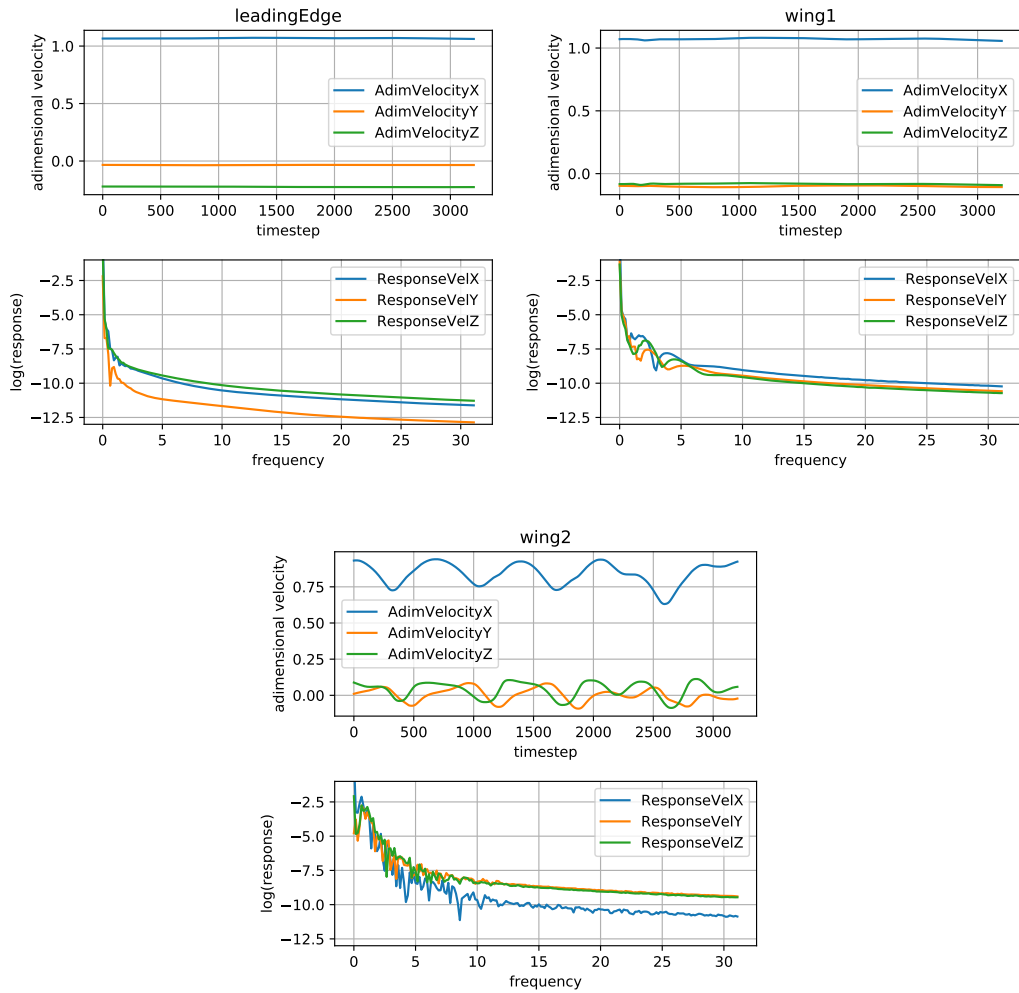
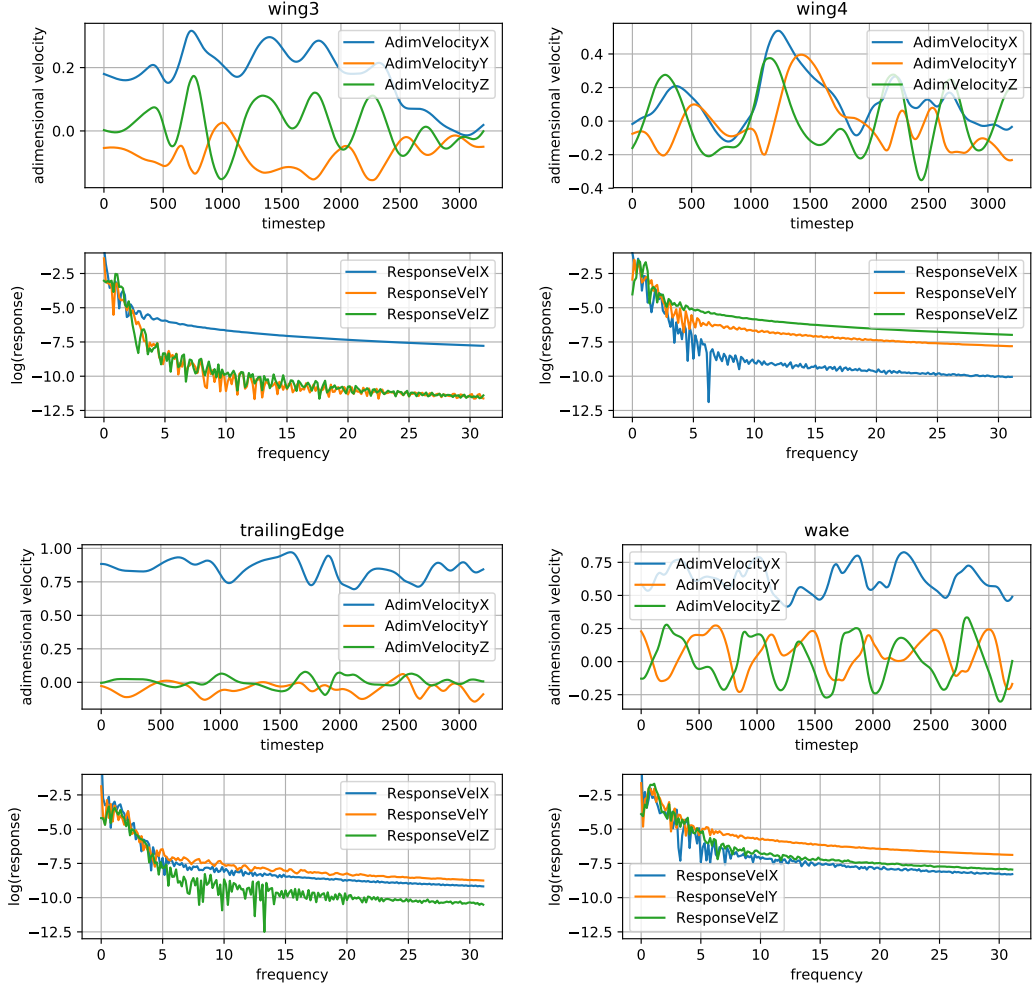


Figure 3.22.: Time history of velocity and respective FFT transform for the tracking points `wing3`, `wing4`, `trailingEdge`, `wake` (See Figure 3.20) used in the PANS simulations. $\Delta t = 0.0001025s$.



3.2.6. Turbulent intensity

We can compare the development of turbulence of PANS with the other models also in a quantitative sense and not only in the qualitative sense discussed in the previous subsection. The quantity we can use for this purpose is *turbulence intensity*, which is defined as (with reference to the nomenclature used in Chapter 1):

$$I_T = \frac{u'}{\bar{u}}, \quad (3.2)$$

where for sake of compactness we are using u' instead of $\|\mathbf{u}'\|_{L^2}$ and \bar{u} instead of $\|\bar{\mathbf{u}}\|_{L^2}$. Turbulence intensity is then a ratio between the magnitude of the fluctuations

of velocity from its mean value and the magnitude of the mean value itself. In the case of RANS models, where turbulence is fully modelled, the velocity solution corresponds to the average velocity, whereas the fluctuations are modelled by the eddy viscosity. Thus, we can define the modelled turbulence intensity as:

$$I_m = \frac{\sqrt{2/3k}}{\bar{u}}. \quad (3.3)$$

If, like for PANS, part of turbulence is resolved, the velocity solution doesn't correspond anymore to the average velocity, so we compute it averaging the velocity solutions in time considering all the timesteps simulated. The contribution to turbulence intensity given by the resolved scales of turbulence will then be:

$$I_r = \frac{u_{RMS}}{\bar{u}}, \quad (3.4)$$

with:

$$u_{RMS} = \sqrt{u_{i,RMS}^2}; \quad (3.5)$$

$$u_{i,RMS}^2 = \sqrt{\frac{1}{N} \sum_{j=1}^N (u'_{i,j})^2} = \sqrt{\frac{1}{N} \sum_{j=1}^N (u_{i,j} - \bar{u}_i)}, \quad (3.6)$$

where N is the number of timesteps taken into consideration and as $u_{i,j}$ is the i -th velocity component at the j -th timestep. Thus, for SST $k - \omega$, $\gamma - Re_\theta$ and Spalart-Allmaras simulations the total turbulence intensity will be:

$$I_T = I_m, \quad (3.7)$$

whereas for PANS simulations it will be computed as:

$$I_T = I_m + I_r. \quad (3.8)$$

Table 3.4 reports the values of turbulent intensity of the various models in the seven points tracked along the wing (See Figure 3.20). Interestingly, the PANS model produces the highest values of I_T at the leading edge and in the last three points downwind. In the former case, the modelled term (I_m) is dominant, whereas in the latter the resolved term (I_r) is the dominant one.

3.2.7. Pressure distribution

Figures 3.23, 3.24, 3.25, 3.26, and 3.27 show the pressure field acting on the wing, where the left wing represents the dorsal (suction) side and the right wing represents

model	turbulence intensity						
	leadingEdge	wing1	wing2	wing3	wing4	trailingEdge	wake
Spalart-Allmaras	4.157E-04	5.127E-01	6.312E-01	6.294E-01	3.423E-01	2.508E-01	8.024E-02
SST $k - \omega$	8.194E-04	8.083E-01	4.718E-01	5.807E-01	1.919E-01	2.840E-01	9.140E-02
$\gamma - Re_\theta$ 10	2.474E-02	2.225E+00	2.844E-01	2.708E-01	2.316E-01	1.840E-01	4.313E-02
$\gamma - Re_\theta$ 2.5	1.273E-02	9.709E-01	3.601E-01	3.743E-01	2.625E-01	2.275E-01	6.143E-02
PANS, I_m only	5.377E-01	5.172E-01	3.379E-01	1.661E-01	1.552E-01	1.168E-01	1.069E-01
PANS, I_r only	4.069E-03	1.103E-02	1.231E-01	6.369E-01	2.559E+00	9.722E-02	3.647E-01
PANS	5.418E-01	5.283E-01	4.609E-01	8.030E-01	2.715E+00	2.140E-01	4.716E-01

Table 3.4.: Turbulent intensity at the seven tracked points (See Figure 3.20) for the various models used. Among them, PANS is the most productive at the leading edge -where the modelled turbulent intensity (I_m) term is dominant- and in the wake region -where the resolved turbulent intensity (I_r) is dominant.

the ventral (pressure) side. The simulations using SST $k - \omega$, SST $k - \omega$ with $\gamma - Re_\theta$ with inflow condition $\nu_t/\nu = 2.5$ and PANS result in milder values than the other two, which highlight more intense suction (on the dorsal side) and pressure (on the ventral side) in the region close to the leading edge.



Figure 3.23.: Pressure field on the wing using the SST $k - \omega$ model. On the left the dorsal (suction) side, on the right the ventral (pressure) side.



Figure 3.24.: Pressure field on the wing using the Spalart-Allmaras model. On the left the dorsal (suction) side, on the right the ventral (pressure) side.

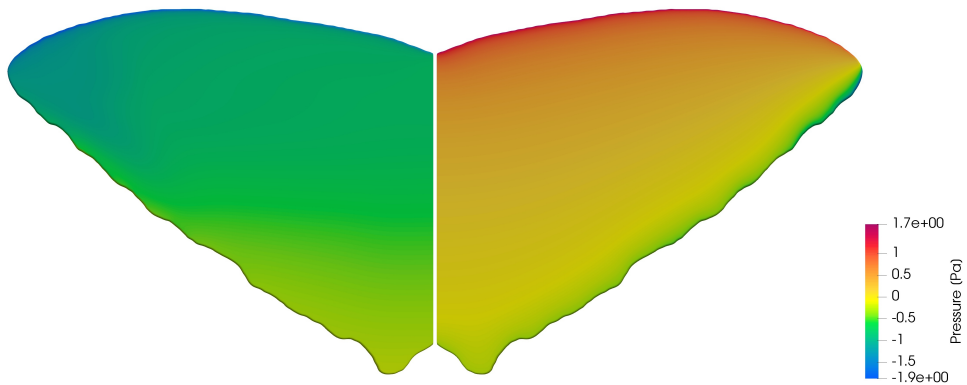


Figure 3.25.: Pressure field on the wing using the SST $k - \omega$ turbulence model with $\gamma - Re_\theta$ transition model; $\nu_t/\nu=2.5$ inflow condition. On the left the dorsal (suction) side, on the right the ventral (pressure) side.



Figure 3.26.: Pressure field on the wing using the SST $k - \omega$ turbulence model with $\gamma - Re_\theta$ transition model; $\nu_t/\nu=10$ inflow condition. On the left the dorsal (suction) side, on the right the ventral (pressure) side.



Figure 3.27.: Pressure field on the wing using the PANS turbulence model. On the left the dorsal (suction) side, on the right the ventral (pressure) side.

3.2.8. Limiting streamlines

Figures 3.28, 3.29, 3.30, 3.31 and 3.32 show the limiting velocity streamlines on the wing (where, again the left wing represents the dorsal side and the right wing the ventral side). Such streamlines consist in the *wall shear stress* vector field, which is defined as:

$$\tau_{w,i} = \mu \left(\frac{\partial u_i}{\partial y} \right)_{y=0}, \quad (3.9)$$

where here y represents the direction normal to the wing. From the figures it is possible to observe that the separation bubble sweeps the whole chord length on the entire wing and that whereas the Spalart-Allmaras simulation results in tidy streamline pattern on both the wing sides, the other models highlight the rise of more curly streamlines close to the wingtip on the dorsal side. The ventral side has a very tidy streamline pattern in all the cases.

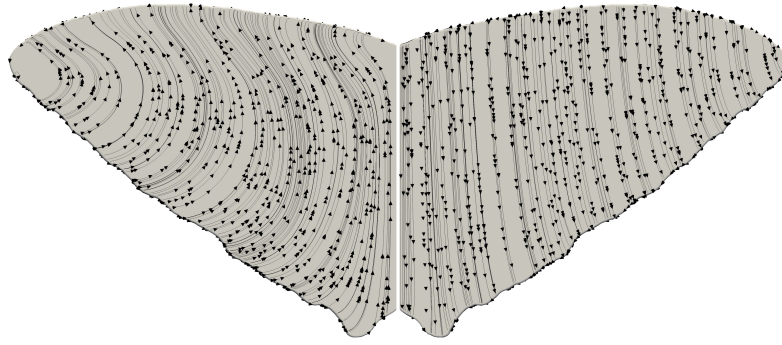


Figure 3.28.: Limiting streamlines (shear stress field) on the wing using the SST $k - \omega$ model. On the left the dorsal (suction) side, on the right the ventral (pressure) side.

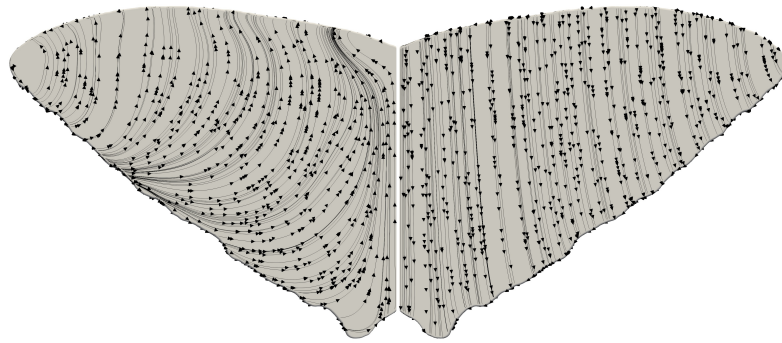


Figure 3.29.: Limiting streamlines (shear stress field) on the wing using the Spalart-Allmaras model. On the left the dorsal (suction) side, on the right the ventral (pressure) side.

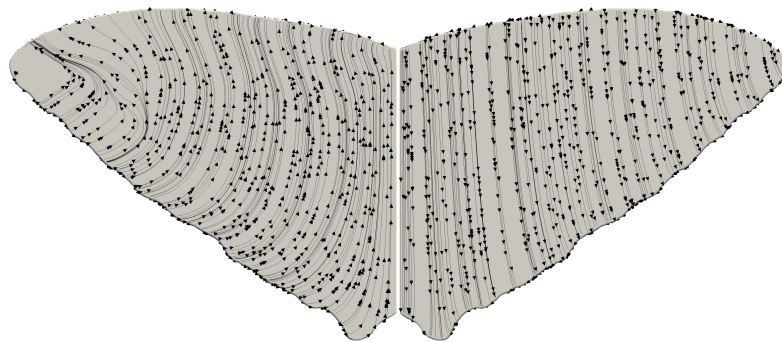


Figure 3.30.: Limiting streamlines (shear stress field) on the wing using the SST $k - \omega$ turbulence model with $\gamma - Re_\theta$ transition model; $\nu_t/\nu=2.5$ inflow condition. On the left the dorsal (suction) side, on the right the ventral (pressure) side.

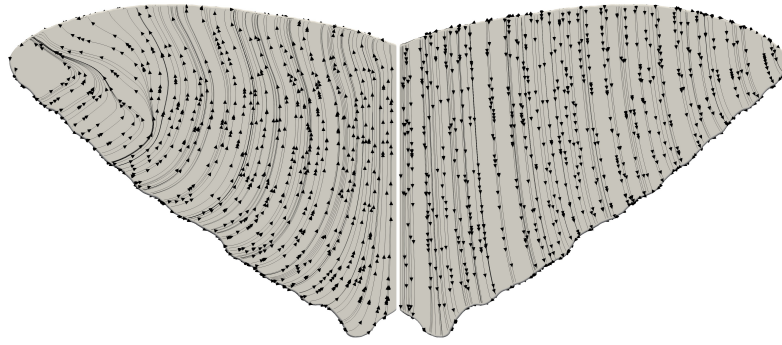


Figure 3.31.: Limiting streamlines (shear stress field) on the wing using the SST $k-\omega$ turbulence model with $\gamma-Re_\theta$ transition model; $\nu_t/\nu=10$ inflow condition. On the left the dorsal (suction) side, on the right the ventral (pressure) side.



Figure 3.32.: Limiting streamlines (shear stress field) on the wing using the PANS turbulence model. On the left the dorsal (suction) side, on the right the ventral (pressure) side.

3.3. Comparison of the numerical simulations with experimental results

Figure 3.33 shows a comparison of the experimental results and the values of drag and lift of the numerical simulations, which are plotted with an error bar showing the discretisation uncertainty; this plot shows that, considering the force values and their range of uncertainty, the simulation using $\gamma-Re_\theta$ model and $\nu_t/\nu=10$ inflow condition is the only one that can be clearly discarded, whereas the others provide results comparably close to the experimental ones. Nevertheless, Table 3.5, gathering the values of this comparison with the difference percentage with

respect to the experimental results, shows instead that if we only consider the exact force values, PANS model gives the closest results to experiments, followed by SST $k - \omega$. Table 3.6 reports the values of the ratio between lift and drag forces of the experimental values and the numerical simulations, together with the respective numerical uncertainty estimation and the percentage difference between experiments and simulations. This parameter, which will be discussed more in detail in the next chapter, gives a measure of the global efficiency of the wing during flight and here it confirms again that the best results are achieved by PANS model, followed by SST $k - \omega$.

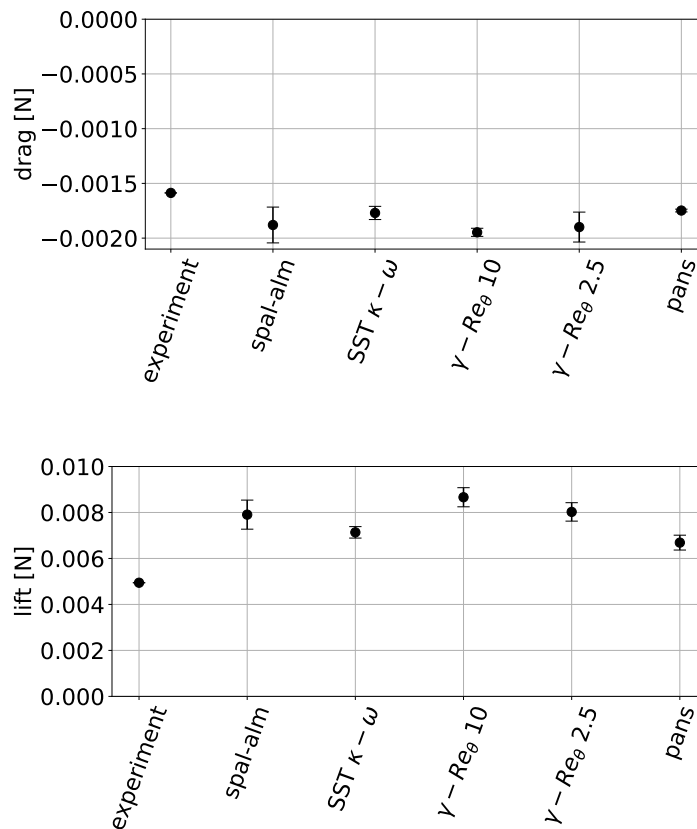


Figure 3.33.: Drag and lift of experiments and numerical simulations compared. The values are taken from the finest grid setups and the error bars represent numerical uncertainty due to spatial (and temporal for PANS) discretisation.

aerodynamic forces comparison				
	drag [N]	lift [N]	% drag Err	% lift Err
experimental	-1.587E-03	4.944E-03	-	-
Spalart-Allmaras	-1.880E-03	7.906E-03	18.42	59.90
SST $k - \omega$	-1.770E-03	7.136E-03	11.52	44.32
$\gamma - Re_\theta$ 10	-1.947E-03	8.663E-03	22.64	75.21
$\gamma - Re_\theta$ 2.5	-1.899E-03	8.025E-03	19.63	62.30
PANS	-1.748E-03	6.689E-03	10.15	35.28

Table 3.5.: Resume of drag and lift values of the numerical simulations (with the finest grid and timestep) ad the experimental values; the last two columns show the percentage difference of the values with respect to the experimental ones.

lift-to-drag ratio comparison			
	L/D [-]	% L/D numerical uncertainty	% L/D Err
experimental	3.115		-
Spalart-Allmaras	4.206	3	-0.350
SST $k - \omega$	4.031	7.4	-0.294
$\gamma - Re_\theta$ 10	4.450	3.5	-0.429
$\gamma - Re_\theta$ 2.5	4.226	2.5	-0.357
PANS	3.825	5.53	-0.228

Table 3.6.: Resume of lift-to-drag ratio values of the numerical simulations (with the finest grid and timestep) ad the experimental values; the last column shows the percentage difference of the values with respect to the experimental ones.

3.4. Discussion

The results show that in terms of flow topology the models give similar answers, with the main difference lying in the unsteady nature of the PANS solution, which is the only one able to catch the stream oscillations that are suggested by Figure 1.4. This difference is though not playing a fundamental role if we consider the time-averaged flow of the PANS simulation, which gives the same pattern showed by the other models. Table 3.5 shows that the predicted forces provided by the numerical simulations overestimate the drag and lift of 10-20% and 35-70% respectively. Thus, if for the prediction of drag all the models lie in a small range, for the lift prediction the SST $k - \omega$ and PANS models give considerably better results, with the latter giving the ones closest to experimental values. Nevertheless, none of the computational results, together with their uncertainty range, matches with the experimental values. The reasons for this discrepancies could come from different sources:

- the simplifications made for the wing model are significant: modelling the body of the butterfly could for example bring to changes in lift and drag production;
- [22] reports that the indoor conditions of the insectary could alter the behaviour of the insects, which sometimes followed more frenetic trajectories; this could lead to some noise in the experimental data;
- by averaging the values of drag and lift extrapolated, we could neglect some unsteady processes playing a role in the production of aerodynamic forces;
- we assume that the flight kinematics were recorded in still air conditions; considering the weight of the butterfly (around 0.5 grams) though, it is not hard to believe that mild air currents can easily affect the natural trajectory of the insects, which translates in a source of error in the drag and lift estimation using inverse dynamics;
- the numerical simulations are based on the geometry of non damaged wings; in practical terms, [22] shows that, during their lifetime, *Morpho* butterflies are subjected to wing deterioration, which can result in losses of flight performances.

To sum up, the results highlight that if we are only interested in the forces acting on the butterfly and in the mean flow topology, the various models used give com-

parable results, showing small relative differences, although none of them matches the experimental results. Compared to the other models, PANS gives an interesting option to catch the unsteadiness nature of the flow that experimental results have shown; it is important though to say that this comes at a much higher computational cost. In practical terms, if we also take into account the number of timesteps needed to reach a reliable solution and the trend of the residuals, we consider the SST $k - \omega$ to be the best solution in terms of results-to-costs ratio.

4. Comparing Different Morpho Species By Means Of Computational Fluid Dynamics

Float like a butterfly, sting like a
bee.

Muhammad Ali

4.1. Setup and Considerations

In this chapter we perform several simulations for two different *Morpho* species, the *cisseis* and the *deidamia*. Following [22], the former belongs to the *canopy* group, which gathers butterfly species characterised by the tendency of flying at a considerable height from the ground, above the trees, whereas the latter belongs to the *understory* specie group, which gathers butterfly species which generally fly closer to the ground, inside the forest. The *cisseis* is a gliding specialist, performing flap-gliding flight characterised by long and neat gliding phases ([22]). Here, using the setups discussed in Chapter 2, we aim at evaluating the flight performances of the two species in the range of 2-20 degrees of angle of attack for gliding flight and in the range of 15-75 degrees for flapping flight. The two species have different morphological characteristics, with the *cisseis* being bigger and lighter than the *deidamia*. A resume of size and flight details of the two butterflies is given in Table 4.1.

Since in Chapter 3 we stated that the model with the best performance-on-cost ratio is the SST $k - \omega$, all the simulations have been run using this model.

specie	Mean glide velocity [m/s]	mean weight [g]	mean chord length [cm]	wing surface area [cm ²]	hinge-to-tip length [cm]	aspect ratio [-]	Reynolds Number [-]
<i>cisseis</i>	1.50E+00	5.80E-01	4.82E-02	4.40573E+03	8.75E+00	3.63E+00	4.89E+03
<i>deidamia</i>	2.07E+00	6.39E-01	3.91E-02	2.57824E+03	7.56 E+00	3.86E+00	5.47E+03

Table 4.1.: Morphological and flight characteristics of *Morpho cisseis* and *deidamia*.

4.1.1. Gliding setup

Regarding the ReFRESCO options, for gliding flight the same choices made for the SST $k - \omega$ based simulations of Chapter 3, except for the following points:

- outerloop:
 - max n° iterations: 15000;
 - check residual norm: L^∞ ;
 - convergence tolerance: 1E-14;
 - convergence check skipped for: false;
- momentum equations:
 - explicit relaxation: 1.5E-01;
- pressure equation:
 - explicit relaxation: 1.0E-01;
- turbulence equations:
 - explicit relaxation: 1.5E-01;
- timeloop:
 - unsteady: false.

The option of running steady simulations comes naturally from the results of Chapter 3, which are represented by a steady state flow.

Simulations are run for angles of attack from 2 to 20 degrees with steps of two degrees. For each angle of attack five different grids are used, in order to perform an estimation of the uncertainty due to spatial discretisation. The processes for the generation and rotation of the grids are the ones described in Sections 2.3.1 and 2.3.2. The coarsest mesh is generated with the following settings:

- number of gross cells in the x, y and z directions respectively: 12, 6, 12;
- number of refinements on the top and bottom surfaces of the wing: 8;
- number of refinements on the wing edge: 10;
- first viscous layer height: 1.0E-05 m.

The number of cells and the y^+ values at various angles of attack are gathered in Tables B.1 and B.2 of Appendix B. No box refinements are applied, as in Chapter 2 it has been stated that they play a negligible role in the computation of aerodynamic forces. The side view of the used grids is visible in Figure 2.12 (a).

For these simulations, we chose an inflow velocity such that the two wings were operating at the same Reynolds number of 5200, in order to have the same dynamical conditions for the different species; to achieve that, simulations for the *cisseis* are run with an inflow velocity value of -1.59 m/s, whereas for the *deidamia* such value has been set to -1.97 m/s.

4.1.2. Flapping setup

The surfaces composing the domain are shown in Figure 4.1; the simulations are performed rotating the wing around its hinge for 360° in still air at a fixed angle of attack and constant rotational velocity.

The ReFRESKO options used for this simulations differing from the SST $k - \omega$ ones performed in Chapter 3 are the following:

- boundary conditions (see Figure 3.3):
 - **wing surface:** velocity no-slip condition;
 - **side:** pressure 0 Pa (free stream);
 - **ceiling:** pressure 0 Pa (free stream);
 - **floor:** pressure 0 Pa (free stream);
- outerloop:
 - **max n° iterations:** 300;
 - **check residual norm:** L^∞ ;
 - **convergence tolerance:** 1E-6;

- convergence check skipped for: $k - \omega$ equations;
- momentum equations:
 - explicit relaxation: 3E-01;
- pressure equation:
 - explicit relaxation: 3E-01;
- turbulence equations:
 - explicit relaxation: 3E-01;
- timeloop:
 - unsteady: true;
 - solution scheme: implicit three time level scheme;
 - time delta: 6.66667E-04 s;
 - total timesteps: 360.

Simulations are run for angles of attack from 15 to 75 degrees with steps of two degrees; for each of them a total of 360 timesteps is considered (using a timestep of 6.66667E-04 s and a rotational velocity of 1500 °/s implies that one timestep corresponds to one degree of revolution). With these settings we avoid that the wing captures its own wake, which would produce effects that we don't want to take into account in our study. For each simulation, results of drag and lift are taken at the last timestep. Only one grid is used, due to computational cost limitations. The grids have been generated with the same criteria used for the coarsest gliding meshes (number of initial cells, number of surface refinements, first layer thickness, absence of box refinements). A first grid was generated with $\alpha = 45^\circ$ and then rotated to the various α studied; this choice minimizes the skewness of the generated meshed caused by the deformation applied, since α lies in the range $15^\circ - 75^\circ$. The number of cells and the y^+ values at various angles of attack are gathered in Tables [B.3](#) and [B.4](#).

For these simulations we didn't follow the same Reynolds number-equalising idea as in the gliding flight simulations, since the definition of the Reynolds number for a rotational simulation is not as neat and straightforward as it is for the gliding

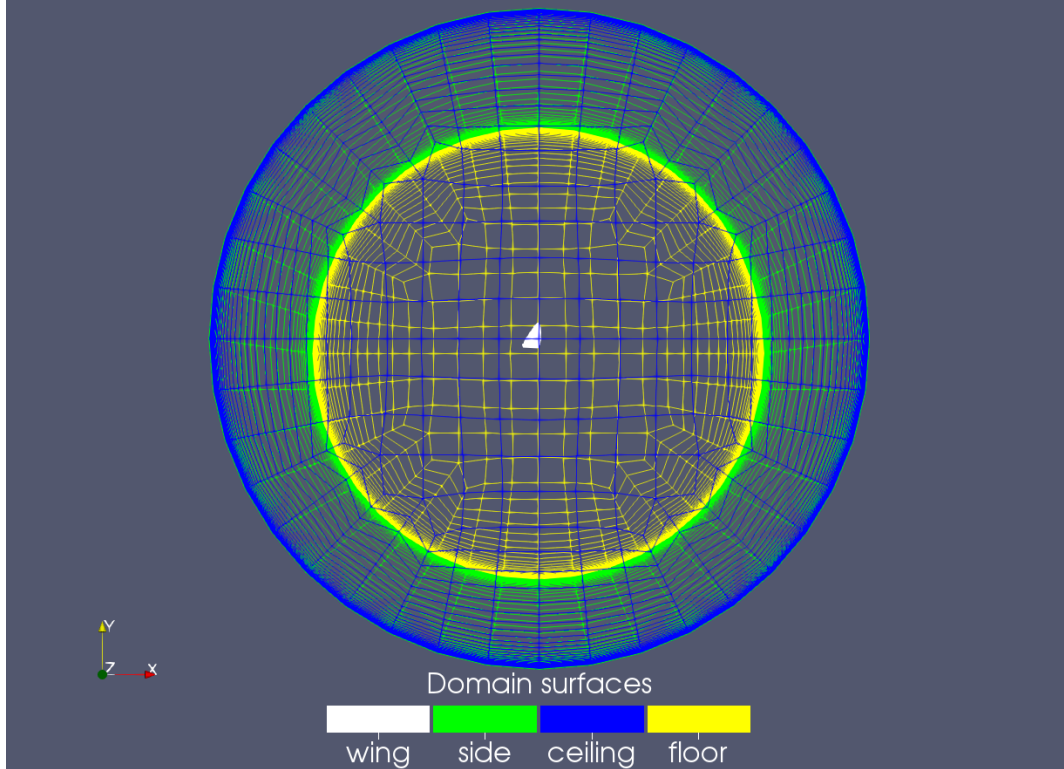


Figure 4.1.: Boundary surfaces of the numerical domain for the flapping simulations.

setup. The rotational velocity of the wing used for all these simulations has a value of $-1500^\circ/\text{s}$, which is compatible with the flapping flight kinematics reported in [22].

4.2. Results

4.2.1. Residuals

For gliding flight simulations the trends of L^2 and L^∞ norms of residuals is generally monotonically decreasing to values lower than 10^{-10} . For some angles of attack, simulations with the coarser grids show stagnation of residuals at higher values: since for all these cases the finer grids provide again decreasing residual trends, we can link this flaw to the coarseness of the grid that might originate problems in the convergence. This phenomenon is visible for the *cisseis* simulations with angles of attack of 16, 18 and 20 degrees and for the *deidamia* ones with angles of attack of 12, 14 and 16 degrees. For sake of continuity and readability only the case of the *deidamia* at $\alpha = 12^\circ$ is reported in Figure 4.2, where the difference in residuals trend between the coarsest and finest meshes is clearly noticeable.

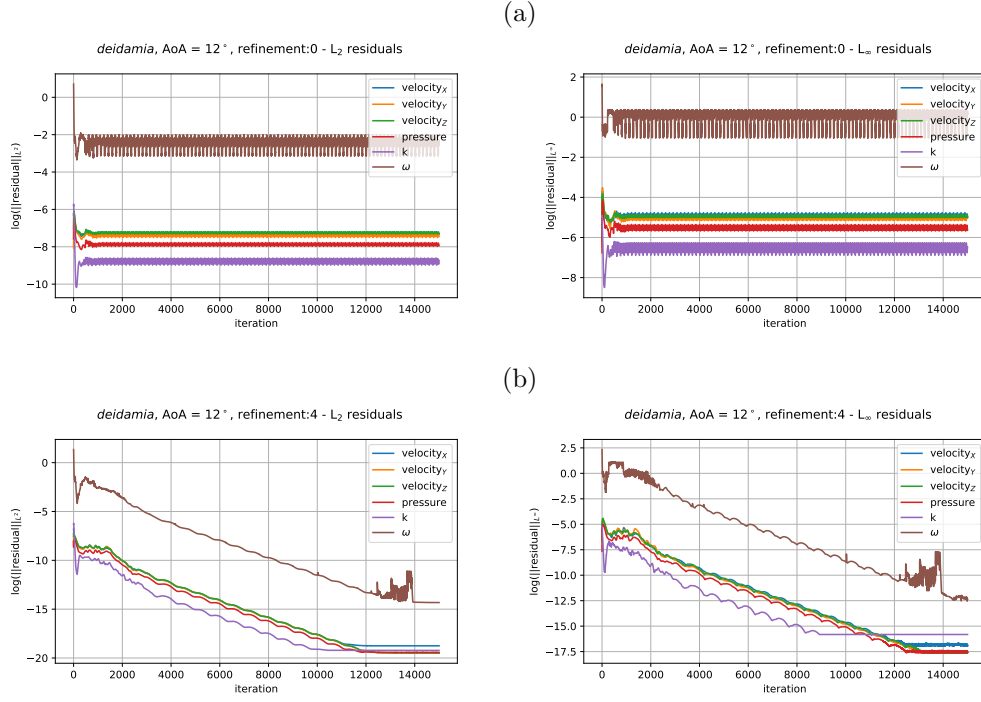


Figure 4.2.: L^2 and L^∞ norms of residuals for *deidamia* gliding at $\alpha = 12^\circ$, for the coarsest (a) and finest (b) grids.

To double check the achievement of convergence of the various simulations, this approach has been followed: first of all we define the functions $D(\text{iteration})$ and $L(\text{iteration})$, which are respectively the drag and lift force at each iteration; then, we define D_{avg} and L_{avg} as constant functions being equal to the average values of the previous functions. This allows us to define the following quantities:

$$Res_{ij}^{D,N} = \|(D - D_{avg})\|_{L^2}, \quad (4.1)$$

$$Res_{ij}^{L,N} = \|(L - L_{avg})\|_{L^2}, \quad (4.2)$$

where N here means that the last N iterations of the simulations are considered, i is the angle of attack and j the grid refinement level (0 = coarsest, 4 = finest). At this point, since we are expecting a steady solution, we also expect that for a reasonable value of N values should tend to zero. This quantities are reported in Tables B.5 and B.6, showing values close to zero ($<1E-17$) for all the simulations run on the finest grids. Nevertheless, for the coarser grids this is not always the case, due to the convergence issues previously discussed.

The residuals of the flapping simulations can't be checked with the same proce-

ture, since we are dealing there with unsteady simulations. Figure 4.3 shows the norms of the residuals of the last 600 iterations of a flapping simulation: it is clearly visible that for each timestep (up to 300 iterations) the residuals decrease of about four orders of magnitude.

4.2.2. Numerical uncertainties

For gliding flight simulations, the numerical uncertainties due to spatial discretisation are computed using the data from the five levels of grid refinement as previously explained. They can be visualised as errorbars in Figure 4.4¹, whereas the full trend of convergence for each angle of attack is reported in Appendix B. It is important to point out that the high uncertainty computed for the lift of the *cisseis* at $\alpha = 8^\circ$ is most likely overestimated, since the respective trend is not of order 2 but the oscillations of lift between the different grids are very small: it is possible that the fitting procedure reacts with an exaggerated safety factor.

4.2.3. Drag and lift coefficients

The main goal of this chapter lies in the investigation of the performances of the two wingshapes. For this reason, we may be less interested in the details of the flow for now. The first quantity we want to compare between the two wingshapes is the *drag coefficient*, defined as:

$$C_D = \frac{\mathbf{D}}{\frac{1}{2}\rho u_\infty^2 A_\alpha}, \quad (4.3)$$

where \mathbf{D} is the drag force, u_∞ is the free stream velocity, for us the inflow velocity, and A_α is the surface area of the wing multiplied by the cosine of the angle of attack. Similarly, we want to compare the two wings by means of the *lift coefficient*, which is defined as:

$$C_L = \frac{\mathbf{L}}{\frac{1}{2}\rho u_\infty^2 A_\alpha}, \quad (4.4)$$

where \mathbf{L} is the lift force.

These two dimensionless coefficients allow us to make a comparison of the two wings aerodynamics taking into account the whole dynamical pattern characterising

¹The uncertainties have been computed on the force values, but since for a fixed angle of attack the respective coefficients are obtained only by a multiplication with a constant value, they can be applied also to the coefficients themselves.

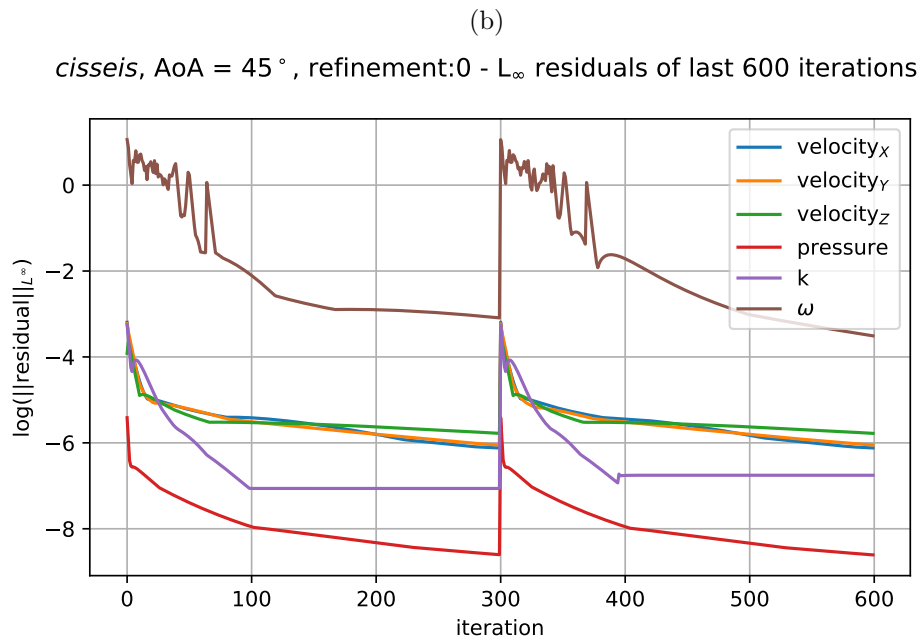
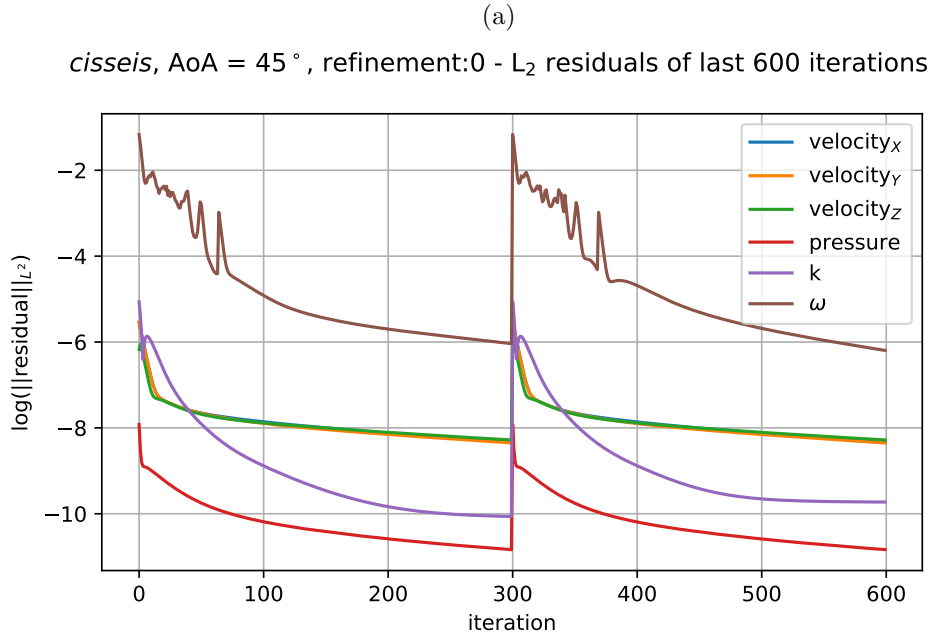


Figure 4.3.: L² (a) and L[∞] (b) norms of residuals for *cisseis* flapping at $\alpha = 45^\circ$, for the last 600 iterations.

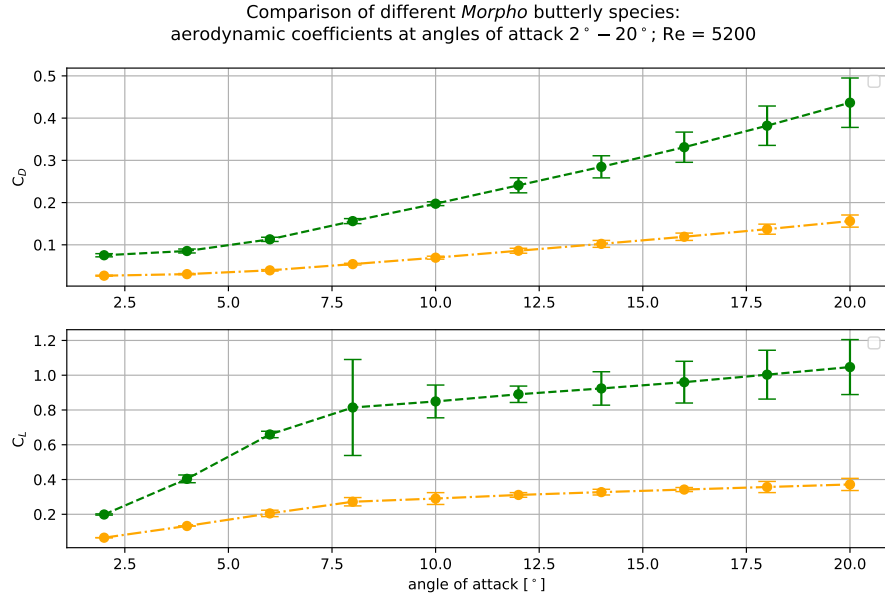


Figure 4.4.: Comparison of drag coefficient (C_D) and lift coefficient (C_L) of *cisseis* and *deidamia* wingshapes during gliding flight at angles of attack in the range 2°-20°.

the two cases -which means that not only drag (or lift) force but also free stream velocity, air density and geometry of the object are considered. Figure 4.4 reports the two coefficients versus the angle of attack for gliding flight, showing that the *cisseis* produces more intense aerodynamic forces.

The same comparison for flapping flight is visible in Figure 4.5, where again the *cisseis* appears to produce more intense aerodynamic forces.

4.2.4. Lift-to-drag ratio

In practical terms, the two previous coefficients don't provide complete insights about the performances of the two butterflies, since they don't evaluate the flight efficiency and energy consumption of the insects. To answer this question we will use another dimensionless parameter, the *lift-to-drag ratio*, which is defined as:

$$L/D = \frac{C_L}{C_D} = \frac{\mathbf{L}}{\mathbf{D}}. \quad (4.5)$$

This parameter brings very precise information about the flight efficiency of the animal ([34]), since it takes into account simultaneously both how much it "costs" to advance through the fluid and how much this cost is paid back in terms of vertical

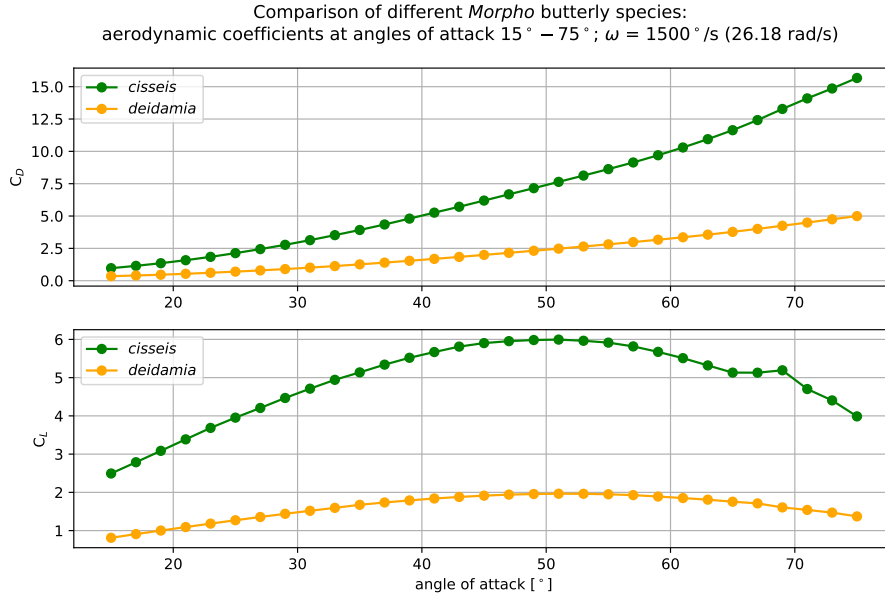


Figure 4.5.: Comparison of drag coefficient (C_D) and lift coefficient (C_L) of *cisseis* and *deidamia* wingshapes during flapping flight at angles of attack in the range 15° - 75° .

thrust. Figures 4.6 and 4.7 show the evolution of L/D with the angle of attack for gliding and flapping flight respectively, showing an important aspect: whereas in gliding conditions the difference between the two species reaches values of around 10% (See Figure 4.6, angle of attack 6°) of the lift-to-drag ratio, in flapping conditions this percentage plummets to values close to zero. This fact explains why the *cisseis* -the gliding specialist- performs such neat and smooth gliding phases during its flight, whereas the *deidamia* needs to flap with higher frequency. The following part of this section will analyze different aspects of the flow pattern to investigate the different behaviour of the two species.

4.3. Pressure distribution in gliding flight

In Chapter 3 we compared the pressure field on the wing for the different models. Nevertheless, to accomplish a more thorough analysis of the differences between the two species, we will now use the *pressure coefficient* instead, which, since our free stream pressure is null, can be defined as:

$$C_p = \frac{p}{\frac{1}{2}\rho v_\infty^2}. \quad (4.6)$$

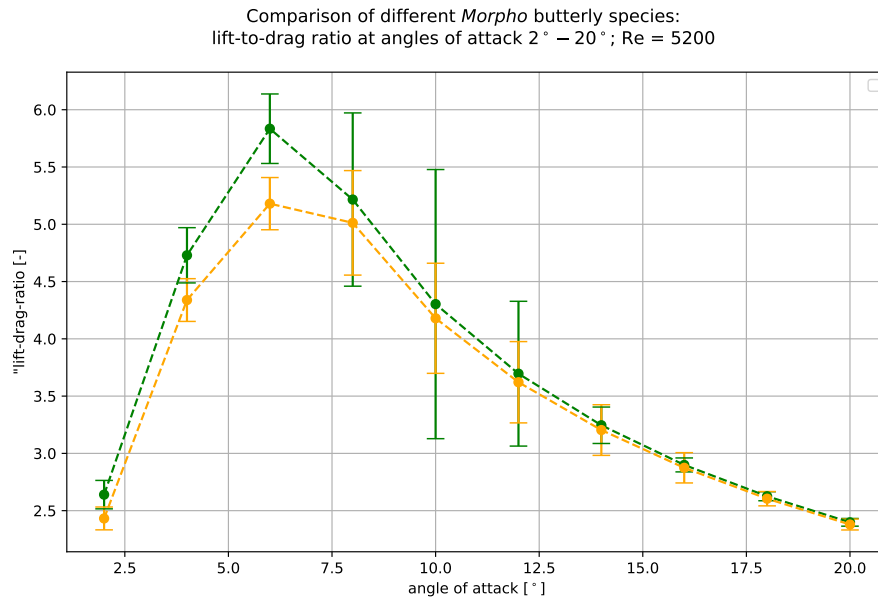


Figure 4.6.: Comparison of lift-to-drag coefficient (L/D) of *cisseis* and *deidamia* wingshapes during gliding flight at angles of attack in the range 2°-20°.

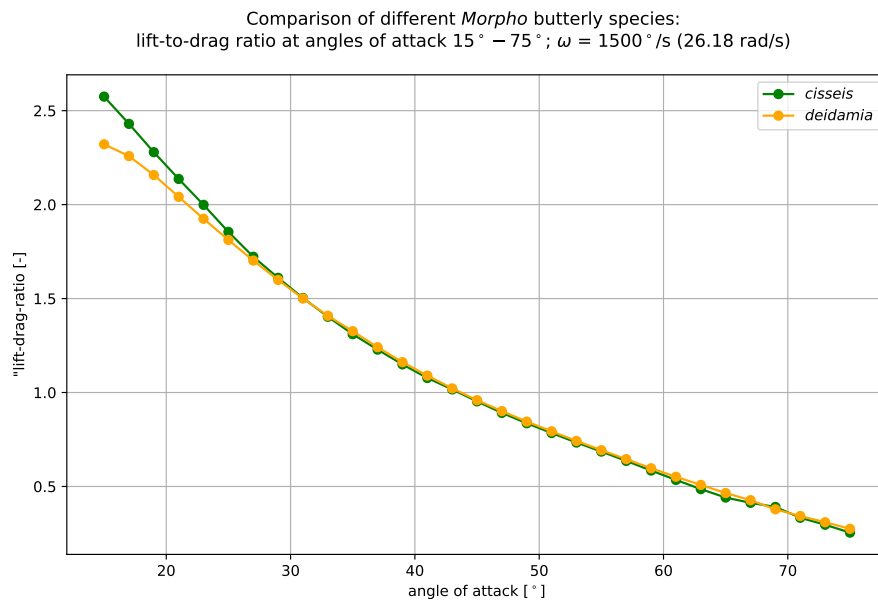


Figure 4.7.: Comparison of lift-to-drag coefficient (L/D) of *cisseis* and *deidamia* wingshapes during flapping flight at angles of attack in the range 15°-75°.

As for the previously introduced coefficients, C_p allows us to look at pressure values which are taking into account the whole dynamical pattern of the flow (in this case, the different inflow velocity). Figure 4.8 shows, for the two wings with an angle of attack of 6° , the distributions of C_p : we are focusing on this angle of attack since it shows the biggest difference in lift-to-drag ratio between the two species and therefore we reckon it could show more precisely the discrepancies between the two wings.

The values of C_p on the ventral side of the two wings have the same magnitude and pattern, whereas some differences are visible on the dorsal side: the rear boundary of the zone of negative C_p -which translates to a more conspicuous suction- tends to follow the shape of the rear wing edge. For this reason the *cisseis*, having a regular and straight shape linking the wingtip to the rear wing root, keeps negative values of C_p (represented in Figure 4.8 by green colours) for more than half of the wing surface, whereas the *deidamia*, with its inner-arched wingshape, can't extend such values of C_p for the same area percentage. The distribution of C_p on the wing at the various α studied is available in Appendix B.

4.3.1. Limiting streamlines in gliding flight

Appendix B reports the velocity limiting streamlines for all the angles of attack studied. These plots show us that for both the wingshapes, whereas the stream pattern on the ventral side is always tidy and hardly influenced by the angle of attack, the flow on the dorsal side for both the species is fully attached only for $\alpha = 2^\circ$, whereas it separates at the leading edge and reattaches later on the surface for $\alpha = 4^\circ$ and $\alpha = 6^\circ$ and turns into a fully separated configuration starting from $\alpha = 8^\circ$.

This considerations help us to understand the trend of the lift-to-drag ratio curves of the two butterflies, which increase to reach their maximum value at $\alpha = 6^\circ$ and then drop as full separation occurs, even though they are not descriptive of the differences between the two species.

4.3.2. Vortex structures on the wing in gliding flight

In Figure 4.9 we use the λ_2 criterion to detect vortex structures surrounding the wing. This parameter is generated by an algorithm which manipulates the velocity

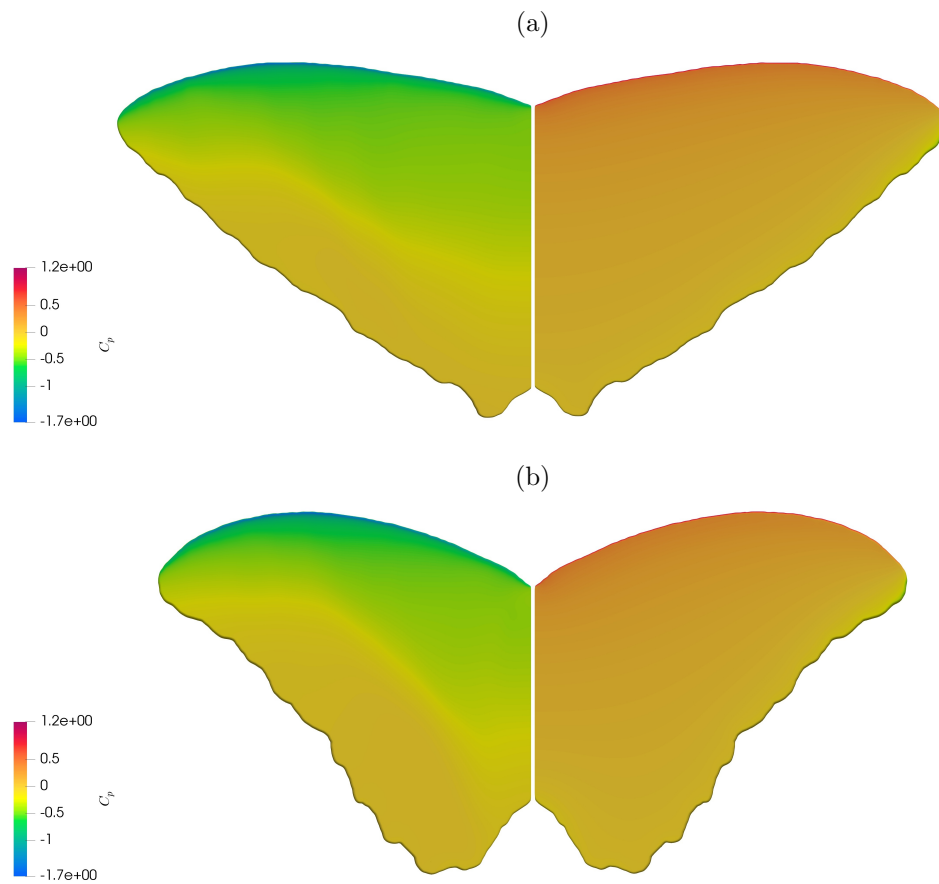


Figure 4.8.: C_p distribution on the wing for the two butterfly species ((a) *Morpho cisseis*, (b) *Morpho deidamia*) tested at 6° angle of attack, which brings the biggest difference in terms of lift-to-drag ratio between the two insects. On the left the dorsal side of the wing, on the right the ventral side.

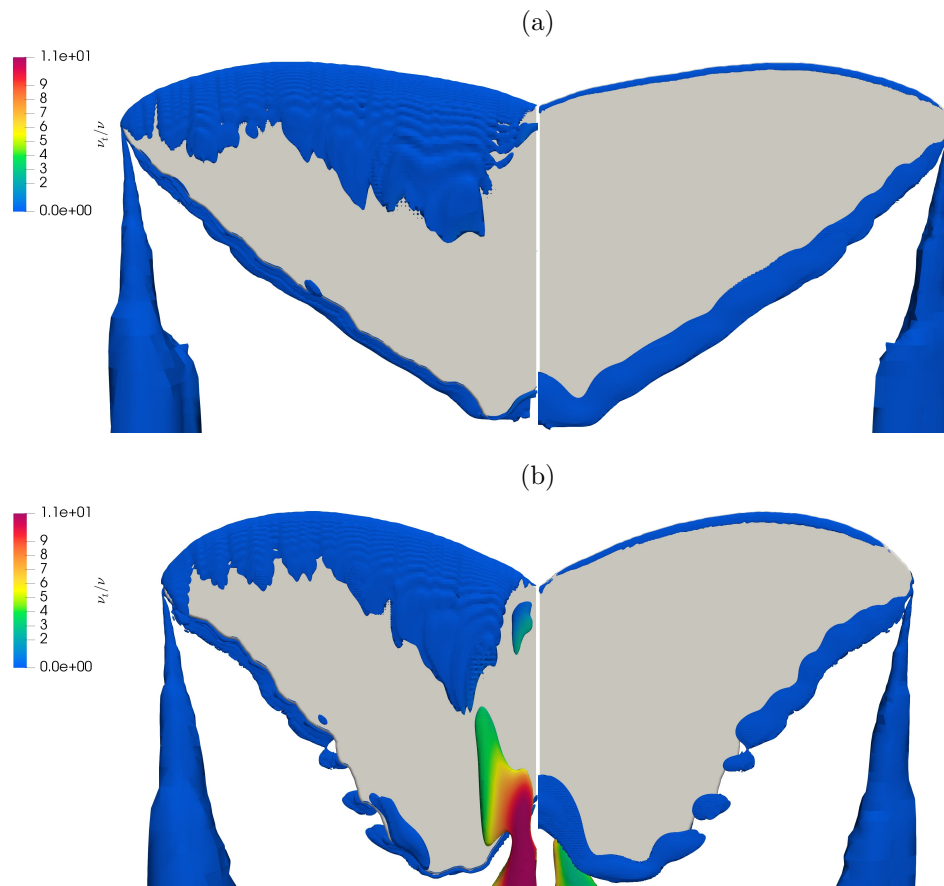


Figure 4.9.: Contours of λ_2 criterion with value 0.1 on the wing coloured with the ν_t/ν ratio for the two butterfly species ((a) *Morpho cisseis*, (b) *Morpho deidamia*) tested at 6° angle of attack, which brings the biggest difference in terms of lift-to-drag ratio between the two insects. On the left the dorsal side of the wing, on the right the ventral side.

vector field to define if a point is part of a vortex core ([17]). The figure shows the contour surface for $\lambda_2=0.1$, coloured with value of ν_t/ν . From these plots it is clearly visible that both the species shed a laminar vortex from the wingtip, but the *deidamia* (Figure 4.9 (b)) also produces a vortex in the rear root of the wing which quickly becomes turbulent. This phenomenon is probably due to the loss in chord length close to the wing root that characterises the *deidamia* wingshape: this loss translates in a reduction of lift production in that area, which, as a consequence, produces a root vortex. Another difference between the two species lies in the vortex structures developing on the lateral edge of the wing, which are smooth and homogeneous for the *cisseis* and snapped and discontinuous for the *deidamia*.

Appendix B gathers the same plots of λ_2 for the various angles of attack studied, which show that the two wings have similar behaviours as we increase the angle of attack, according to the lift-to-drag ratio trend: multiple vortices are released from the side-rear edges in the range of $\alpha = 10^\circ - 12^\circ$; for higher values of α these vortices tend to gather together in a single shed turbulent structure. The vortex released from the wingtip is always visible and mostly characterised by a laminar state.

4.4. Discussion

This chapter underlines some interesting features of the two butterfly species studied and some important differences between them. At the Reynolds number considered (5200) for gliding flight, the two wings have the same stall angle (4°) and experience a separation without reattachment at $\alpha = 8^\circ$; nevertheless, according to the drag and lift coefficients the *Morpho cisseis* produces higher aerodynamic forces. For what concerns flapping flight simulations, using a different Reynolds number for the two different species but the same rotational velocity of $1500^\circ/\text{s}$, the same conclusion can be drawn in terms of force coefficients. Interestingly, if we consider the lift-to-drag ratio, which is commonly used in insect and animal flight studies to evaluate the efficiency and performances of flight ([34, 36, 35]), things go in a different way. In fact, in gliding flight the *cisseis* boasts higher L/D values for all the angles of attack studied, reaching a maximum of around 10% better performances with respect to the *deidamia* at $\alpha = 6^\circ$. On the contrary, in flapping flight condition the L/D of the two species, except for α in the range 15° - 21° , is almost identical. With the goal of explaining the difference in performances in glide conditions, we looked at the C_p distribution on the two wings for $\alpha = 6^\circ$, noticing that the inner-arched lateral shape of the *deidamia* could play a role in not letting the low pressure regions extend along the wing as much as it happens with the *cisseis* (Figure 4.8); moreover, Figure 4.9 underlines that the loss in chord length close to the wing root, which characterises the *deidamia*, triggers a turbulent vortex on the dorsal side of the insect which can also represent a source of performance loss. The latter phenomenon has been observed in previous studies carried out on bats and birds ([36]), allowing us to roughly link the aerodynamic relationship between *Morpho cisseis* and *Morpho deidamia* to the one between birds and bats respectively. This work shows thus that at dynamical

conditions typical of *Morpho butterflies*, the shape of the wing plays a fundamental role in the performances of gliding flight but not in the ones of flapping flight. This matches with the data provided by [22], confirming the gliding specialist profile of the *cisseis* and explaining why it is able to perform longer gliding flight phases at higher altitudes.

5. Conclusions and Final Remarks

In this thesis we approach the study of *Morpho* butterfly aerodynamics by means of computational fluid dynamics. Firstly, we investigate the optimal criteria to model the morphology and physics of the insects, defining important parameters for the discretisation of the geometries and the setups of the simulations. As a second step, we reproduce gliding flight conditions using different turbulence models. These results are compared with experimental results pulled out from recorded flight kinematics using inverse dynamics. Then we reproduce both gliding and flapping flight for two different *Morpho* species at various angles of attack. The reliability of the results is ensured by uncertainty estimations and sensitivity studies.

The results obtained allow us to answer to the questions issued in the Introduction, as discussed next.

5.1. Which CFD model should we use to reproduce the flight of *Morpho* butterflies?

If we are only looking at the closeness of the simulation to the experimental results, the answer is easy: PANS model performs best in this aspect: in the gliding flight study case we focused on, looking at the global efficiency parameter lift-to-drag ratio, this model provides a result 20% different from the experimental one, whereas the others differ of about 30% to 43%. Moreover, among the models used, PANS is the only one able to catch the unsteady nature of the flow, in contrast with the others, converging to a steady result. Nevertheless, PANS demands high computational costs, not affordable for a wide range of study cases. Among the RANS models, SST $k - \omega$ proved to be the most reliable, providing results not far from PANS values at a much lower computational cost.

It is important to underline that all the numerical simulations overestimate the

values of drag and lift forces: reasons for this inconsistency could lie in the modelling assumptions and/or in uncertainties in the experimental data, which are unknown.

5.2. Do different *Morpho* species have different aerodynamic performances?

The present work limits its focus on the two species *cisseis* and *deidamia*, which belong respectively to the canopy species group and the understory species group. The results of the simulations highlight some differences between the two specimens, showing how the *cisseis* boasts higher performances in gliding flight, whereas the two butterflies have equal performances in flapping flight. This result is in accordance with the flying behaviour adopted by the two species, as reported in [22].

5.3. Future work

Ranging from defining an approach to proposing meaningful results about the flying behaviour and aerodynamic features of the two species studied, this work can represent a solid starting point for a complete study of *Morpho* butterflies and other insects operating at similar Reynolds numbers. Nevertheless, some aspects can be improved to increment validity and precision of the results. Important assumptions have been made while modelling the geometry of the insect: it would be interesting to investigate the role of the body in the production of aerodynamic forces and definition of the flow pattern. Moreover, it would be of great interest to perform PANS simulations for different setups, both in gliding and flapping flight, to gain precise insights of the flow behaviour in several conditions. For time and computational power constrictions, not only the number of PANS simulations but also the number of species studied was limited: [22] suggests that other flying behaviour are adopted by different species, representing a further object of interest. As a last consideration, the inference of other parameters -like gliding velocity- should be studied to give more comprehensive answers about the different behaviours of the various species.

A. Support Plots for Chapter 3

A.1. Numerical uncertainties

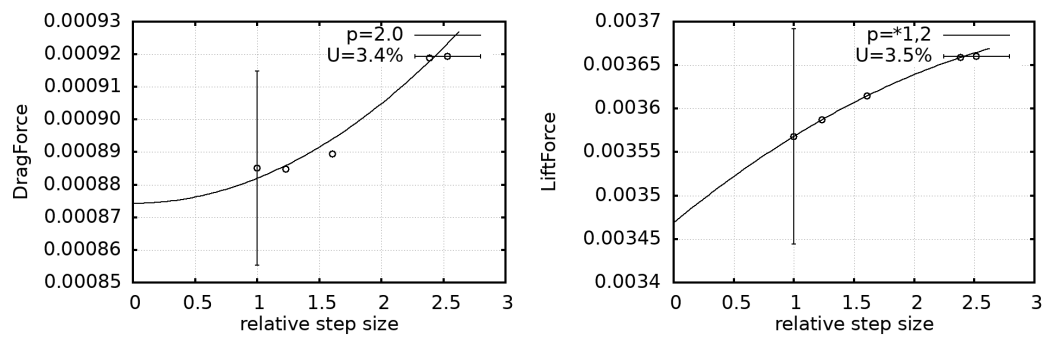


Figure A.1.: SST $k - \omega$ model: numerical uncertainty.

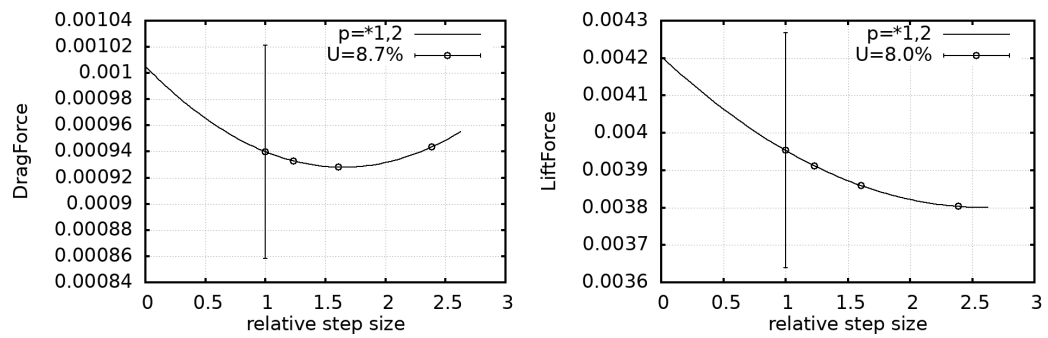


Figure A.2.: Spalart-Allmaras model: numerical uncertainty.

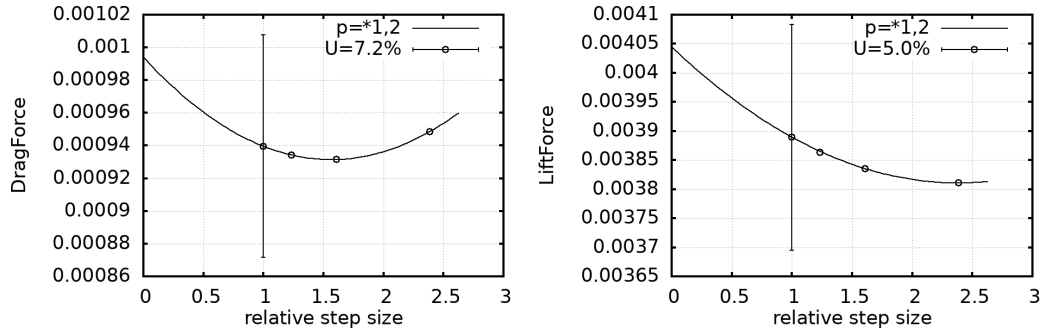


Figure A.3.: SST $\gamma - Re_{\theta} \nu_t/\nu = 2.5$ model: numerical uncertainty.

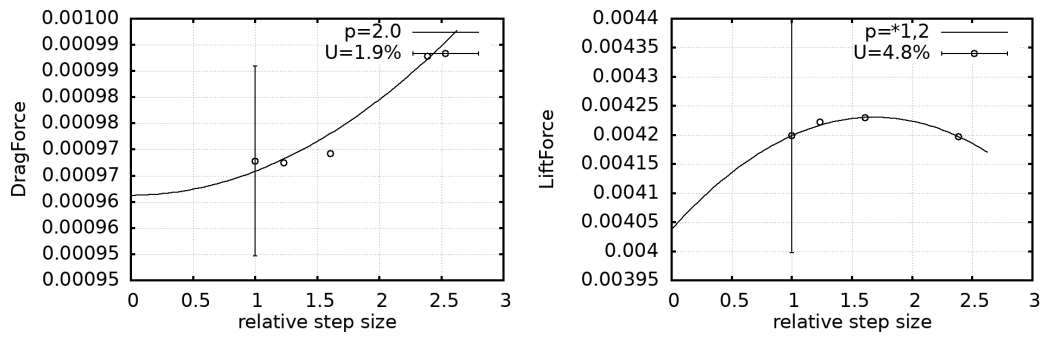


Figure A.4.: SST $\gamma - Re_{\theta} \nu_t/\nu = 10$ model: numerical uncertainty.

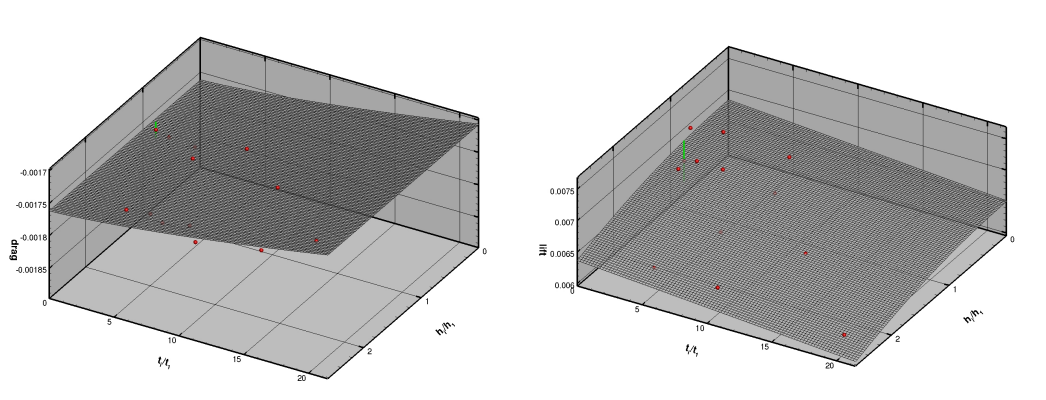


Figure A.5.: PANS model: numerical uncertainty. Here the results are interpolated with a surface dependent on the space and time discretisation; for the finest grid and timestep (red dot highlighted by green bar) drag force has an uncertainty of 0.723% and lift of 4.83%.

B. Support Material for Chapter 4

B.1. Numerical uncertainties

Figure B.1.: *Morpho cisseis*: numerical uncertainty of drag and lift forces at 2° angle of attack.

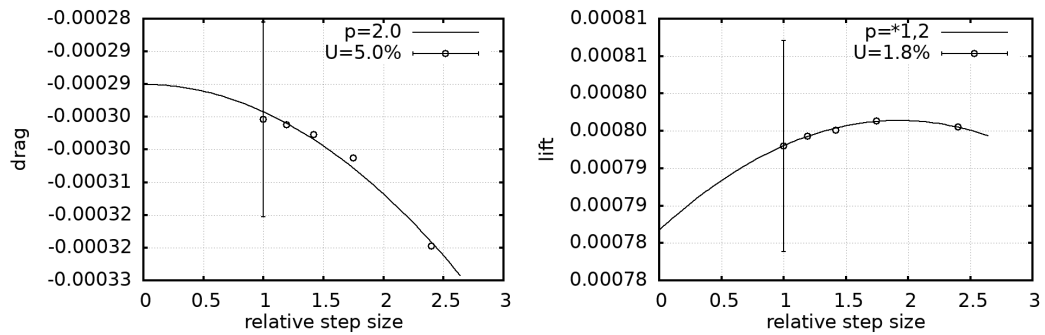


Figure B.2.: *Morpho cisseis*: numerical uncertainty of drag and lift forces at 4° angle of attack.

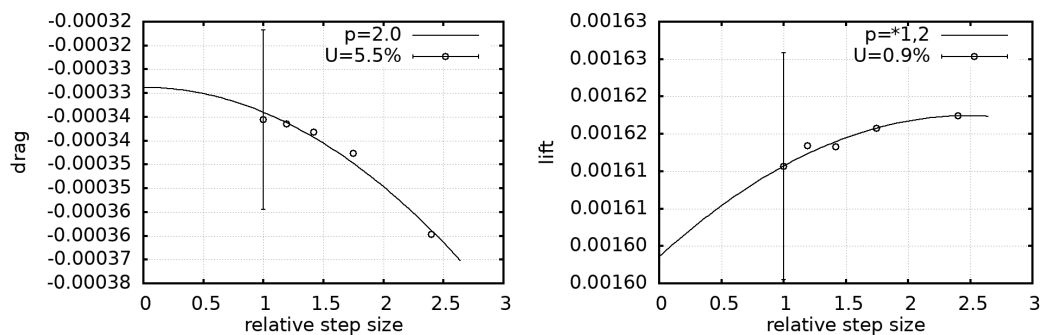


Figure B.3.: *Morpho cisseis*: numerical uncertainty of drag and lift forces at 6° angle of attack.

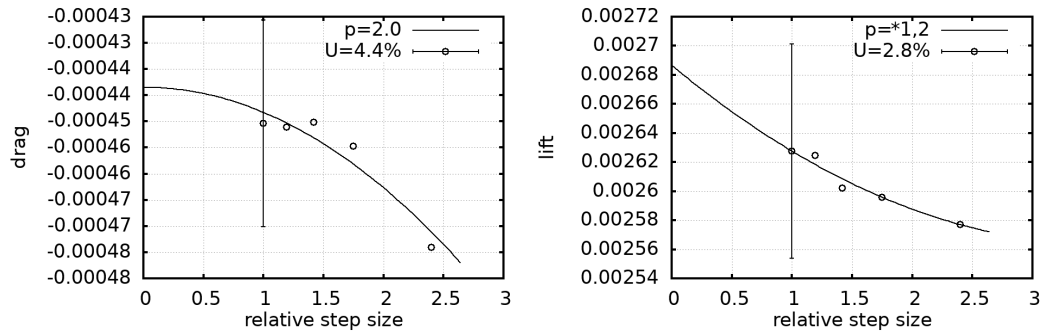


Figure B.4.: *Morpho cisseis*: numerical uncertainty of drag and lift forces at 8° angle of attack.

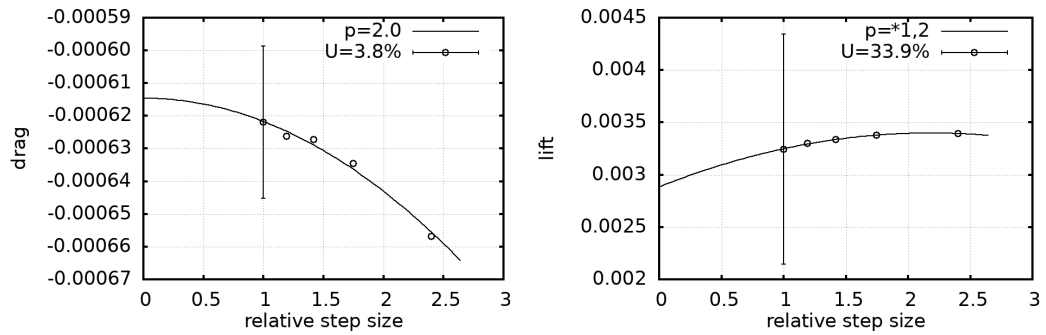


Figure B.5.: *Morpho cisseis*: numerical uncertainty of drag and lift forces at 10° angle of attack.

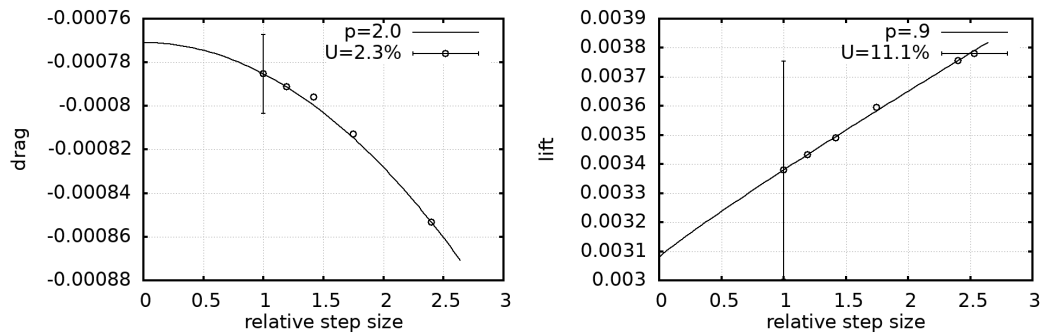


Figure B.6.: *Morpho cisseis*: numerical uncertainty of drag and lift forces at 12° angle of attack.

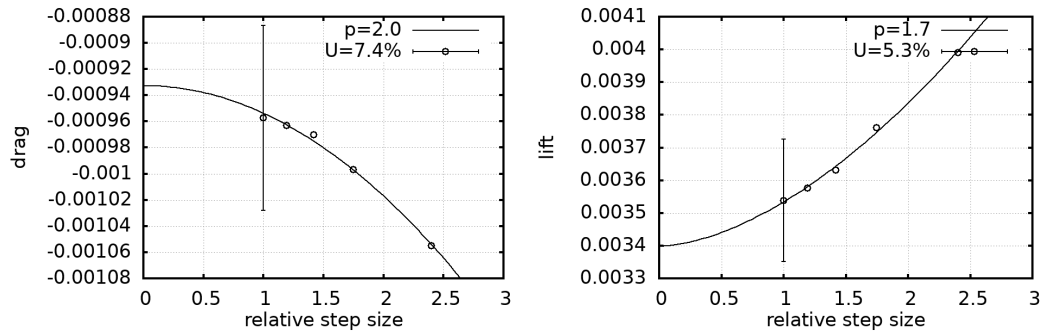


Figure B.7.: *Morpho cisseis*: numerical uncertainty of drag and lift forces at 14° angle of attack.

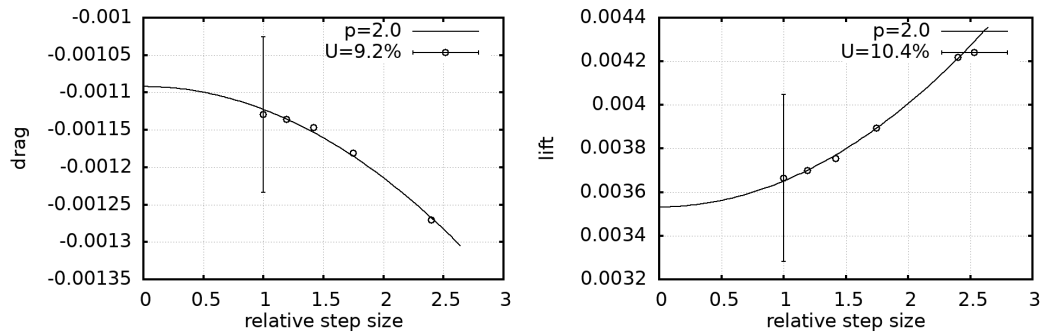


Figure B.8.: *Morpho cisseis*: numerical uncertainty of drag and lift forces at 16° angle of attack.

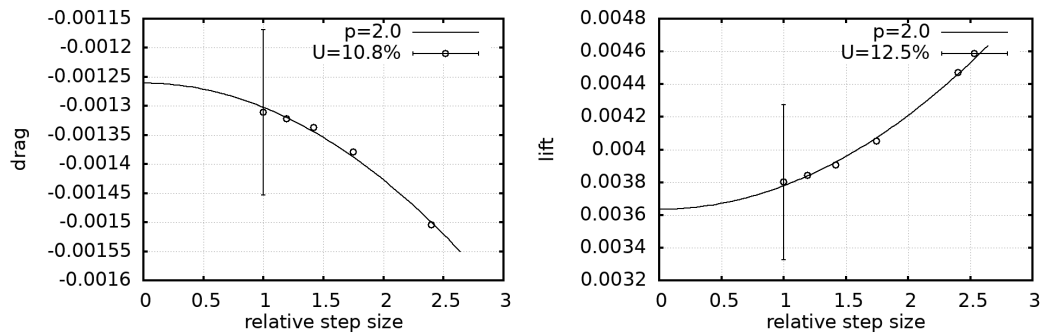


Figure B.9.: *Morpho cisseis*: numerical uncertainty of drag and lift forces at 18° angle of attack.

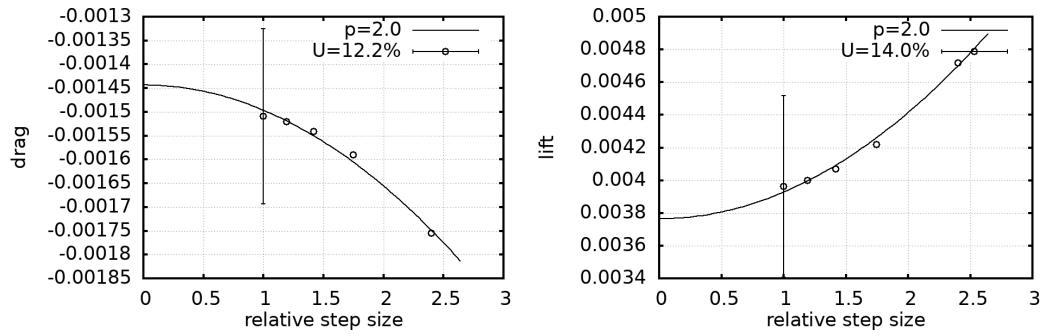


Figure B.10.: *Morpho cisseis*: numerical uncertainty of drag and lift forces at 20° angle of attack.

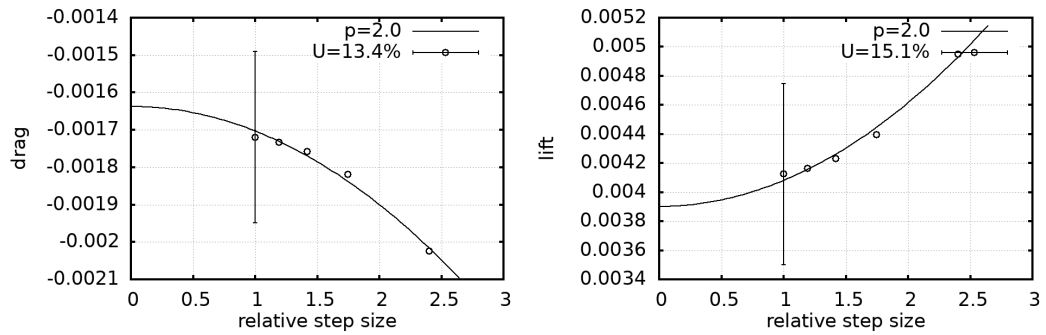


Figure B.11.: *Morpho deidamia*: numerical uncertainty of drag and lift forces at 2° angle of attack.

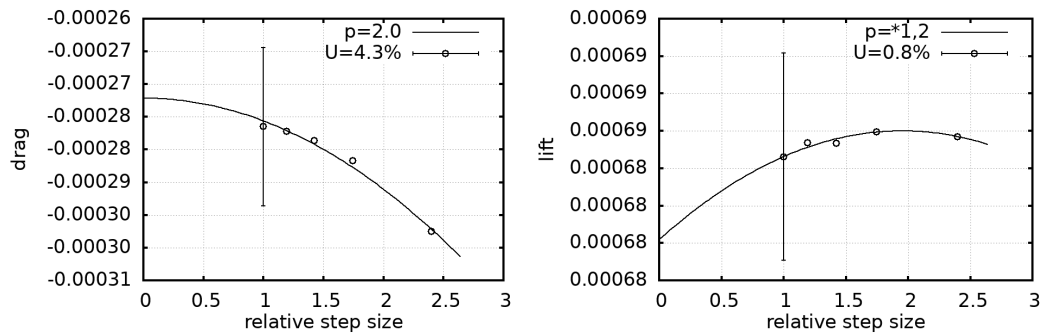


Figure B.12.: *Morpho deidamia*: numerical uncertainty of drag and lift forces at 4°

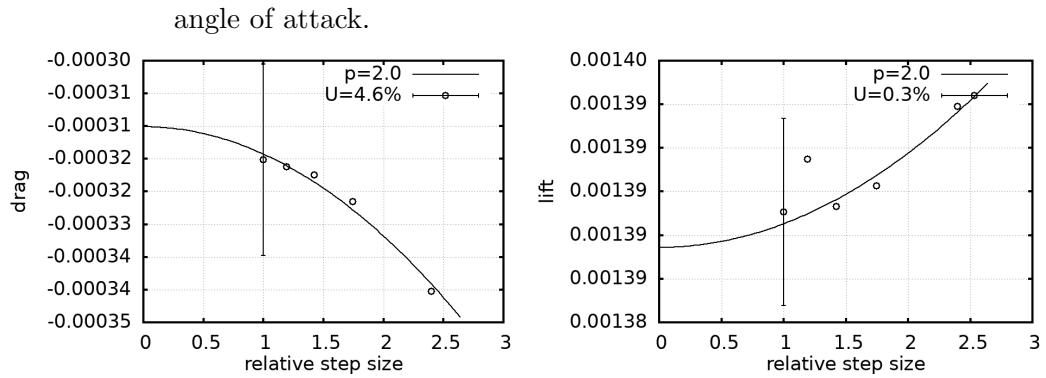


Figure B.13.: *Morpho deidamia*: numerical uncertainty of drag and lift forces at 6°

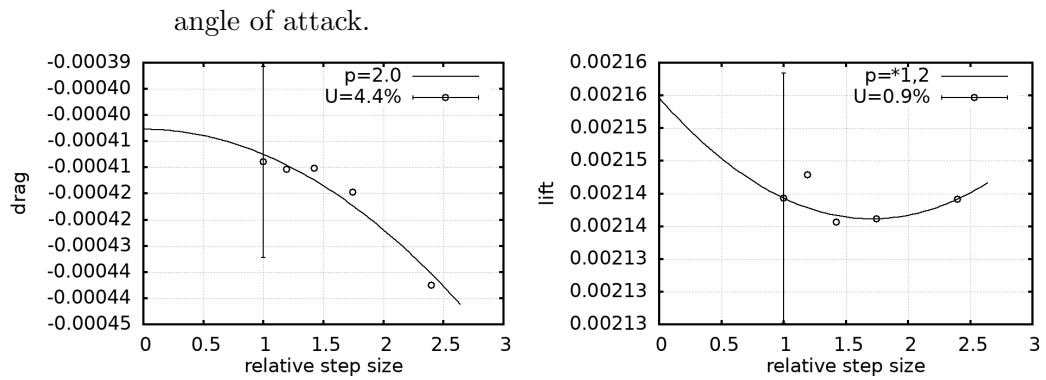


Figure B.14.: *Morpho deidamia*: numerical uncertainty of drag and lift forces at 8°

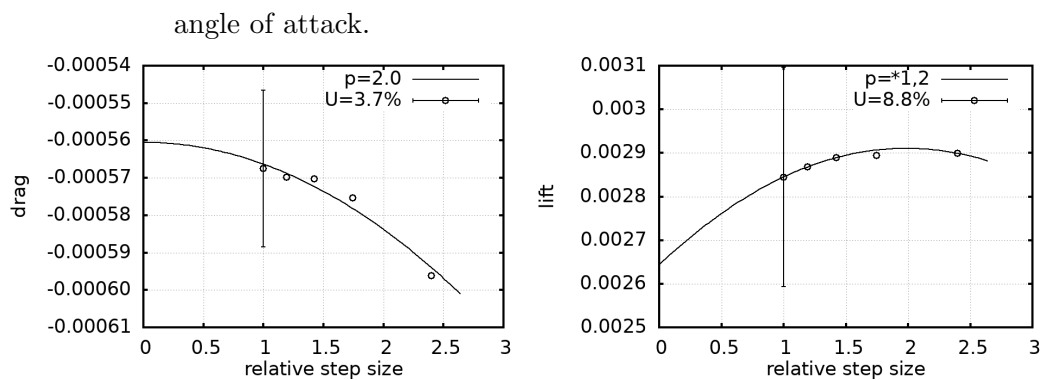


Figure B.15.: *Morpho deidamia*: numerical uncertainty of drag and lift forces at 10° angle of attack.

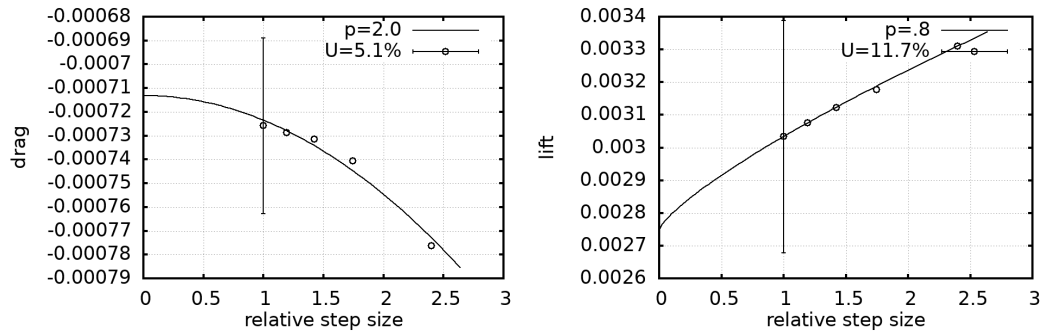


Figure B.16.: *Morpho deidamia*: numerical uncertainty of drag and lift forces at 12° angle of attack.

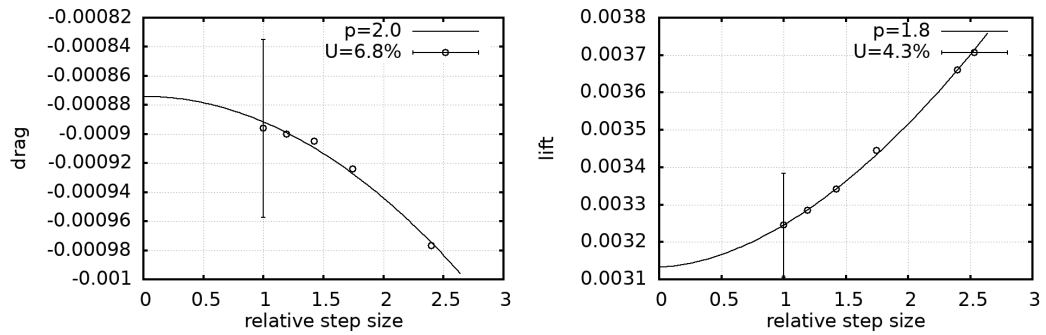


Figure B.17.: *Morpho deidamia*: numerical uncertainty of drag and lift forces at 14° angle of attack.

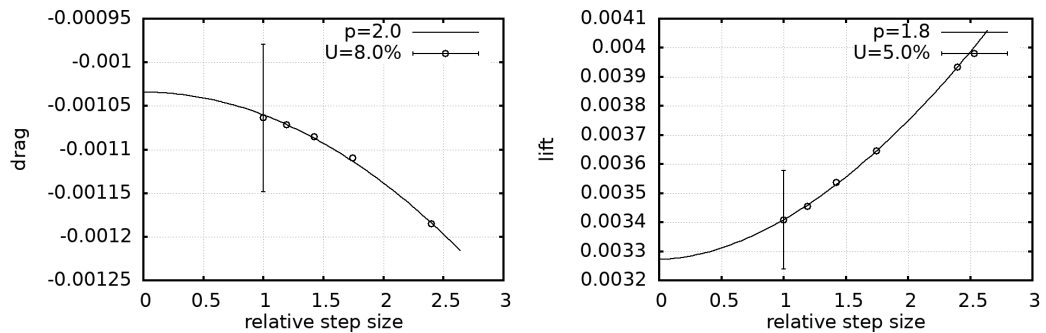


Figure B.18.: *Morpho deidamia*: numerical uncertainty of drag and lift forces at 16° angle of attack.

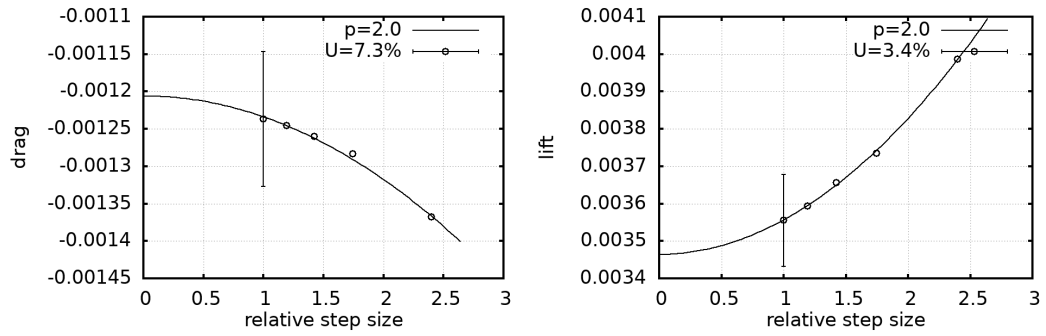


Figure B.19.: *Morpho deidamia*: numerical uncertainty of drag and lift forces at 18° angle of attack.

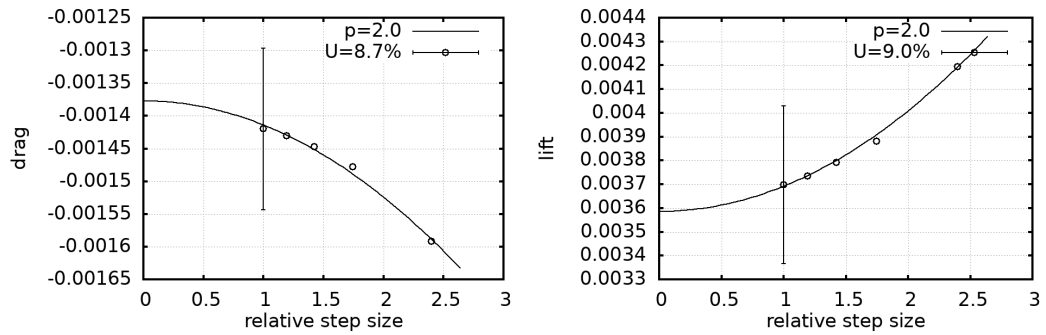


Figure B.20.: *Morpho deidamia*: numerical uncertainty of drag and lift forces at 20° angle of attack.

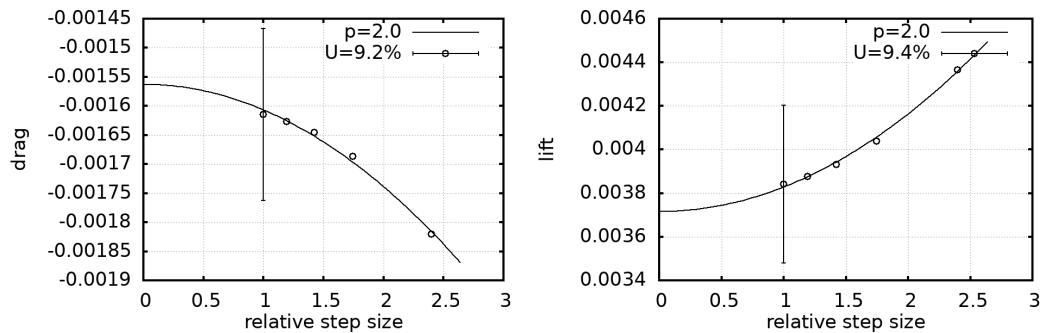


Table B.1.: *Morpho cisseis*, gliding flight: resume of grid specifications.

<i>Morpho cisseis</i> - gliding grids resume												
y+												
grid	n° cells	AoA 2°	AoA 4°	AoA 6°	AoA 8°	AoA 10°	AoA 12°	AoA 14°	AoA 16°	AoA 18°	AoA 20°	
0	698804	7.336E-01	7.339E-01	7.345E-01	7.347E-01	7.345E-01	7.342E-01	7.336E-01	7.337E-01	7.345E-01	7.362E-01	
1	1810196	5.851E-01	5.857E-01	5.859E-01	5.866E-01	5.873E-01	5.877E-01	5.884E-01	5.895E-01	5.905E-01	5.915E-01	
2	3377716	4.948E-01	4.949E-01	4.952E-01	4.950E-01	4.953E-01	4.970E-01	4.960E-01	4.965E-01	4.968E-01	4.974E-01	
3	5715510	4.318E-01	4.320E-01	4.319E-01	4.320E-01	4.326E-01	4.332E-01	4.335E-01	4.336E-01	4.342E-01	4.352E-01	
4	9658292	3.846E-01	3.848E-01	3.847E-01	3.849E-01	3.851E-01	3.855E-01	3.853E-01	3.865E-01	3.856E-01	3.860E-01	

Table B.2.: *Morpho deidamia*, gliding flight: resume of grid specifications.

<i>Morpho deidamia</i> - gliding grids resume												
y+												
grid	n° cells	AoA 2°	AoA 4°	AoA 6°	AoA 8°	AoA 10°	AoA 12°	AoA 14°	AoA 16°	AoA 18°	AoA 20°	
0	481503	8.175E-01	8.170E-01	8.177E-01	8.184E-01	8.189E-01	8.189E-01	8.188E-01	8.194E-01	8.205E-01	8.223E-01	
1	1249733	6.516E-01	6.518E-01	6.521E-01	6.520E-01	6.530E-01	6.536E-01	6.538E-01	6.536E-01	6.538E-01	6.543E-01	
2	2312933	5.507E-01	5.508E-01	5.508E-01	5.507E-01	5.510E-01	5.513E-01	5.517E-01	5.522E-01	5.527E-01	5.532E-01	
3	3911936	4.806E-01	4.807E-01	4.806E-01	4.803E-01	4.803E-01	4.806E-01	4.806E-01	4.805E-01	4.808E-01	4.806E-01	
4	6643215	4.282E-01	4.283E-01	4.283E-01	4.287E-01	4.291E-01	4.294E-01	4.295E-01	4.300E-01	4.305E-01	4.311E-01	

Table B.3.: *Morpho cisseis*, flapping flight: resume of grid specifications.

<i>Morpho cisseis</i> - flapping grids resume											
y^+											
grid	n° cells	AoA 15°	AoA 17°	AoA 19°	AoA 21°	AoA 23°	AoA 25°	AoA 27°	AoA 29°	AoA 31°	AoA°
0	1203569	8.922E-01	8.900E-01	8.873E-01	8.853E-01	8.836E-01	8.819E-01	8.812E-01	8.802E-01	8.794E-01	8.782E-01
<i>Morpho cisseis</i> - gliding grids resume											
y^+											
grid	n° cells	AoA 35°	AoA 37°	AoA 39°	AoA 41°	AoA 43°	AoA 45°	AoA 47°	AoA 49°	AoA 51°	AoA 53°
0	1203569	8.769E-01	8.762E-01	8.750E-01	8.736E-01	8.729E-01	8.732E-01	8.736E-01	8.740E-01	8.742E-01	8.743E-01
<i>Morpho cisseis</i> - gliding grids resume											
y^+											
grid	n° cells	AoA 55°	AoA 57°	AoA 59°	AoA 61°	AoA 63°	AoA 65°	AoA 67°	AoA 69°	AoA 71°	AoA 73°
0	1203569	8.752E-01	8.755E-01	8.755E-01	8.751E-01	8.742E-01	8.732E-01	8.735E-01	8.736E-01	8.735E-01	8.731E-01

Table B.4.: *Morpho deidamia*, flapping flight: resume of grid specifications.

<i>Morpho deidamia</i> - gliding grids resume											
y^+											
grid	n° cells	AoA 15°	AoA 17°	AoA 19°	AoA 21°	AoA 23°	AoA 25°	AoA 27°	AoA 29°	AoA 31°	AoA°
0	859001	7.709E-01	7.709E-01	7.709E-01	7.709E-01	7.708E-01	7.708E-01	7.707E-01	7.707E-01	7.707E-01	7.708E-01
<i>Morpho deidamia</i> - gliding grids resume											
y^+											
grid	n° cells	AoA 35°	AoA 37°	AoA 39°	AoA 41°	AoA 43°	AoA 45°	AoA 47°	AoA 49°	AoA 51°	AoA 53°
0	859001	7.708E-01	7.709E-01	7.709E-01	7.710E-01	7.710E-01	7.711E-01	7.711E-01	7.712E-01	7.712E-01	7.713E-01
<i>Morpho deidamia</i> - gliding grids resume											
y^+											
grid	n° cells	AoA 55°	AoA 57°	AoA 59°	AoA 61°	AoA 63°	AoA 65°	AoA 67°	AoA 69°	AoA 71°	AoA 73°
0	859001	7.714E-01	7.714E-01	7.715E-01	7.715E-01	7.716E-01	7.716E-01	7.716E-01	7.717E-01	7.717E-01	7.717E-01

Table B.5.: *Morpho cisseis*, gliding flight: L^2 norm of variation of aerodynamic forces for the last 2000 iterations. The meaning of this values is explained in Subsection 4.2.1.

		L_2 norm of drag force variation for the last 2000 iterations [N]												
grid	AoA 2 °	AoA 4 °	AoA 6 °	AoA 8 °	AoA 10 °	AoA 12 °	AoA 14 °	AoA 16 °	AoA 18 °	AoA 20 °				
0	4.536E-18	0.000E+00	1.361E-17	1.814E-17	1.814E-17	1.814E-17	4.796E-08	1.887E-03	3.515E-03	4.450E-03				
1	4.536E-18	9.071E-18	1.361E-17	1.814E-17	0.000E+00	4.717E-09	1.814E-17	1.814E-17	3.628E-17	1.017E-08				
2	9.071E-18	0.000E+00	0.000E+00	9.071E-18	9.071E-18	1.814E-17	3.628E-17	0.000E+00	5.443E-17	0.000E+00				
3	4.536E-18	0.000E+00	1.814E-17	9.071E-18	9.071E-18	0.000E+00	1.814E-17	3.628E-17	1.814E-17	0.000E+00				
4	0.000E+00	0.000E+00	9.071E-18	0.000E+00	2.721E-17	2.721E-17	1.814E-17	1.814E-17	3.628E-17	5.443E-17				

		L_2 norm of lift force variation for the last 2000 iterations [N]												
grid	AoA 2 °	AoA 4 °	AoA 6 °	AoA 8 °	AoA 10 °	AoA 12 °	AoA 14 °	AoA 16 °	AoA 18 °	AoA 20 °				
0	0.000E+00	1.814E-17	0.000E+00	3.628E-17	7.257E-17	7.257E-17	2.002E-07	7.537E-03	1.233E-02	1.380E-02				
1	9.071E-18	3.628E-17	3.628E-17	1.089E-16	3.628E-17	2.858E-08	8.670E-09	7.257E-17	0.000E+00	2.690E-08				
2	1.814E-17	1.814E-17	3.628E-17	7.257E-17	3.628E-17	3.628E-17	1.451E-16	1.089E-16	7.257E-17	7.257E-17				
3	9.071E-18	5.443E-17	0.000E+00	0.000E+00	7.257E-17	3.628E-17	7.257E-17	0.000E+00	1.451E-16	7.257E-17				
4	1.814E-17	0.000E+00	0.000E+00	3.628E-17	3.628E-17	3.628E-17	1.089E-16	3.628E-17	0.000E+00	1.451E-16				

Table B.6.: *Morpho deidamia*, gliding flight: L_2 norm of variation of aerodynamic forces for the last 2000 iterations. The meaning of this values is explained in Subsection 4.2.1.

		L ₂ norm of drag force variation for the last 2000 iterations [N]												
grid	AoA 2 °	AoA 4 °	AoA 6 °	AoA 8 °	AoA 10 °	AoA 12 °	AoA 14 °	AoA 16 °	AoA 18 °	AoA 20 °				
0	4.849E-18	9.697E-18	9.697E-18	1.098E-05	2.479E-04	1.017E-03	2.067E-03	0.000E+00	3.879E-17	5.818E-17				
1	4.849E-18	0.000E+00	0.000E+00	2.845E-08	3.448E-04	8.876E-04	1.526E-03	2.146E-07	0.000E+00	3.879E-17				
2	4.849E-18	4.849E-18	1.455E-17	9.697E-18	2.204E-08	5.346E-04	1.191E-03	1.312E-05	3.879E-17	7.758E-17				
3	4.849E-18	9.697E-18	9.697E-18	0.000E+00	9.697E-18	5.627E-09	2.892E-04	4.194E-06	1.562E-08	1.939E-17				
4	4.849E-18	4.849E-18	4.849E-18	9.106E-09	1.939E-17	2.909E-17	3.879E-17	1.507E-08	3.879E-17	3.879E-17				

		L ₂ norm of lift force variation for the last 2000 iterations [N]												
grid	AoA 2 °	AoA 4 °	AoA 6 °	AoA 8 °	AoA 10 °	AoA 12 °	AoA 14 °	AoA 16 °	AoA 18 °	AoA 20 °				
0	1.94E-17	0.00E+00	0.00E+00	1.08E-04	1.85E-03	5.61E-03	9.28E-03	7.76E-17	7.76E-17	1.55E-16				
1	1.94E-17	0.00E+00	0.00E+00	2.46E-07	2.31E-03	4.84E-03	6.84E-03	7.91E-07	3.88E-17	7.76E-17				
2	9.70E-18	1.94E-17	7.76E-17	3.88E-17	1.40E-07	2.77E-03	5.19E-03	4.88E-05	3.88E-17	7.76E-17				
3	0.00E+00	0.00E+00	3.88E-17	3.88E-17	3.36E-08	3.17E-08	1.24E-03	1.56E-05	2.65E-08	7.76E-17				
4	9.70E-18	1.94E-17	0.00E+00	9.58E-08	3.88E-17	0.00E+00	3.88E-17	1.71E-08	7.76E-17	3.88E-17				

α [°]	L/D % uncertainty	
	<i>cisseis</i>	<i>deidamia</i>
2	4.7	4.1
4	5.1	4.3
6	5.2	4.4
8	14.5	9.1
10	27.3	11.5
12	17.1	9.8
14	4.9	6.9
16	2.1	4.6
18	1.5	2.4
20	1.4	2

Table B.7.: Values of numerical uncertainty for lift-to-drag ratio in gliding flight simulations.

B.2. Morpho cisseis: pressure coefficient on the wing

Figure B.21.: *Morpho cisseis*: pressure coefficient on the wing at 2° angle of attack. On the left the dorsal side, on the right the ventral side of the wing.

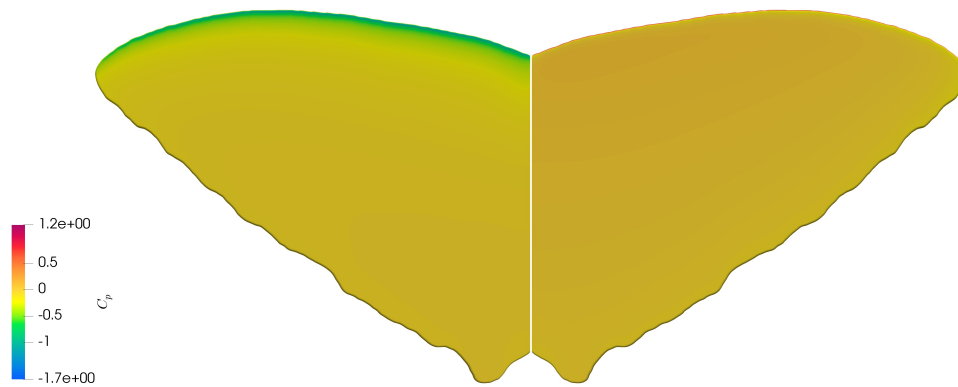


Figure B.22.: *Morpho cisseis*: pressure coefficient on the wing at 4° angle of attack.

On the left the dorsal side, on the right the ventral side of the wing.

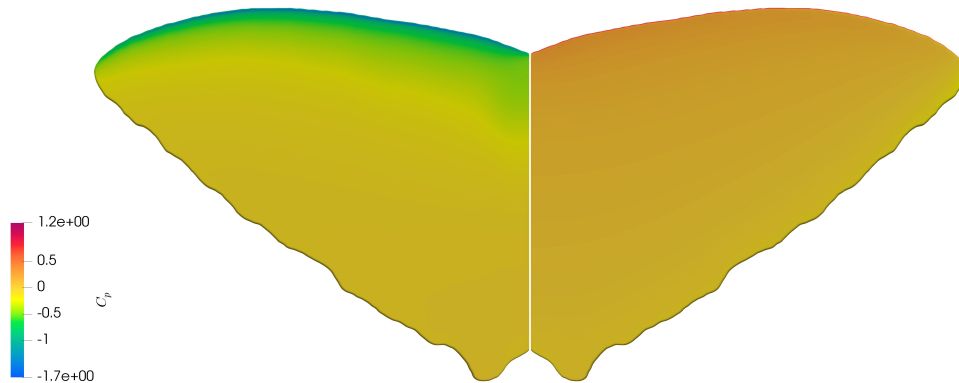


Figure B.23.: *Morpho cisseis*: pressure coefficient on the wing at 6° angle of attack.

On the left the dorsal side, on the right the ventral side of the wing.

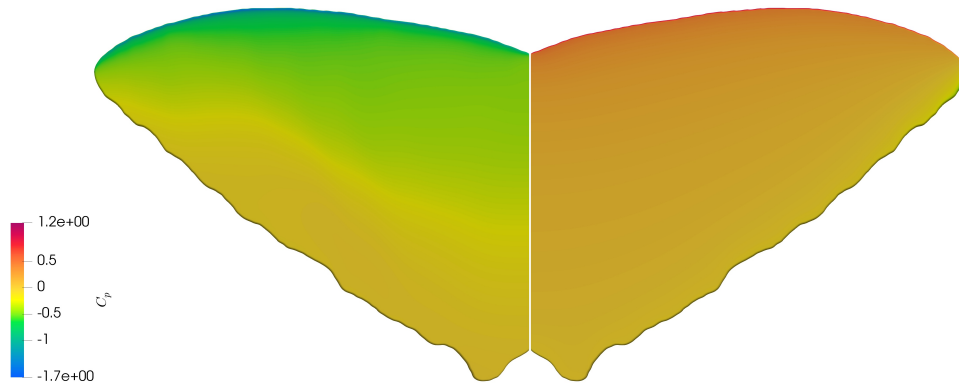


Figure B.24.: *Morpho cisseis*: pressure coefficient on the wing at 8° angle of attack.

On the left the dorsal side, on the right the ventral side of the wing.

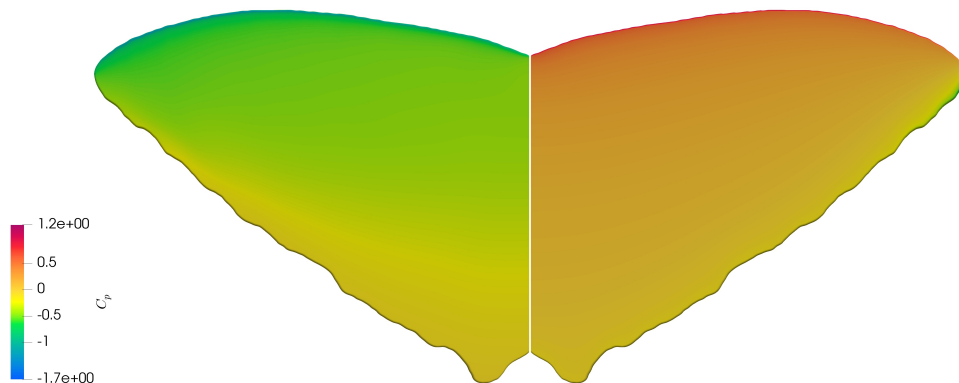


Figure B.25.: *Morpho cisseis*: pressure coefficient on the wing at 10° angle of attack.

On the left the dorsal side, on the right the ventral side of the wing.

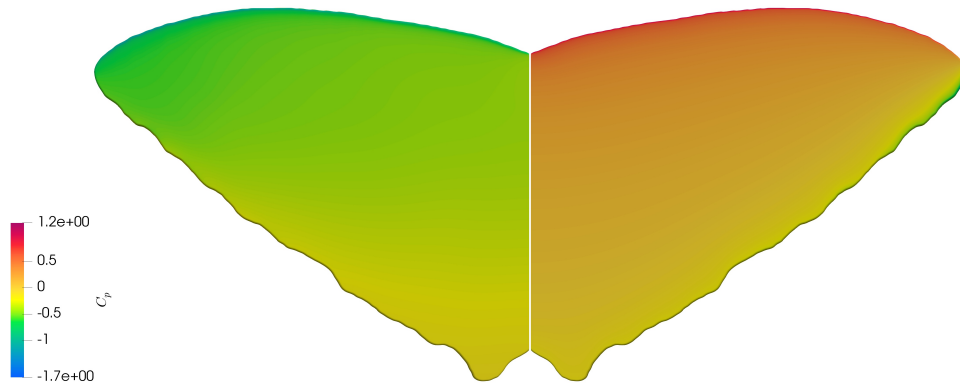


Figure B.26.: *Morpho cisseis*: pressure coefficient on the wing at 12° angle of attack.

On the left the dorsal side, on the right the ventral side of the wing.

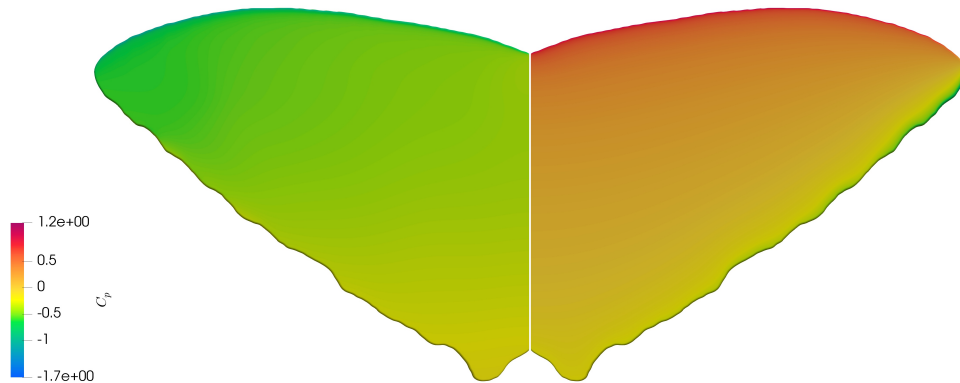


Figure B.27.: *Morpho cisseis*: pressure coefficient on the wing at 14° angle of attack.

On the left the dorsal side, on the right the ventral side of the wing.



Figure B.28.: *Morpho cisseis*: pressure coefficient on the wing at 16° angle of attack.

On the left the dorsal side, on the right the ventral side of the wing.

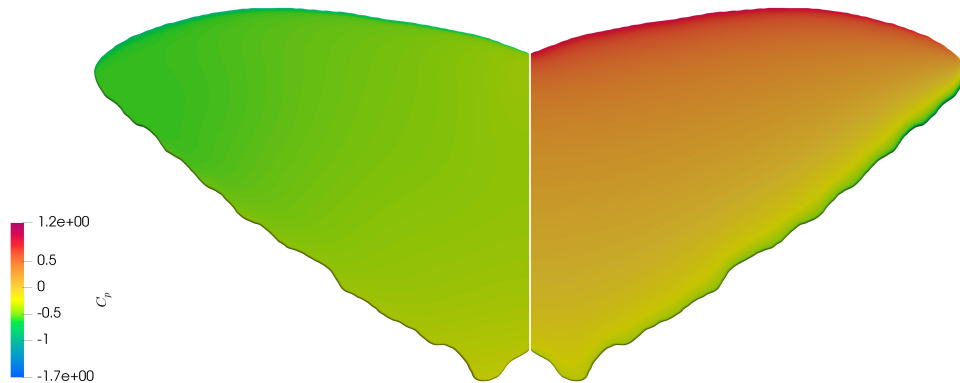


Figure B.29.: *Morpho cisseis*: pressure coefficient on the wing at 18° angle of attack.

On the left the dorsal side, on the right the ventral side of the wing.



Figure B.30.: *Morpho cisseis*: pressure coefficient on the wing at 20° angle of attack.

On the left the dorsal side, on the right the ventral side of the wing.



B.3. *Morpho deidamia*: pressure coefficient on the wing

Figure B.31.: *Morpho deidamia*: pressure coefficient on the wing at 2° angle of attack. On the left the dorsal side, on the right the ventral side of the wing.

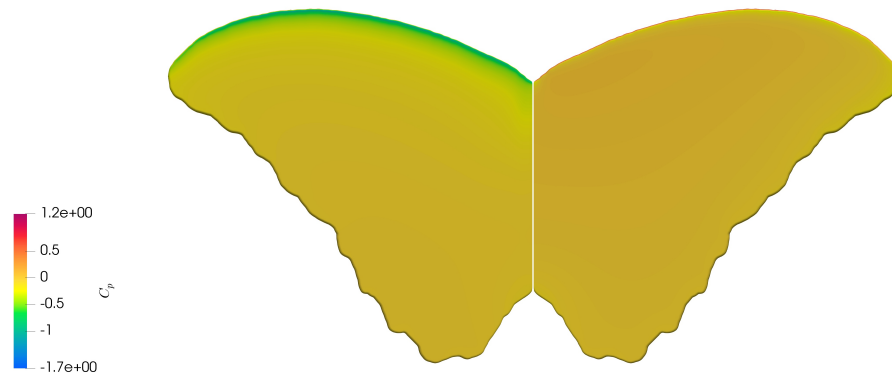


Figure B.32.: *Morpho deidamia*: pressure coefficient on the wing at 4° angle of attack. On the left the dorsal side, on the right the ventral side of the wing.

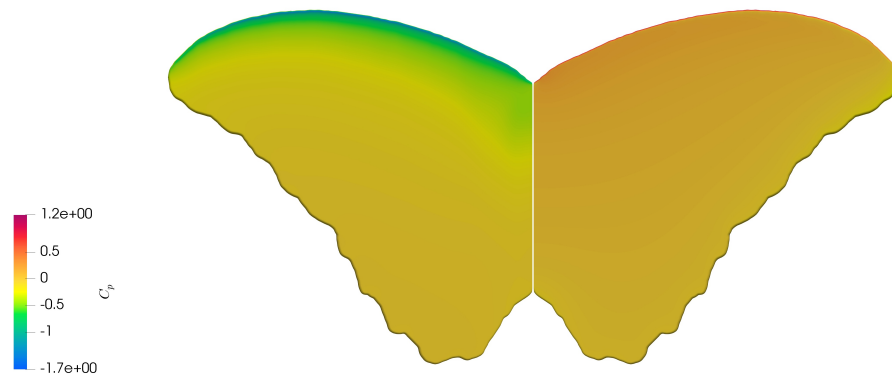


Figure B.33.: *Morpho deidamia*: pressure coefficient on the wing at 6° angle of attack. On the left the dorsal side, on the right the ventral side of the wing.

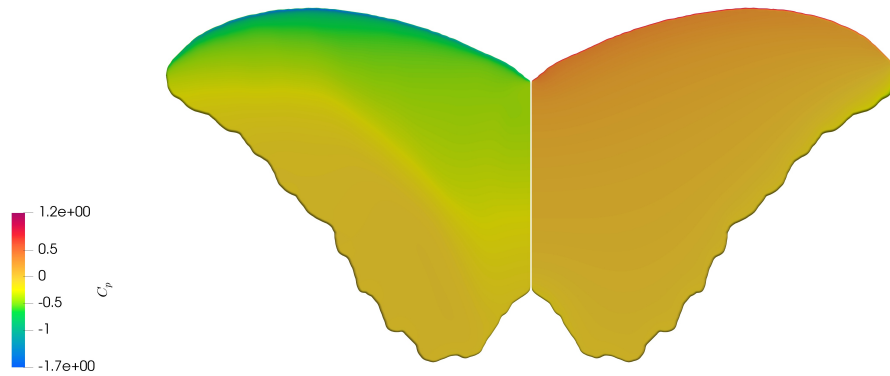


Figure B.34.: *Morpho deidamia*: pressure coefficient on the wing at 8° angle of attack. On the left the dorsal side, on the right the ventral side of the wing.

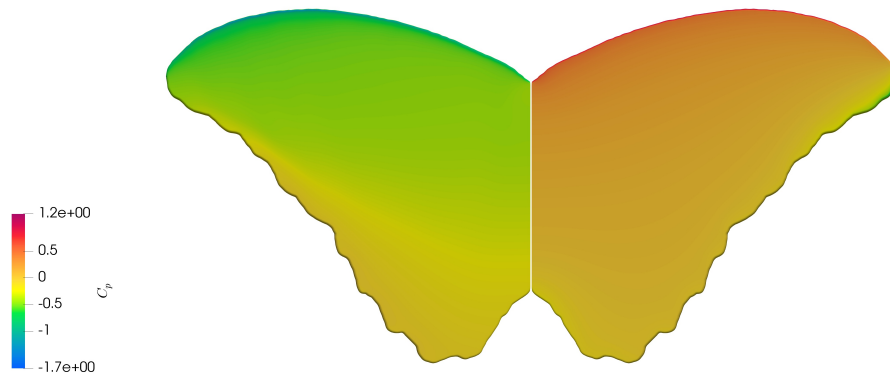


Figure B.35.: *Morpho deidamia*: pressure coefficient on the wing at 10° angle of attack. On the left the dorsal side, on the right the ventral side of the wing.

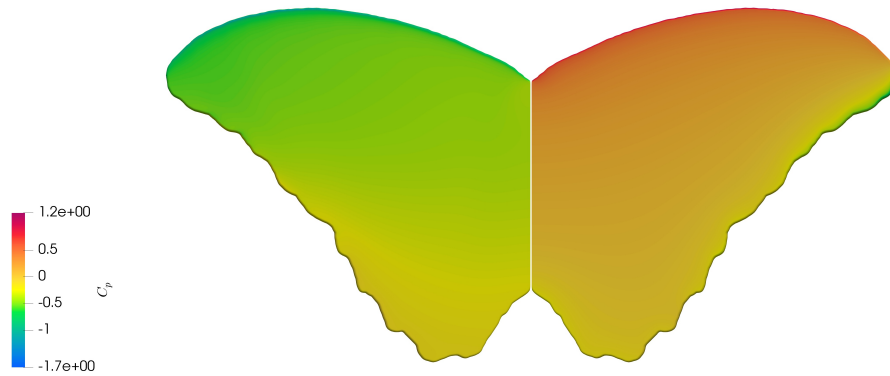


Figure B.36.: *Morpho deidamia*: pressure coefficient on the wing at 12° angle of attack. On the left the dorsal side, on the right the ventral side of the wing.

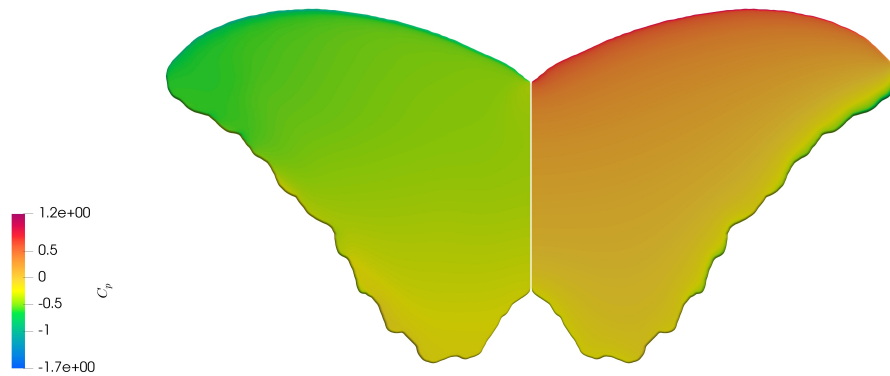


Figure B.37.: *Morpho deidamia*: pressure coefficient on the wing at 14° angle of attack. On the left the dorsal side, on the right the ventral side of the wing.



Figure B.38.: *Morpho deidamia*: pressure coefficient on the wing at 16° angle of attack. On the left the dorsal side, on the right the ventral side of the wing.



Figure B.39.: *Morpho deidamia*: pressure coefficient on the wing at 18° angle of attack. On the left the dorsal side, on the right the ventral side of the wing.

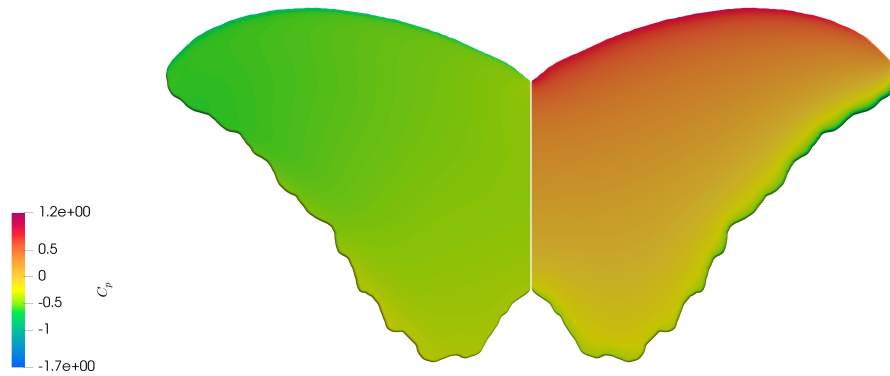
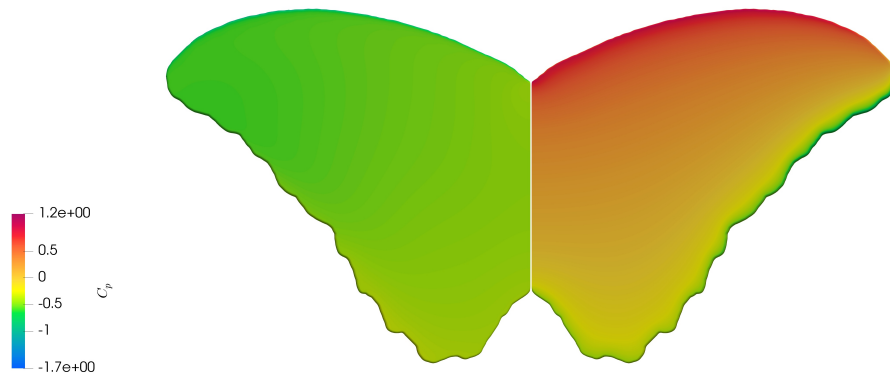


Figure B.40.: *Morpho deidamia*: pressure coefficient on the wing at 20° angle of attack. On the left the dorsal side, on the right the ventral side of the wing.



B.4. *Morpho cisseis*: velocity limiting streamlines on the wing

Figure B.41.: *Morpho cisseis*: velocity limiting streamlines on the wing at 2° angle of attack. On the left the dorsal side, on the right the ventral side of the wing.



Figure B.42.: *Morpho cisseis*: velocity limiting streamlines on the wing at 4° angle of attack. On the left the dorsal side, on the right the ventral side of the wing.



Figure B.43.: *Morpho cisseis*: velocity limiting streamlines on the wing at 6° angle of attack. On the left the dorsal side, on the right the ventral side of the wing.

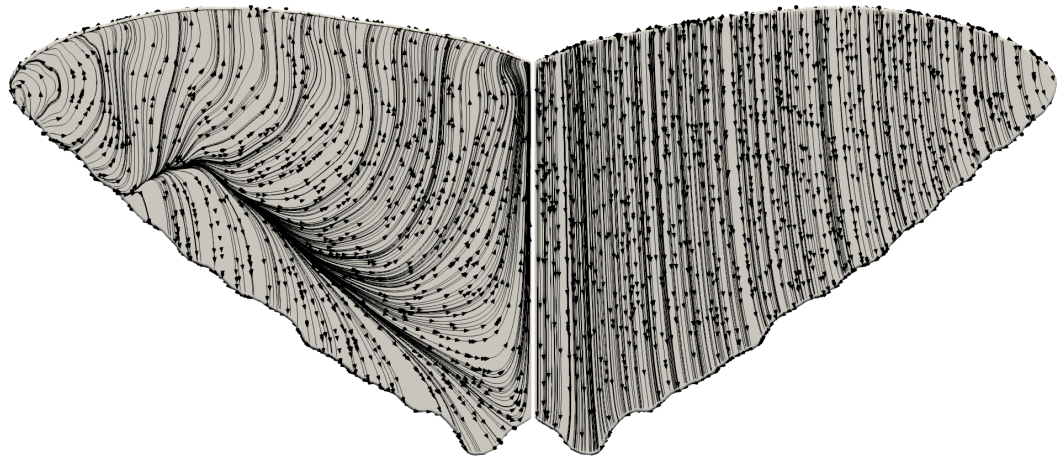


Figure B.44.: *Morpho cisseis*: velocity limiting streamlines on the wing at 8° angle of attack. On the left the dorsal side, on the right the ventral side of the wing.

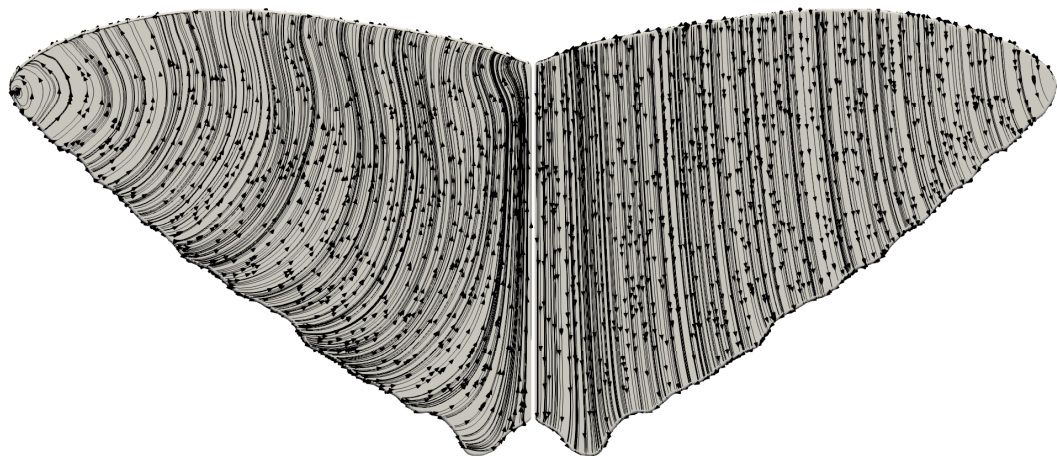


Figure B.45.: *Morpho cisseis*: velocity limiting streamlines on the wing at 10° angle of attack. On the left the dorsal side, on the right the ventral side of the wing.

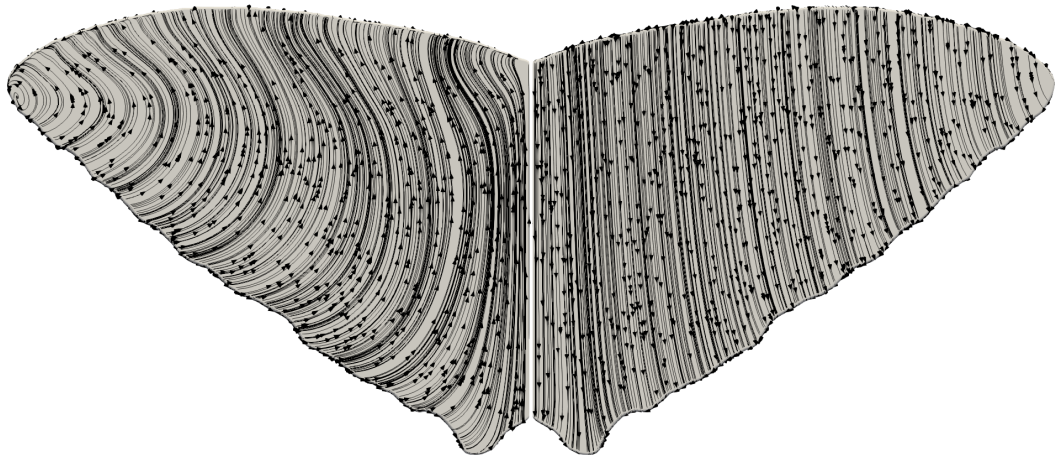


Figure B.46.: *Morpho cisseis*: velocity limiting streamlines on the wing at 12° angle of attack. On the left the dorsal side, on the right the ventral side of the wing.

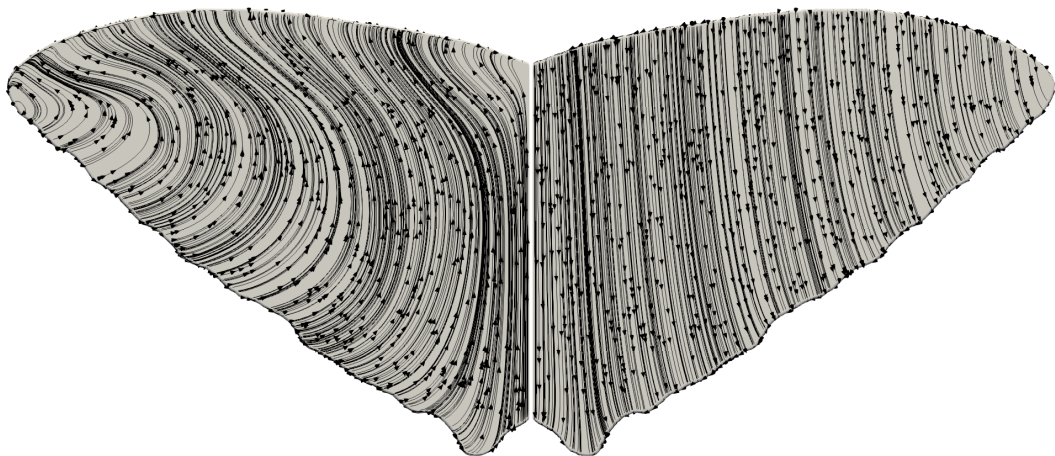


Figure B.47.: *Morpho cisseis*: velocity limiting streamlines on the wing at 14° angle of attack. On the left the dorsal side, on the right the ventral side of the wing.

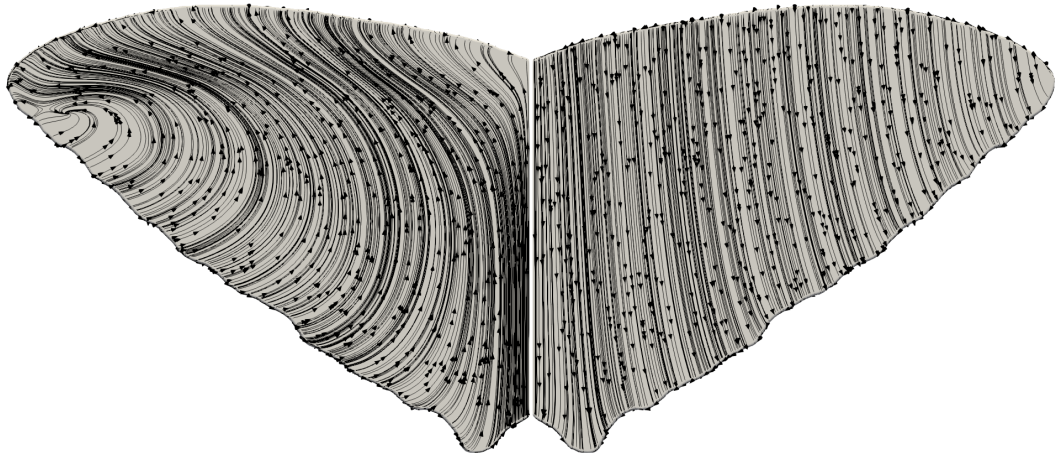


Figure B.48.: *Morpho cisseis*: velocity limiting streamlines on the wing at 16° angle of attack. On the left the dorsal side, on the right the ventral side of the wing.

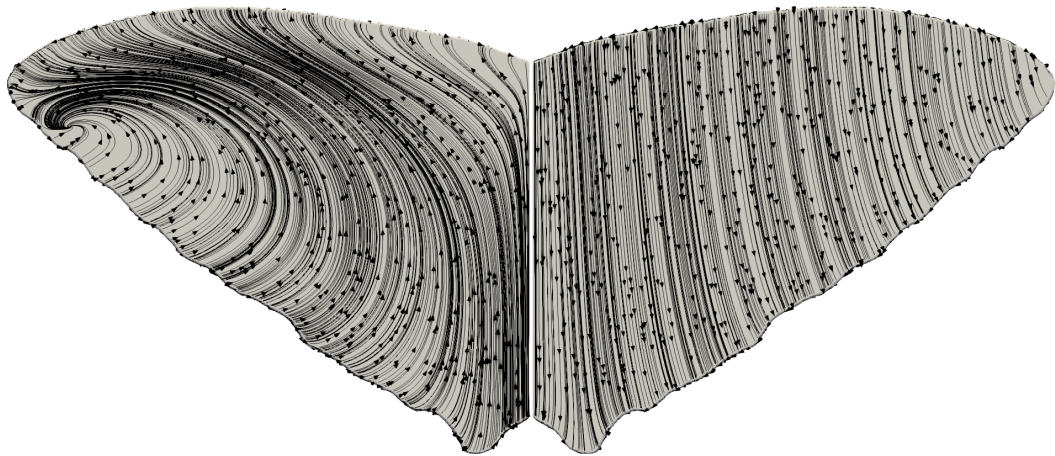


Figure B.49.: *Morpho cisseis*: velocity limiting streamlines on the wing at 18° angle of attack. On the left the dorsal side, on the right the ventral side of the wing.

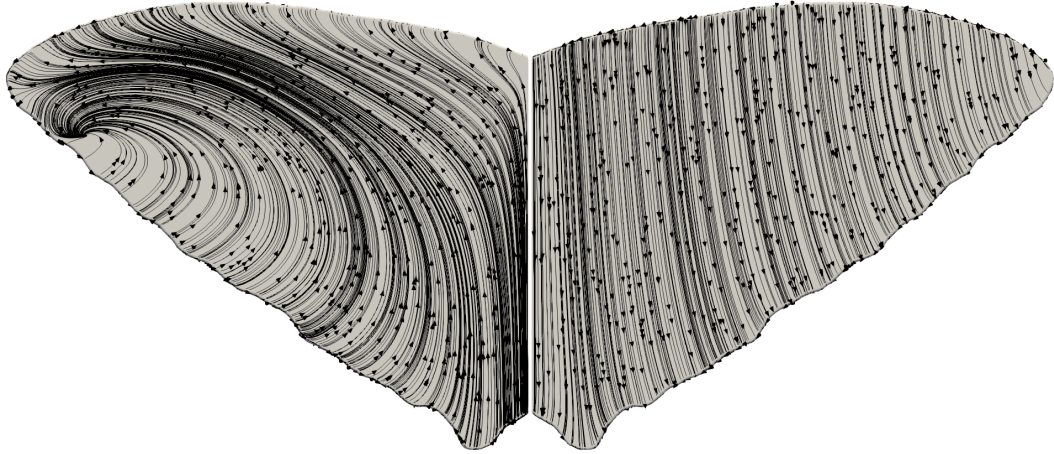
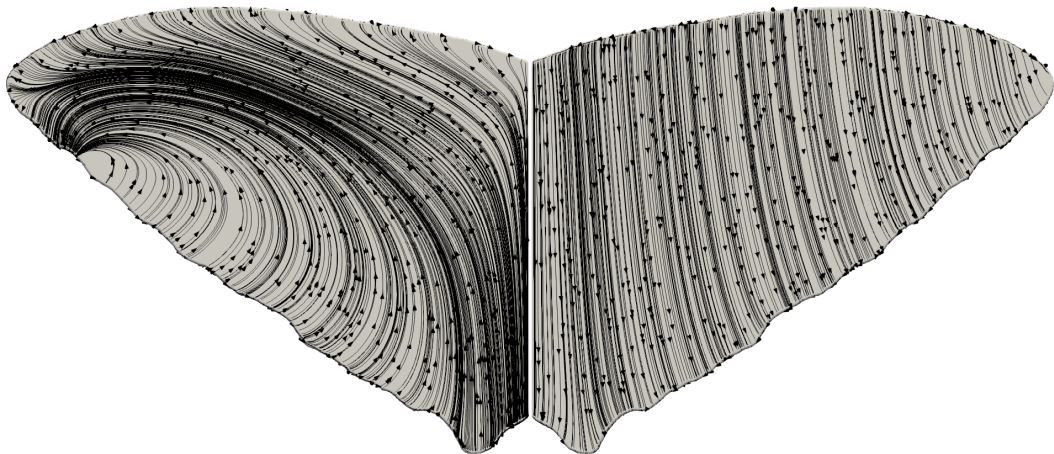


Figure B.50.: *Morpho cisseis*: velocity limiting streamlines on the wing at 20° angle of attack. On the left the dorsal side, on the right the ventral side of the wing.



B.5. *Morpho deidamia*: velocity limiting streamlines on the wing

Figure B.51.: *Morpho deidamia*: velocity limiting streamlines on the wing at 2° angle of attack. On the left the dorsal side, on the right the ventral side of the wing.



Figure B.52.: *Morpho deidamia*: velocity limiting streamlines on the wing at 4° angle of attack. On the left the dorsal side, on the right the ventral side of the wing.

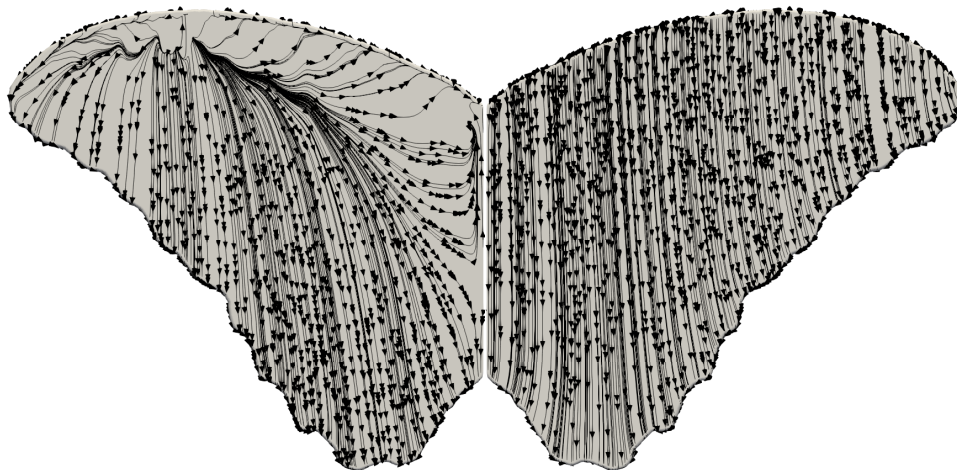


Figure B.53.: *Morpho deidamia*: velocity limiting streamlines on the wing at 6° angle of attack. On the left the dorsal side, on the right the ventral side of the wing.

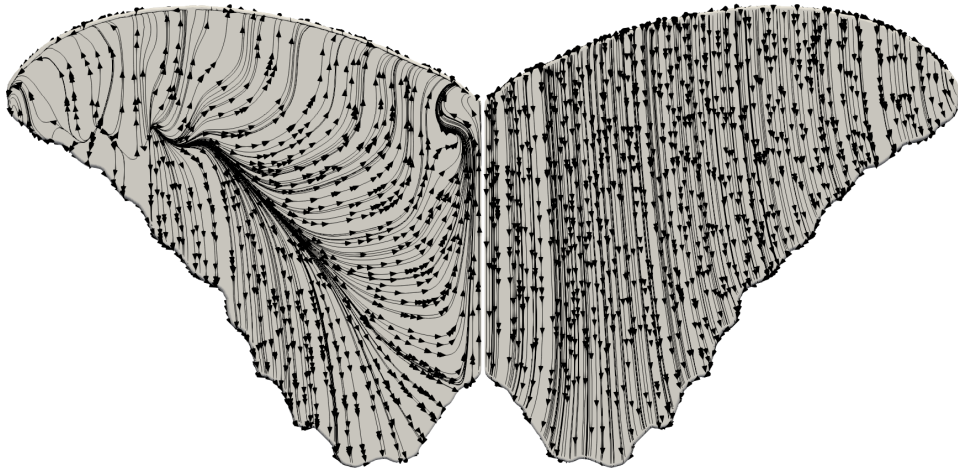


Figure B.54.: *Morpho deidamia*: velocity limiting streamlines on the wing at 8° angle of attack. On the left the dorsal side, on the right the ventral side of the wing.



Figure B.55.: *Morpho deidamia*: velocity limiting streamlines on the wing at 10° angle of attack. On the left the dorsal side, on the right the ventral side of the wing.



Figure B.56.: *Morpho deidamia*: velocity limiting streamlines on the wing at 12° angle of attack. On the left the dorsal side, on the right the ventral side of the wing.

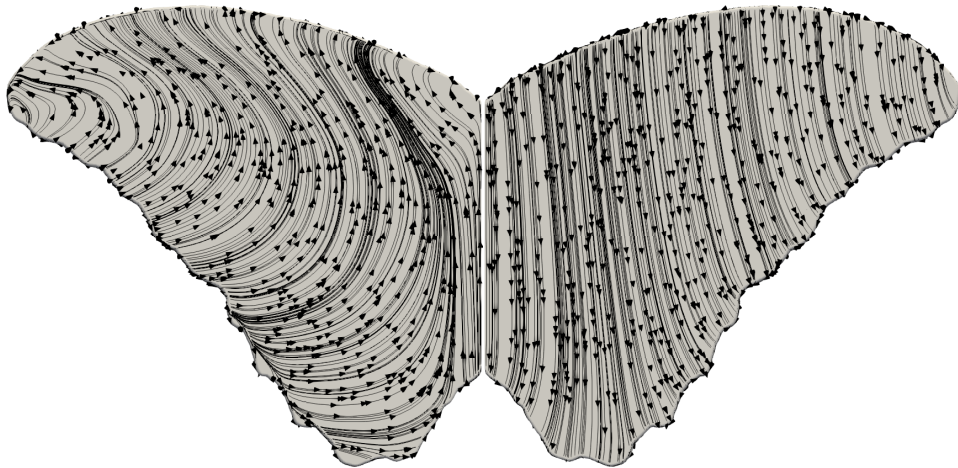


Figure B.57.: *Morpho deidamia*: velocity limiting streamlines on the wing at 14° angle of attack. On the left the dorsal side, on the right the ventral side of the wing.

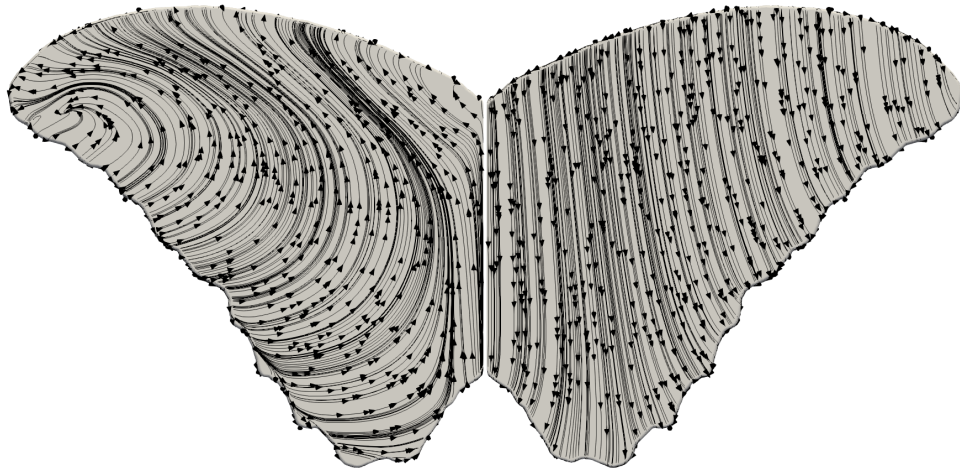


Figure B.58.: *Morpho deidamia*: velocity limiting streamlines on the wing at 16° angle of attack. On the left the dorsal side, on the right the ventral side of the wing.

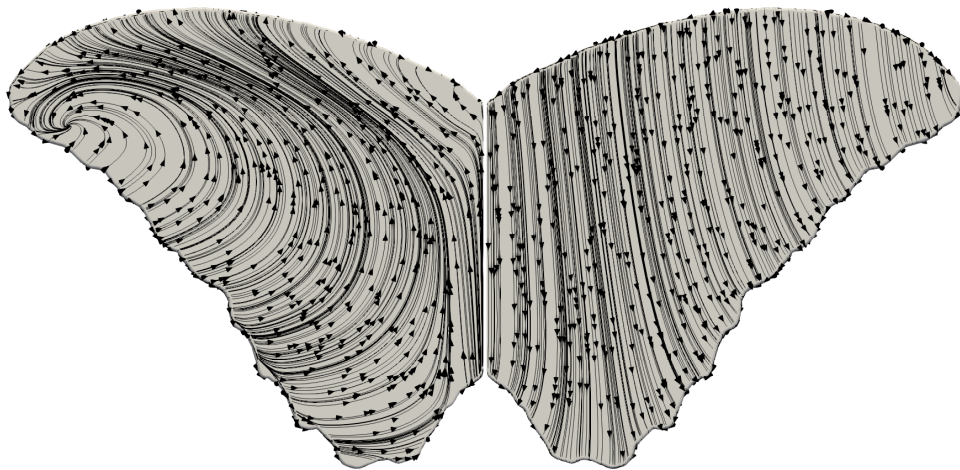


Figure B.59.: *Morpho deidamia*: velocity limiting streamlines on the wing at 18° angle of attack. On the left the dorsal side, on the right the ventral side of the wing.

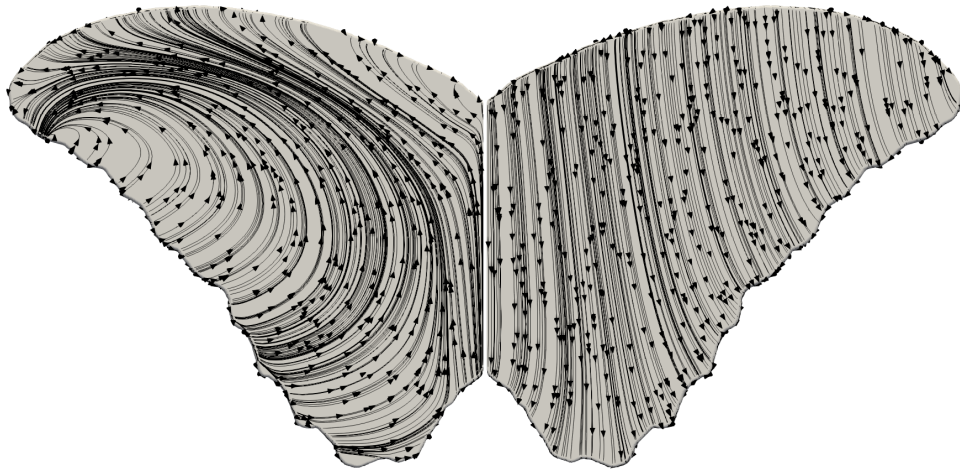
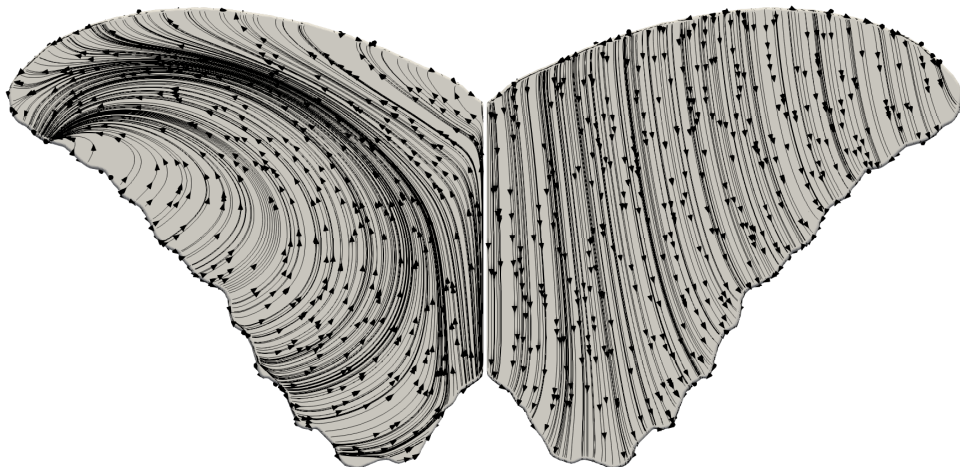


Figure B.60.: *Morpho deidamia*: velocity limiting streamlines on the wing at 20° angle of attack. On the left the dorsal side, on the right the ventral side of the wing.



B.6. Morpho cisseis: vortex structures

Figure B.61.: *Morpho cisseis*: contour surface of λ_2 criterion for the value 0.1 coloured with u_t/u at 2° angle of attack. On the left the dorsal side, on the right the ventral side of the wing.

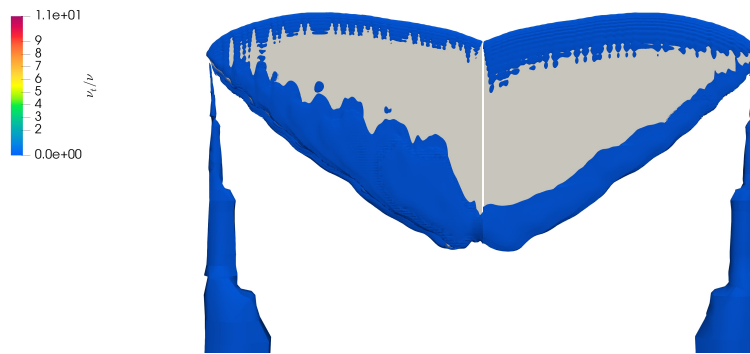


Figure B.62.: *Morpho cisseis*: contour surface of λ_2 criterion for the value 0.1 coloured with u_t/u at 4° angle of attack. On the left the dorsal side, on the right the ventral side of the wing.

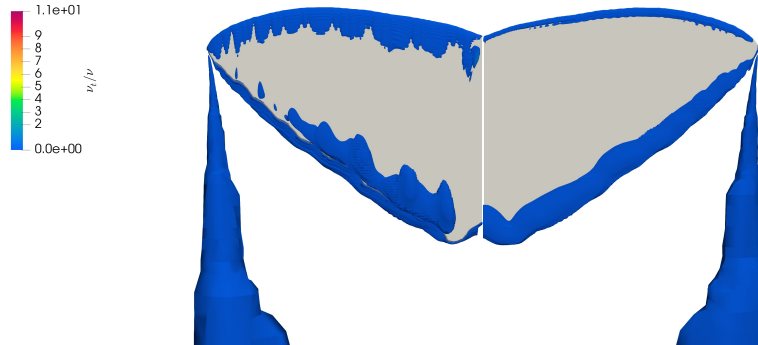


Figure B.63.: *Morpho cisseis*: contour surface of λ_2 criterion for the value 0.1 coloured with u_t/u at 6° angle of attack. On the left the dorsal side, on the right the ventral side of the wing.

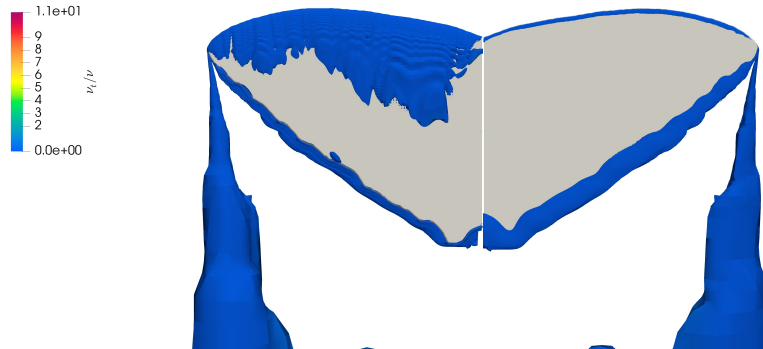


Figure B.64.: *Morpho cisseis*: contour surface of λ_2 criterion for the value 0.1 coloured with u_t/u at 8° angle of attack. On the left the dorsal side, on the right the ventral side of the wing.

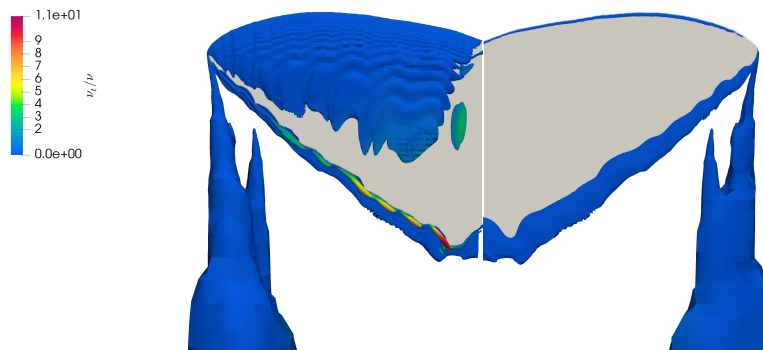


Figure B.65.: *Morpho cisseis*: contour surface of λ_2 criterion for the value 0.1 coloured with u_t/u at 10° angle of attack. On the left the dorsal side, on the right the ventral side of the wing.

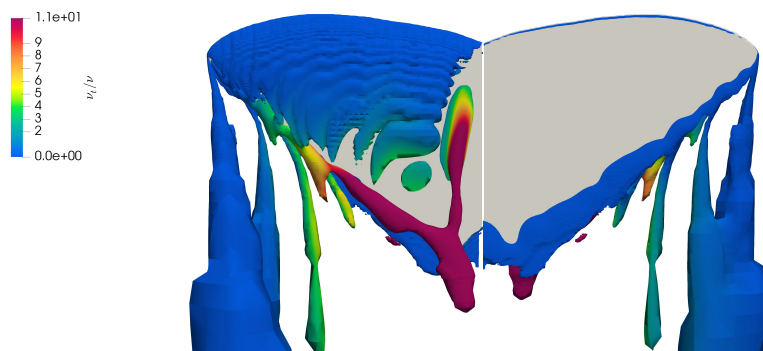


Figure B.66.: *Morpho cisseis*: contour surface of λ_2 criterion for the value 0.1 coloured with u_t/u at 12° angle of attack. On the left the dorsal side, on the right the ventral side of the wing.

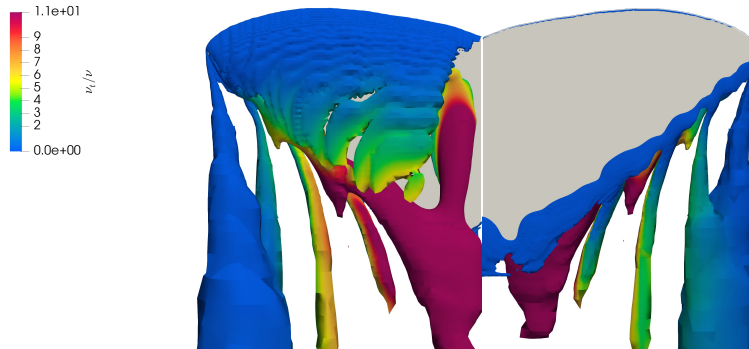


Figure B.67.: *Morpho cisseis*: contour surface of λ_2 criterion for the value 0.1 coloured with u_t/u at 14° angle of attack. On the left the dorsal side, on the right the ventral side of the wing.

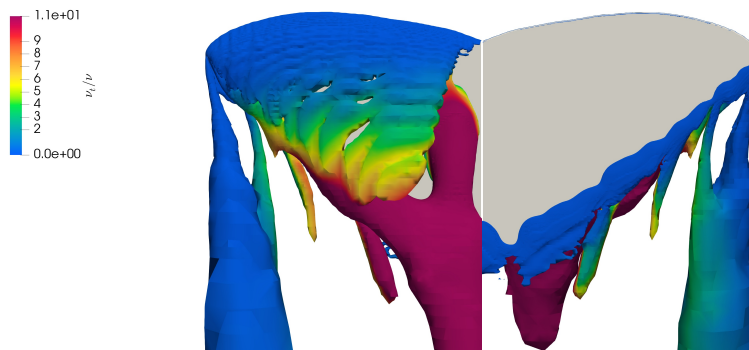


Figure B.68.: *Morpho cisseis*: contour surface of λ_2 criterion for the value 0.1 coloured with u_t/u at 16° angle of attack. On the left the dorsal side, on the right the ventral side of the wing.

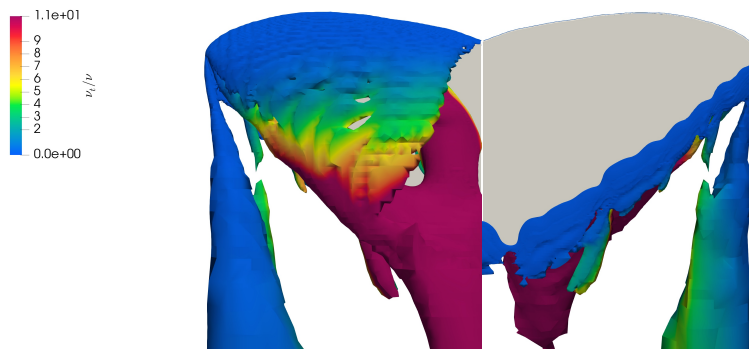


Figure B.69.: *Morpho cisseis*: contour surface of λ_2 criterion for the value 0.1 coloured with u_t/u at 18° angle of attack. On the left the dorsal side, on the right the ventral side of the wing.

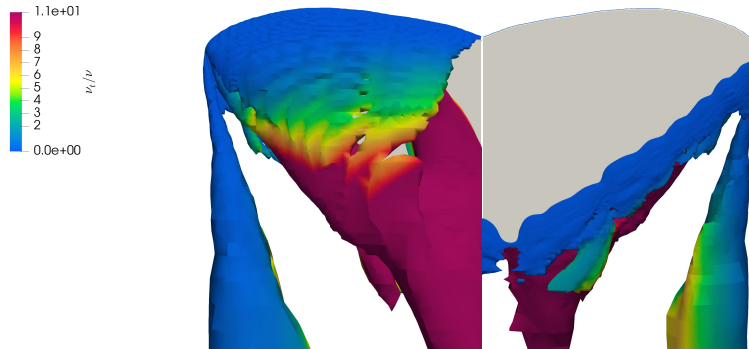
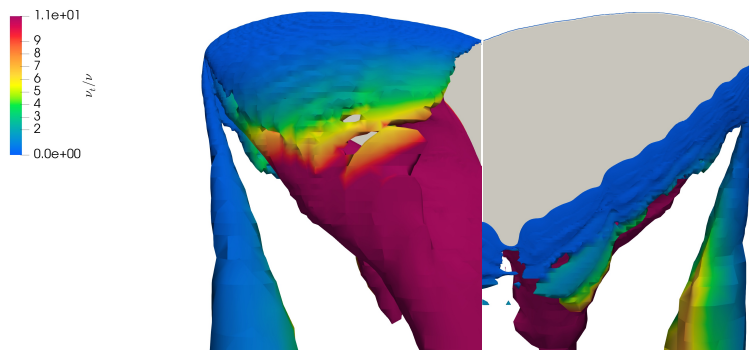


Figure B.70.: *Morpho cisseis*: contour surface of λ_2 criterion for the value 0.1 coloured with u_t/u at 20° angle of attack. On the left the dorsal side, on the right the ventral side of the wing.



B.7. Morpho deidamia: vortex structures

Figure B.71.: *Morpho deidamia*: contour surface of λ_2 criterion for the value 0.1 coloured with u_t/u at 2° angle of attack. On the left the dorsal side, on the right the ventral side of the wing.

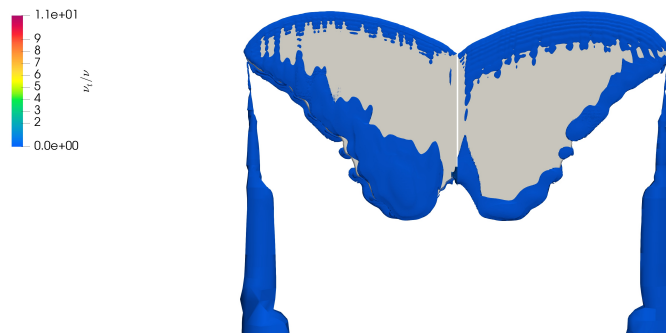


Figure B.72.: *Morpho deidamia*: contour surface of λ_2 criterion for the value 0.1 coloured with u_t/u at 4° angle of attack. On the left the dorsal side, on the right the ventral side of the wing.

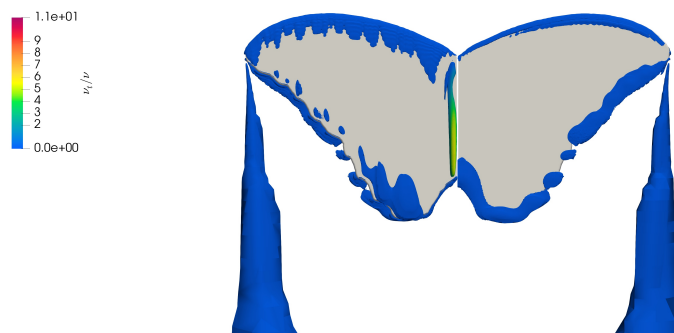


Figure B.73.: *Morpho deidamia*: contour surface of λ_2 criterion for the value 0.1 coloured with u_t/u at 6° angle of attack. On the left the dorsal side, on the right the ventral side of the wing.

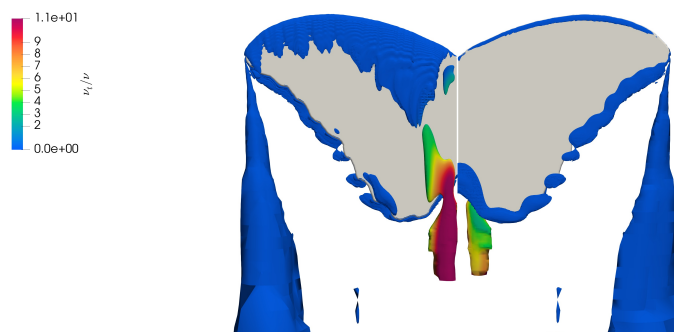


Figure B.74.: *Morpho deidamia*: contour surface of λ_2 criterion for the value 0.1 coloured with u_t/u at 8° angle of attack. On the left the dorsal side, on the right the ventral side of the wing.

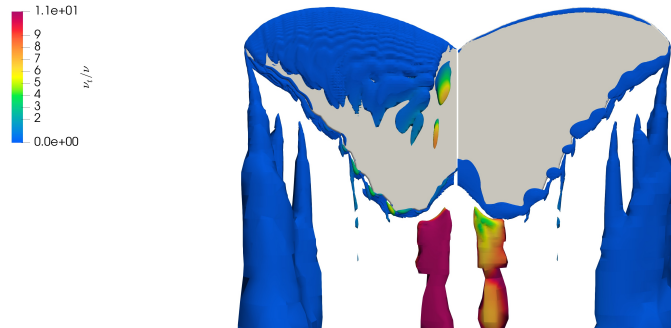


Figure B.75.: *Morpho deidamia*: contour surface of λ_2 criterion for the value 0.1 coloured with u_t/u at 10° angle of attack. On the left the dorsal side, on the right the ventral side of the wing.

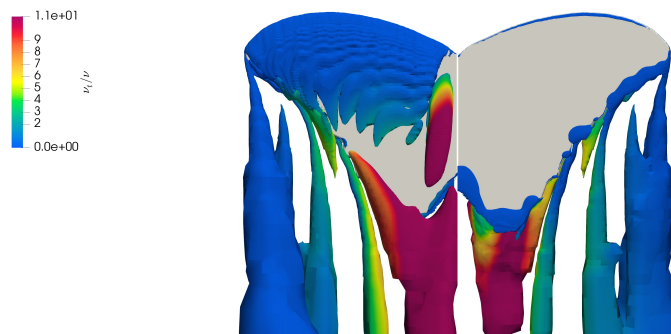


Figure B.76.: *Morpho deidamia*: contour surface of λ_2 criterion for the value 0.1 coloured with u_t/u at 12° angle of attack. On the left the dorsal side, on the right the ventral side of the wing.

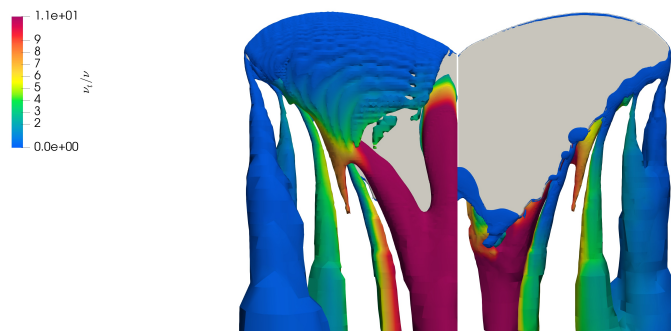


Figure B.77.: *Morpho deidamia*: contour surface of λ_2 criterion for the value 0.1 coloured with u_t/u at 14° angle of attack. On the left the dorsal side, on the right the ventral side of the wing.

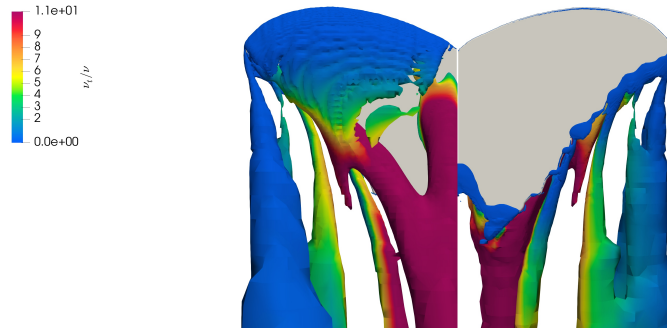


Figure B.78.: *Morpho deidamia*: contour surface of λ_2 criterion for the value 0.1 coloured with u_t/u at 16° angle of attack. On the left the dorsal side, on the right the ventral side of the wing.

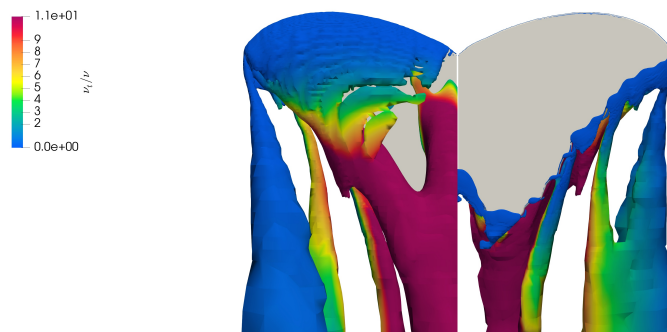


Figure B.79.: *Morpho deidamia*: contour surface of λ_2 criterion for the value 0.1 coloured with u_t/u at 18° angle of attack. On the left the dorsal side, on the right the ventral side of the wing.

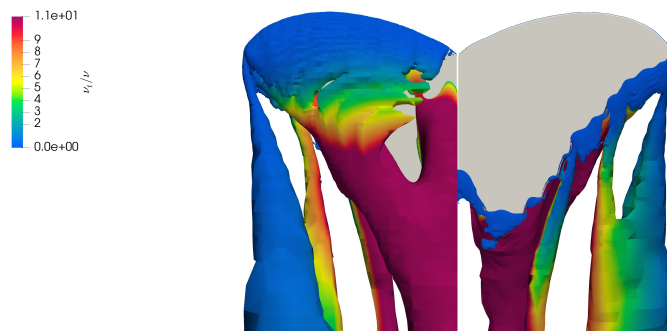
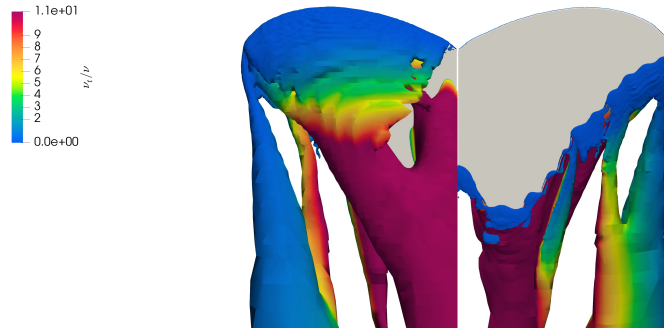


Figure B.80.: *Morpho deidamia*: contour surface of λ_2 criterion for the value 0.1 coloured with u_t/u at 20° angle of attack. On the left the dorsal side, on the right the ventral side of the wing.



Bibliography

- [1] E. ARISTODEMOU, L. M. BOGANEGRA, L. MOTTET, D. PAVLIDIS, A. CONSTANTINOU, C. PAIN, A. ROBINS, AND H. APSIMON, *How tall buildings affect turbulent air flows and dispersion of pollution within a neighbourhood*, *Environmental Pollution*, 233 (2018), pp. 782–796.
- [2] G. K. BATCHELOR, *An Introduction to Fluid Dynamics*, Cambridge University Press, Cambridge, 2000.
- [3] A. L. BRASLOW, R. M. HICKS, AND R. V. HARRIS, *Use of grit-type boundary-layer-transition trips on wind-tunnel models*, Tech. Rep. 1966, 1966.
- [4] G. BURESTI, *Bluff body aerodynamics*, 2000.
- [5] P. CREPIER, *Ship resistance prediction: Verification and validation exercise on unstructured grids*, 7th International Conference on Computational Methods in Marine Engineering, MARINE 2017, 2017-May (2017), pp. 365–376.
- [6] L. DAVIDSON, *Fluid mechanics, turbulent flow and turbulence modeling*, CFD course, (2012), pp. 1–270.
- [7] P. A. DAVIDSON, *An introduction to turbulence models*, Citeseer, 2015.
- [8] A. DE BOER, M. S. VAN DER SCHOOT, AND H. BIJL, *Mesh deformation based on radial basis function interpolation*, *Computers and Structures*, 85 (2007), pp. 784–795.
- [9] M. H. DICKINSON, F. O. LEHMANN, AND S. P. SANE, *Wing Rotation and the Aerodynamics Basis of Insect Flight*, *Science*, 284 (1999), pp. 1954–1960.
- [10] K. J. DROST, H. JOHNSON, S. V. APTEY, AND J. A. LIBURDYZ, *Low reynolds number flow dynamics of a thin airfoil with an actuated leading edge*, 41st AIAA Fluid Dynamics Conference and Exhibit, (2011), pp. 1–20.

- [11] L. EÇA, *Verification and Validation in CFD*, in MARIN Accademy, 2019.
- [12] L. EÇA AND M. HOEKSTRA, *A procedure for the estimation of the numerical uncertainty of CFD calculations based on grid refinement studies*, Journal of Computational Physics, 262 (2014), pp. 104–130.
- [13] C. P. ELLINGTON, *The Aerodynamics of Hovering Insect Flight. III. Kinematics*, Philosophical Transactions of the Royal Society B: Biological Sciences, 305 (1984), pp. 41–78.
- [14] ———, *The Aerodynamics of Hovering Insect Flight. IV. Aerodynamic Mechanisms*, Philosophical Transactions of the Royal Society B: Biological Sciences, 305 (1984), pp. 79–113.
- [15] S. GIRIMAJI, *Partially-Averaged Navier-Stokes Model for Turbulence: A Reynolds-Averaged Navier-Stokes to Direct Numerical Simulation Bridging Method*, Journal of Applied Mechanics, 73 (2006), p. 413.
- [16] S. GIRIMAJI AND K. ABDOL-HAMID, *Partially-Averaged Navier Stokes Model for Turbulence: Implementation and Validation*, (2013), pp. 1–14.
- [17] J. JEONG AND F. HUSSAIN, *On the identification of a vortex*, Journal of Fluid Mechanics, 285 (1995), pp. 69–94.
- [18] A. V. JOHANSSON AND W. STEFAN, *An introduction to turbulence*, 2015.
- [19] M. KLAPWIJK, T. LLOYD, AND G. VAZ, *International Journal of Heat and Fluid Flow On the accuracy of partially averaged Navier â Stokes resolution estimates*, International Journal of Heat and Fluid Flow, 80 (2019), p. 108484.
- [20] R. B. LANGTRY AND F. R. MENTER, *Transition Modeling for General CFD Application in Aeronautics*, 43rd AIAA Aerospace Sciences Meeting and Exhibition, (2005), pp. 1–14.
- [21] R. B. LANGTRY, F. R. MENTER, S. R. LIKKI, Y. B. SUZEN, P. G. HUANG, AND S. VOÏLKER, *A Correlation-Based Transition Model Using Local VariablesâPart II: Test Cases and Industrial Applications*, Journal of Turbomachinery, 128 (2006), p. 423.
- [22] C. LE ROY, *Unpublished filed data of Morpho butterflies*, 2019.

- [23] C. LE ROY, V. DEBAT, AND V. LLAURENS, *Adaptive evolution of butterfly wing shape: from morphology to behaviour*, *Biological Reviews*, 94 (2019), pp. 1261–1281.
- [24] F. O. LEHMANN, *The mechanisms of lift enhancement in insect flight*, *Naturwissenschaften*, 91 (2004), pp. 101–122.
- [25] D. LENTINK AND M. H. DICKINSON, *Rotational accelerations stabilize leading edge vortices on revolving fly wings.*, *The Journal of experimental biology*, 212 (2009), p. 2705.
- [26] MARITIME RESEARCH INSTITUTE NETHERLANDS, *ReFRESHCO Theory Manual*, (2017).
- [27] ———, *Numerical Uncertainty Analysis - User Manual*, tech. rep., 2018.
- [28] ———, *ReFRESHCO Official website*, 2019.
- [29] P. MAZZOLDI, M. NIGRO, AND C. VOCI, *Elementi di fisica: 1*, EdiSES, Napoli, 2007.
- [30] F. R. MENTER, *Zonal Two Equation $k-\epsilon$, Turbulence Models for Aerodynamic Flows.*, 24th Fluid Dynamics Conference July 6-9, 1993 / Orlando, Florida, (1993).
- [31] F. R. MENTER, M. KUNTZ, AND R. B. LANGTRY, *Ten years of Industrial Experience with the SST Turbulence Model*, *Heat and Mass Transfer*, (2003).
- [32] F. R. MENTER, R. B. LANGTRY, S. R. LIKKI, Y. B. SUZEN, P. G. HUANG, AND S. VOÛLKER, *A Correlation-Based Transition Model Using Local Variables: Part I - Model Formulation*, Volume 4: Turbo Expo 2004, (2004), pp. 57–67.
- [33] M. MIZOGUCHI AND H. ITOH, *Effect of aspect ratio on aerodynamic characteristics at low Reynolds numbers*, *AIAA Journal*, 51 (2013), pp. 1631–1639.
- [34] F. T. MUIJRES, P. HENNINGSSON, M. STUIVER, AND A. HEDENSTRÖM, *Aerodynamic flight performance in flap-gliding birds and bats*, *Journal of Theoretical Biology*, 306 (2012), pp. 120–128.

- [35] F. T. MUIJRES, N. A. IWASAKI, M. J. ELZINGA, J. M. MELIS, AND M. H. DICKINSON, *Flies compensate for unilateral wing damage through modular adjustments of wing and body kinematics*, *Interface Focus*, 7 (2017).
- [36] F. T. MUIJRES, L. C. JOHANSSON, M. S. BOWLIN, Y. WINTER, AND A. HEDENSTRÖM, *Comparing aerodynamic efficiency in birds and bats suggests better flight performance in birds*, *PLoS ONE*, 7 (2012).
- [37] K. NIITEPÖLD, A. L. MATTILA, P. J. HARRISON, AND I. HANSKI, *Flight metabolic rate has contrasting effects on dispersal in the two sexes of the Glanville fritillary butterfly*, *Oecologia*, 165 (2011), pp. 847–854.
- [38] NUMECA INTERNATIONAL, *HEXPRESS Official website*, 2019.
- [39] H. PARK, K. BAE, B. LEE, W. P. JEON, AND H. CHOI, *Aerodynamic performance of a gliding swallowtail butterfly wing model*, *Proceedings of the Society for Experimental Mechanics, Inc.*, 67 (2010), pp. 1313–1321.
- [40] Y. POMEAU AND P. MANNEVILLE, *Intermittent Transition to Turbulence in Dissipative Dynamical Systems*, *Transition*, 197 (1980), pp. 189–197.
- [41] S. B. POPE, *Turbulent Flows.pdf*, 2001.
- [42] ROBERT MCNEEL & ASSOCIATES, *Rhino Official website*, 2019.
- [43] G. F. ROSETTI, G. VAZ, AND A. L. FUJARRA, *Urans calculations for smooth circular cylinder flow in a wide range of reynolds numbers: Solution Verification and Validation*, *Proceedings of the International Conference on Offshore Mechanics and Arctic Engineering - OMAE*, 5 (2012), pp. 549–571.
- [44] S. P. SANE, *The aerodynamics of insect flight*, *Journal of Experimental Biology*, 206 (2003), pp. 4191–4208.
- [45] H. SCHLICHTING AND K. GERSTEN, *Boundary-layer theory*, Springer, 2016.
- [46] M. SMITH, A. ORTEGA ANCEL, M. KOVAČ, C. ITHIER, R. WOOD, D. VOGT, AND R. EASTWOOD, *Aerodynamic evaluation of wing shape and wing orientation in four butterfly species using numerical simulations and a low-speed wind tunnel, and its implications for the design of flying micro-robots*, *Interface Focus*, 7 (2016), p. 20160087.

- [47] P. R. SPALART AND S. R. ALLMARAS, *A One-Equation Turbulence for Aerodynamic Flows*, 30th Aerospace Sciences Meeting and Exhibit, (1992).
- [48] H. THENNEKES AND J. L. LUMLEY, *A First Course in Turbulence*, vol. 49, 1972.
- [49] G. E. TORRES AND T. J. MUELLER, *Low-aspect-ratio wing aerodynamics at low reynolds numbers*, AIAA Journal, 42 (2004), pp. 865–873.
- [50] D. J. TRITTON, *Physical Fluid Dynamics*, 2nd ed., 1988.
- [51] W. VAN VEEN, J. L. VAN LEEUWEN, AND F. T. MUIJRES, *Rotation axis offset enhances rotational lift production in insect wings: a numerical study*, Journal of The Royal Society Interface, 16 (2019).
- [52] D. C. WILCOX, *Reassessment of the scale-determining equation for advanced turbulence models*, AIAA Journal, 26 (1988), pp. 1299–1310.
- [53] ———, *Turbulence Modeling for CFD*, 2006.
- [54] J. WINDT, *Improvement of the grid deformation methods in ReFRESHCO - Report No. 70058-7-RD*, tech. rep., 2015.
- [55] J. WINDT AND C. KLAIJ, *Incompressible flow simulations on moving and deforming grids - Report No. 70058-2-RD*, tech. rep., 2013.